Control of self-assembly of organic semiconductors by solution processing for electronic applications

Dissertation zur Erlangung des Grades

“Doktor der Naturwissenschaften”

am Chemie, Pharmazie, Geographie und Geowissenschaften

der Johannes Gutenberg-Universität Mainz

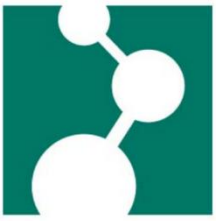

Ke Zhang

Geboren in Shandong, P.R. China

Mainz im April 2019

Dekan:

1. Gutachter:

2. Gutachter:

Tag der mündlichen Prüfung

Affidavit

I hereby confirm that I have completed the present dissertation independently and without inadmissible external support. I have not used any sources or tools other than those indicated and have identified literal and analogous quotations.

Furthermore, I confirm that this thesis has not yet been submitted as part of another examination process neither in identical nor in similar form.

Ort, Datum: Unterschrift:

Contents

Chapter 1 Introduction

In this chapter, controlled self-assembly of organic semiconductors (OSCs) and charge carrier transport of organic field-effect transistors (OFETs) are introduced. Firstly, I introduce the basic working principle, classification, and characterization of OFETs. Secondly, the relationship between the microstructure of OSC films and transistor performance is presented. In addition, the physical processes and crystallization mechanism during solution processing of OSCs are introduced. Finally, solution processing techniques for controlling the self-assembly of OSCs for electronic applications is discussed in detail.

1.1 General background of OFETs

1.1.1 Organic electronics

Nowadays, electronics take an important role in our daily life, including information technology, multimedia and healthcare. Many of the pioneering studies and commercialized technologies rely on inorganic semiconductors. Notably, inorganic semiconductors (such as silicon) exhibit excellent conductive properties and precise machining. At the same time, organic electronics including OFETs, organic photovoltaics (OPVs) and organic light emitting diodes (OLEDs),[1] have also attracted great attention and have shown a rapid increase in performance during the last decades.[1-4] OSCs are a class of carbon-based materials that exhibit semiconducting properties and consist of conjugated small molecules and polymers. Compared to inorganic semiconductors, OSCs can permit solution processable electronic devices that are flexible and light-weight. [5, 6] Next to its application in printed electronic circuits, OFET is also a key element for driving OLEDs as well as realizing label-free sensing applications in the field of environmental monitoring.[7, 8] Therefore, intensive efforts both from academic and industry have been made in developing high performance OFETs. Figure

1 shows examples of organic electronics for wearable devices on flexible substrates,[9] and a large-area array of stretchable transistors on fingertip and wrist.[10] These kinds of flexible organic electronic circuits are highly desirable for applications such as medical treatments.[10]

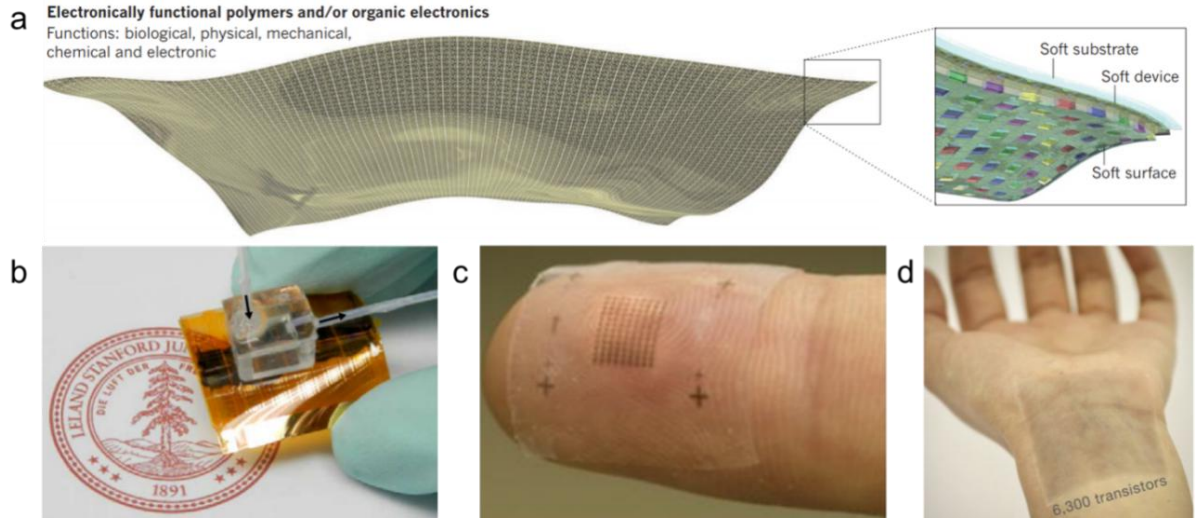

Figure 1.1. (a) Diagram of electronically functional polymer and organic electronics on flexible substrate.[7] (b) Optical image of OFETs on flexible substrate.[9] A large area of stretchable transistors on (c) fingertip and (d) wrist.[10]

In a conjugated molecule, the σ-bond is formed by the overlap of hybridized sp^2 orbitals and the π-bond is formed by the overlap of the unhybridized p_z orbitals. The unfilled anti-bonding orbital of the π-bond corresponds to the lowest unoccupied molecular orbital (LUMO) of the molecule, and the filled bonding orbital corresponds to the highest occupied molecular orbital (HOMO).[11] Electrons are free to move from one atom to another within these π-orbitals, called delocalization. Molecular structure plays a crucial role on the electronic properties of OSCs. For instance, the presence of electron donating/withdrawing groups impacts the overlap of intramolecular π-orbitals. The stacking distance of adjacent molecules influences the overlap of intermolecular π-orbitals.[12] Therefore, designing novel molecular structures for high performance OFETs has been an intensive area of research.

In addition to the molecular structure, also the charge carrier mobility in OFETs is determined by the molecular organization and film morphology.[13] Controlling the self-assembly of OSCs by solution processing has been demonstrated as an efficient way to tune

the microstructure of OSC films for high performance OFETs. In this aspect, the general motivation of this work is to understand the mechanism of OSC self-assembly and crystallization and to design novel solution-processing techniques.

1.1.2 Working principle of OFETs

A typical OFET device consists of three electrodes (source, drain and gate electrodes), a dielectric layer and an active OSC layer (Figure 1.2a). Common gate electrodes include highly doped silicon or deposited metals such as aluminum (Al), silver (Ag) and gold (Au). The selection of source and drain electrodes requires a work function match with the OSC energy level. Common source and drain metal electrodes are Al, Ag and Au. As for the dielectric layer, inorganic insulators such as silicon dioxide (SiO_2), aluminum oxide (Al_2O_3) and polymeric insulators such as poly(methyl methacrylate) (PMMA) and cyclized transparent optical polymer (CYTOP) are widely used.[14] The active OSC layer can be deposited by solution processing or thermal evaporation, whose thickness is in the range from a few to hundred nanometers. In OFETs, the charge carrier transport occurs at the interface between OSC and dielectric layers.

We classify OFETs into four types based on the transistor architecture (Figure 1.2a): bottom-gate and bottom-contact (BGBC), bottom-gate and top-contact (BGTC), top-gate and bottom-contact (TGBC), top-gate and top-contact (TGTC).[15, 16] For instance, heavily doped silicon wafer with 300 nm SiO_2 layer (Si/SiO_2), acting as common gate electrode and dielectric layer, respectively, is widely used in bottom-gate transistors. The SiO_2 dielectric surface can be modified by a self-assembled monolayer to reduce interfacial traps. Furthermore, the bottom-contact geometry also provides the opportunity to modulate the work function of the electrodes to investigate the charge injection into the active layer. Top-contact devices typically exhibit an improved injection compared to bottom ones and additionally

provide the opportunity to observe the interfacial microstructure of OSC film, which is important to understand the relation between film morphology and charge carrier transport.

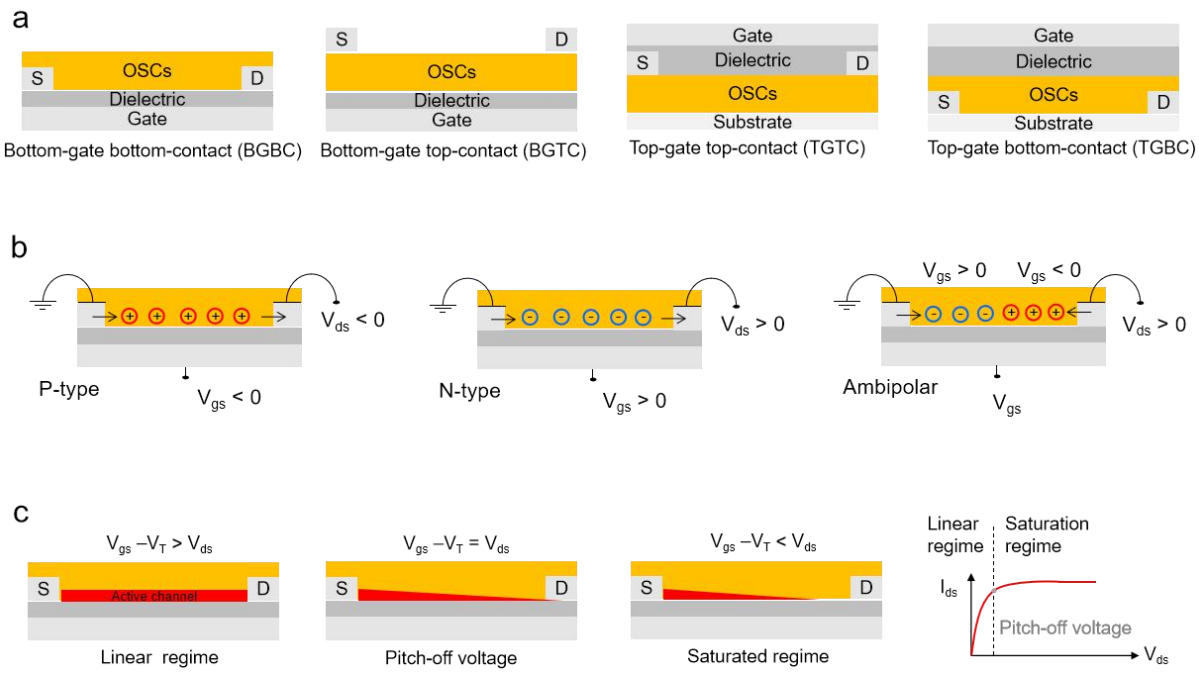

Figure 1.2. Basic working principles of OFETs. Classification of OFETs based on (a) device architecture and (b) charge carrier types. (c) Linear and saturation regime of OFETs. S and D indicate the source and drain electrodes, respectively.

To operate a transistor, a bias voltage between source and gate electrodes (V_g) is applied to accumulate charge carriers at the OSC/dielectric interface, combined with a bias voltage between source and drain electrodes (V_{ds}) to drive the transport of these charge carriers along the OSC/dielectric interface (source electrode is grounded). According to the type of charge carriers, there are three types of OFETs, namely p-type, n-type and ambipolar transistors (Figure 1.2b),[17, 18] which is determined by the HOMO/LUMO of the OSCs and the work functions of source and drain electrodes.[19] For p-type transistors, a negative V_g drives the accumulation of holes at the OSCs/dielectric interface and a negative V_{ds} (higher than the threshold voltage, V_T) drives the hole transport. For n-type OFETs, accumulation and transport of electrons result from positive V_g and V_{ds}, respectively. In ambipolar OFETs, both holes and electrons can be accumulated and transported at the OSC/dielectric interface.[17]

As discussed above, the combination of V_g and V_{ds} drives the transport of charge carriers. In principle, when $V_g = 0$, meaning no accumulation of charge carriers, the source and drain current (I_{ds}) driven by the V_{ds} is low (theoretically should be zero). An electric field between source and gate is required to turn on the transistor. Ideally, only a very low V_g is required to turn the transistor on. However, in reality, the turn-on of the transistor is influenced by the amount by traps present at the OSC/dielectric interface. In that case, first a certain V_{gs} is required to fill all the interface traps with carriers. For larger V_{gs}, the additional accumulated carriers contribute to the I_{ds} ($V_g > V_T$).

The operation of a transistor is characterized by two regimes, the so-called linear and saturation regime, as shown schematically in Figure 1.2c. When $V_{ds} = 0$, the accumulated charge carriers uniformly distribute at the OSC/dielectric interface, and $I_{ds} = 0$ since there is no driving voltage. A small V_{ds} ($V_{ds} << V_g - V_T$) leads to a linear gradient of charge density from source to drain electrode and I_{ds} is proportional to V_{ds}, termed as linear regime. With the increase of $V_{ds,}$ a pinch-off appears near the drain electrode at $V_{ds} = V_g - V_T$, forming a charge carrier depletion region. A further increase of V_{ds} will not lead to further enhance of I_{ds} anymore, termed as saturation regime. Carriers are swept from the pinch point to the drain by a comparatively high electric field in the depletion region. A further increase in V_{ds} pushes the pinch-off point further away from the drain ($V_{ds} >> V_g - V_T$). However, the length of the channel (L) shortens only slightly, as it is infinitely larger than the width of the depletion region, and the integrated resistance of the channel from the source to the pinch point remains more or less the same. For these reasons, once pinch off condition is met, I_{ds} saturates at $V_{ds} = V_g – V_T$. [20]

1.1.3 Characterization of OFETs

Transfer and output curves are two basic electrical characteristics to evaluate the performance of a transistor. Figure 1.3 shows the typical transfer and output curves of a

unipolar p-type OFET. The key parameters of an OFET, including charge carrier mobility (μ), on/off ratio, V_T and subthreshold voltage, can all be extracted from the transfer and output curves. As shown in the output curves (Figure 1.3a), I_{ds} increases with V_{ds} at the linear regime and reaches a stable value at the saturation regime for each V_g. The field effect increases with the applied V_g and leads to higher I_{ds}. Typical transfer curves for p-type OFETs are shown in Figure 1.3b. The saturation mobility, threshold and sub-threshold can be estimated from the slope of $(I_{ds})^{1/2}$-V_g and I_{ds}-V_g curves, respectively.

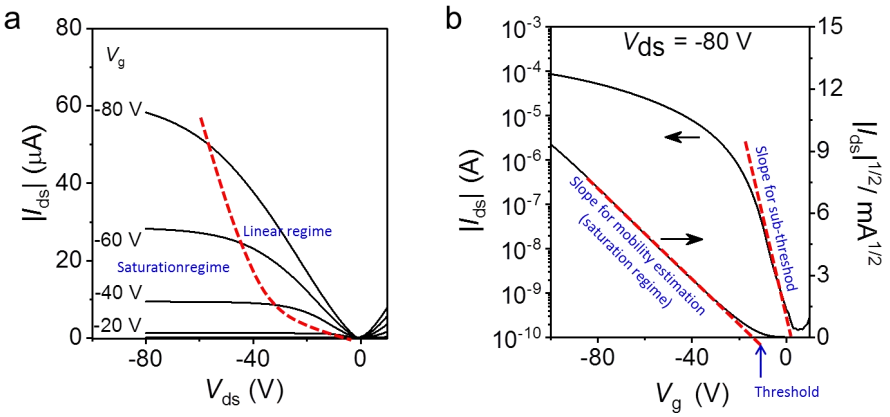

Figure 1.3. Characterization of p-type OFETs by (a) output and (b) transfer curves.

A high-performance OFET requires a high charge carrier mobility (μ) with high on/off ratio and low V_T. The charge carrier mobility quantifies the drift velocity of the charge carriers under an applied electric field. The on/off ratio represents the I_{ds} ratio between on and off states, indicating the ability of the OFET to perform as a switch. V_T describes the minimum V_g to turn on the conducting channel in the OFET. The mobility of the OFET can be calculated based on either the linear regime or saturation regime, respectively.[3]

In the linear regime ($V_{ds} << V_g - V_T$),

$$I_{ds} = \frac{W}{L}\mu_{lin}C_i\left[(V_g - V_T)V_{ds} - \frac{1}{2}V_{ds}^2\right] \qquad \text{(Equation 1.1)}$$

In the saturation regime ($V_{ds} << V_{gs} - V_T$),

$$I_{ds} = \frac{W}{2L}\mu_{sat}C_i\left[(V_g - V_T)^2\right] \qquad \text{(Equation 1.2)}$$

where C_i is the gate dielectric capacitance per unit area, L and W are the channel length and width of the transistor, respectively. The expression for the mobility can be simplified as follows:

In the linear regime ($V_{ds} << V_g - V_T$),

$$\mu_{lin} = \frac{L}{WC_iV_{ds}}\frac{\partial I_{ds}}{\partial V_g} \quad \text{(Equation 1.3)}$$

In the saturation regime ($V_{ds} << V_g - V_T$),

$$\mu_{sat} = \frac{2L}{WC_i}\left(\frac{\partial\sqrt{I_{ds}}}{\partial V_g}\right)^2 \quad \text{(Equation 1.4)}$$

1.1.4 Charge transport mechanism

Dependent on temperature-dependence of the mobility in OFETs, the charge transport mechanism is either classified into band (-like) transport (mobility increases with decreasing temperature) or hopping regime (mobility decreases with decreasing temperature). The presence of inherent disorder and thermally-activated structural fluctuations pose a fundamental challenge to the realization of band(-like) transport.[21] Therefore, in OFETs, band(-like) transport is observed only in very limited number of systems, as single crystals of small molecule OSCs or conjugated polymers with extremely low torsion in the chains.[22-24] In the hopping regime, the charge carrier transport is typically thermal activated, where charge carrier mobility increase with temperature.[25] In most cases, polycrystalline and amorphous OSCs exhibit hopping dominated transport.[3]

1.1.5 Charge injection and traps in OFETs

The device performance of OFETs is determined by the efficiency of charge injection from electrode into the OSC layer, as well as charge transport at the OSC/dielectric interface, which is governed by the mobility but can also be limited by interfacial traps. The role of

charge injection and interfacial traps on OFET performance will now be discussed, whereas the intrinsic charge transport behavior of the active OSC film is presented in the next section.

In a typical OFET, the contact resistance (Rc) cannot be neglected because of the presence of a metal electrode/OSC junction.[26] As shown in Figure 1.4a, the hole injection from the electrode into the OSC layer (with deeper HOMO level) is governed by an injection barrier, φ_b. Taking p-type OSC as an example, φ_b is the difference between the work function of the metal electrode (φ_m) and the HOMO level of the OSC.[26] Doped-injection layers have been used to obtain Ohmic contact.[27, 28] The resulting band bending in the doped layer allows for injection via tunneling.[29] In addition, self-assembled monolayers were also utilized to modify and tune the work function of electrodes.[30, 31] In addition, transition-metal oxides with high work function (such as and Molybdenum trioxide, MoO_3) are also expected to improve hole injection. The utilizing of MoO_3 has been demonstrated to efficiently improve the hole injection in OFETs.[32] However, MoO_3 induces a considerable injection barrier of 0.3-0.4 eV when in contact with amorphous small molecule OSCs in OLEDs. The nanometer interlayer method has been developed to reduce this injection barrier and achieve an Ohmic contact, owing to electrostatic decoupling of the electrode from the OSC (Figure 1.4b).[33]

The presence of interfacial traps significantly influences the charge carrier transport in OFETs.[34] Figure 1.4c shows typical transfer curves of a n-type transistor using *poly(9,9-dioctylfluorene-alt-benzothiadiazole)* (F8BT) as semiconductor on different substrate interfaces, such as a bare Si/SiO_2 substrate (S_{bare}), Si/SiO_2 substrate modified with a hexamethyldisilazane (HMDS) self-assembled monolayer (S_{HMDS}), dodecyltrichlorosilane (DTS) modified substrate (S_{DTS}), trichloro(octadecyl)silane (OTS) modified substrate (S_{OTS}) and polyethylene substrate (S_{PE}). From S_{bare} to S_{HMDS} and S_{OTS} and S_{PE}, I_{on} gradually increases and V_T gradually reduces. It indicates that traps are located at or near the SiO_2 interface and self-assembled monolayers can be used to reduce but cannot completely eliminate the

interfacial traps.[35] In addition to the interfacial traps, bulk traps that originate from molecular disorder and grain boundaries also impede the charge transport.

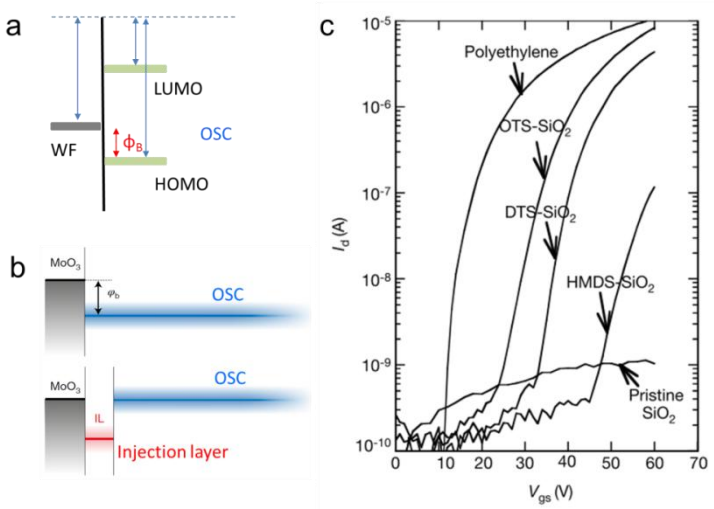

Figure 1.4. (a) Injection barrier of Schottky-Mott limit. φ_b indicates Schottky barrier between the work function of electrode and energy level of OSC. (b) Schematic illustration of injection interlayer for Ohmic contact.[33] (c) Transfer curves of F8BT n-type transistor with different substrate interfaces.[35]

1.2 Molecular organization and film morphology

Understanding the factors that influence the intrinsic charge transport of the active OSC layer is important to achieve a high mobility device. In this section, the relation between molecular structure, molecular organization, film morphology and charge carrier transport performance is introduced.

1.2.1 Molecular design

It is known that the conjugated core, end-group and side chain of the OSC determine the molecular packing and the corresponding electronic performance.[36, 37] Representative and widely used small molecule and polymer based OSCs in OFETs are shown in Figure 1.5. For instance, linear fused acene rings (pentacene) is a promising building block for a high mobility transistor. The mobility of pentacene-based FETs has been reported above 5 $cm^2 s^{-1} V^{-1}$, owing to the perfect single crystal obtained by the physical vapor transport method.

However, pentacene is insoluble in common organic solvents and can therefore not be applied by solution processing. Therefore, triisopropylsilylethynyl substituents are introduced at the pentacene core, 6,13-bis(triisopropylsilylethynyl)pentacene (TIPS-pentacene), improving the solubility and enabling low-cost solution processing.[2] The incorporation of heteroatoms in the pentacene core efficiently modulates the energy levels and induces additional intermolecular interactions. For instance, the electron mobility of silylethynylated N-heteropentacene has been reported to exceed 10 $cm^2 s^{-1} V^{-1}$.[38] Moreover, the incorporation of fused thiophenes provides a promising route to design molecules with enhanced hole mobility,[39, 40] such as 2,7-dioctyl[1]benzothieno[3,2-b][1]benzothiophene (C8-BTBT)[39] and 2,8-difluoro-5,11-bis(triethylsilylethynyl) anthradithiophene (diF-TES-ADT). OFETs based on the strongly aligned C8-BTBT provide a hole mobility up to 25 $cm^2 s^{-1} V^{-1}$[41], whereas devices based on single crystal diF-TES-ADT exhibit a hole mobility above 6 $cm^2 s^{-1} V^{-1}$.[42] In addition, small molecule OSCs based on oligothiophenes,[43] diketopyrrolopyrroles (DPP),[44] naphthalene diimide (NDI),[45] perylene diimide (PDI)[46] are also widely used in OFETs due to their highly delocalized backbone, dense molecular packing and strong intermolecular interactions.

For polymer OSCs the mobility is determined by the charge carrier transport along and between polymer chains. Molecular regioregularity, molecular weight, polydispersity, rotational freedom along the conjugated chain and the construction of donor-acceptor conjugated systems are important factors that influence charge carrier transport.[2, 47] Common conjugated polymers applied in OFETs include polythiophene and various donor-acceptor polymers.[48] Figure 1.5 shows four common polymer OSCs as examples, such as amorphous poly(triarylamine) (PTAA), semi-crystalline poly(3-hexylthiophen-2,5-diyl) (P3HT),[49] donor-acceptor polymer poly[2,5-(2-octyldodecyl)-3,6-diketopyrrolopyrrole-alt-5,5-(2,5-di(thien-2-yl)thieno [3,2-b]thiophene)] (DPP-DTT),[50, 51] and n-type poly{[N,N'-bis(2-octyldodecyl)naphthalene-1,4,5,8-bis(dicarboximide)-2,6-diyl]-alt-5,5'-(2,2'-

bithiophene)} (PNDI(OD)2T)[52]. Among polymer OSCs, donor-acceptor polymers typically exhibit field-effect mobilities on the order of 10^{-2} - 1 cm^2 V^{-1} s^{-1}, but several examples showed a mobility over 10 cm^2 $V^{-1}s^{-1}$.[53]

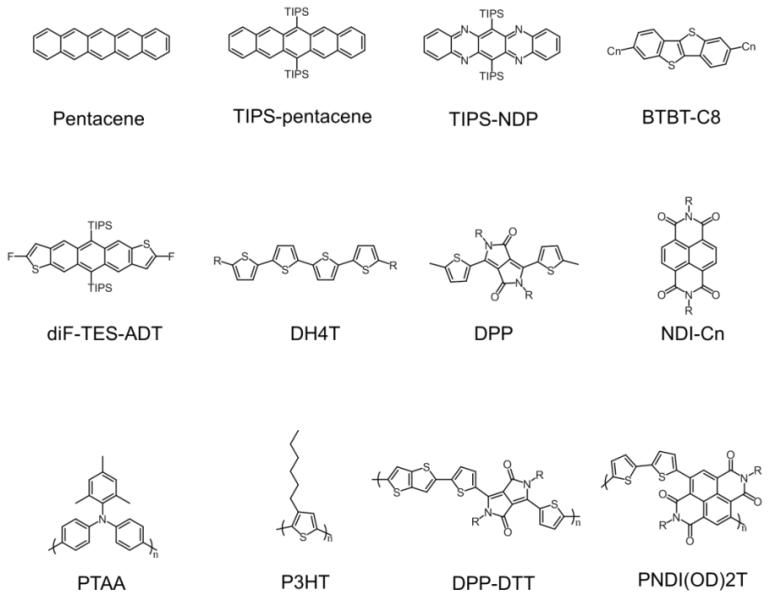

Figure 1.5. Molecular structures of representative small molecule and polymer OSCs in OFETs.

1.2.2 Molecular organization

The charge carrier transport in OFETs significantly depends on the molecular organization. As discussed above, the band (-like) transport is expected to occur in single crystals of small molecule OSCs (Figure 1.6a). Therefore, we firstly discuss molecular packing motifs in small molecule single crystals. According to different π-π stacking geometries among adjacent molecules, typical molecular packing modes can be divided into herringbone, brick layer, slipped and cofacial stacking modes.[54] Especially, the herringbone and brick layer stacking modes are known toexhibit efficient charge transport (Figure 1.6b). In the herringbone mode, the π-π stacking arrangements within columns and the face-to-edge arrangements between columns facilitate charge transfer from one column to the adjacent one, such as in pentacene and rubrene.[2, 55] In the brick layer stacking mode, a large displacement between molecules in adjacent columns induces large π-π overlap that increases

the electronic coupling and improves device performance, as for instance in TIPS-pentacene and diF-TES-ADT.

However, most thin film transistors are based on semi-crystalline and amorphous OSCs. For instance, semi-crystalline polymer OSCs consist of ordered and disordered regions, as shown in Figure 1.6a. The ordered region exhibits strong π-π stacking and long-range periodicity, where the charge carrier transport depends on molecule packing orientation and π-π stacking distance.[56] In contrast to ordered regions, disordered regions are governed by weak intermolecular interactions limiting π-π stacking and/or interlayer packing. The main transport pathways for charge carriers in disordered region are over the polymer chains (Figure 1.6a). Therefore, the charge transport in the ordered region of semi-crystalline OSCs is higher than in the amorphous parts and the connections between the ordered regions play a dominate role on charge carrier transport over macroscopic dimensions.[57] In contrast to semi-crystalline polymer OSCs, amorphous polymer OSCs only show a disordered region and exhibit a limited charge transport performance due to weak intermolecular interactions (Figure 1.6a).

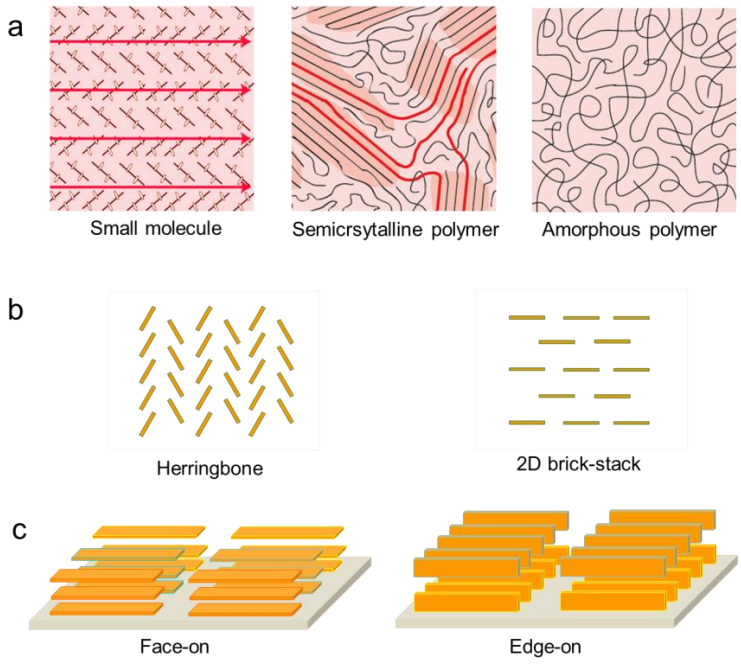

Figure 1.6. (a) Charge transport and molecular microstructure in different OSCs.[57, 58] (b) Illustration of molecular packing modes: herringbone and brick layer stacking. (c) Illustration of face-on and edge-on of polymer OSCs.

The molecular organization of ordered polymer OSCs refers to the molecular packing orientation and packing distance. According to the molecular packing orientation towards the substrate surface, thin film OSCs are classified into edge-on and face-on.[59] In the case of edge-on organization, the backbone plane is arranged perpendicular to the substrate so that the π-stacking direction is oriented parallel to the substrate surface, favorable for charge carrier transport in OFETs.[60] In contrast, in the face-on orientation the backbone plane is parallel to substrate and the π-stacking direction is perpendicular to substrate (Figure 1.6b).[15] A face-on arrangement often leads to lower field-effect mobilities in OFETs, but might be favourable for solar cells.[60]

1.2.3 Film morphology

In addition to molecular organization, film morphology of OSCs also plays a crucial role on the charge carrier transport in OFETs. In many cases, morphological defects, grain boundaries, and misalignment can impede the intrinsic charge transport.[13, 61, 62] For instance, dendritic crystals, coffee-ring and stick-slip morphologies result in a lower mobility. To understand how morphological defects influence the charge transport, dynamic simulation and scanning Kelvin probe microscopy have been used. The molecular dynamics simulations of polycrystalline TIPS-pentacene films show that the disruption of the molecular packing at the grain boundaries leads to energetic barriers for hole transport and potential wells for electrons (Figure 1.7a). The height of the energy barriers will be further enhanced when the voids occur at the grain boundaries.

Furthermore, the impact of grain boundaries on charge transport is dependent on the angle between adjacent domains. Low-angle grain boundary and high-angle grain boundary are schematically shown in Figure 1.7b. A low-angle grain boundary represents a slight misorientation between individual grain domains, whereas a high-angle grain boundary is associated with a high degree of packing misorientation. The occurrence of a high-angle grain

boundary for slip-stacked packing leads to an energy barrier that hinders inter-grain transport. Conversely, a low-angle grain boundary gives rise to a lower transport barrier for herringbone packing (Figure 1.7).[63]

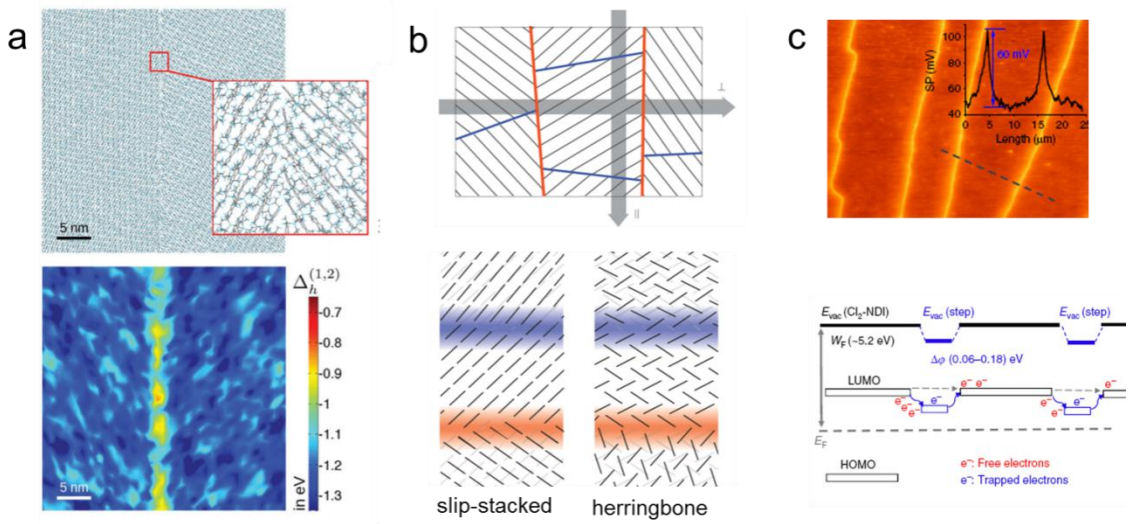

Figure 1.7. (a) Energetic barriers at the grain boundary of TIPS-pentacene crystal.[64] (b) Low-angle grain boundary and high-angle grain boundary models.[63] (c) Electron traps at the step edges on the surface of OSC crystal.[65]

The step edges on the surface of OSC single crystal FETs also influence the charge carrier transport. The high-resolution surface potential mapping obtained by scanning Kelvin probe microscopy is shown in Figure 1.7c. It shows that crystal step edges on the surface of n-type OSCs induce the positive potential that can trap electron impeding the transport. Micro-electrostatic calculations suggest that the step edges trapping can be intrinsic to crystals of the molecule with polar substituents.[65]

1.3 Physical processes during solution processing

The control of self-assembly of OSCs by solution processing is an efficient method to tune molecular organization and film morphology for high performance electronic devices. In this section, I present the main physical processes during film deposition, such as solvent evaporation, fluid flow, crystallization and self-assembly.

1.3.1 Solvent evaporation

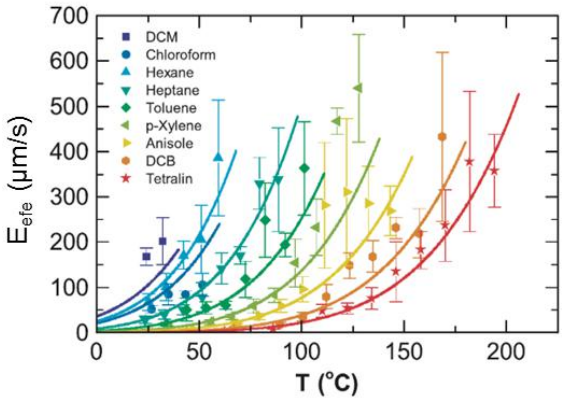

Figure 1.8. Equilibrium front evaporation rate (E_{efe}) of different solvents during an edge-casting experiment measured at different substrate temperatures.[66]

During solution processing, solvent evaporation dominates the dynamics and kinetics of OSC self-assembly and crystallization. For instance, spin-coated OSC films often exhibit low crystallinity and less ordered molecular organization due to an insufficient time scale induced by a high evaporation rate (E). In contrast, for drop-casting, an evaporation front originates at the three-phase contact line. The movement of the evaporation front depends on the non-uniform evaporation rate.[67] As a consequence, a concentration gradient is formed at the evaporation front, driving the nucleation and crystal growth of OSCs. Similarly, during meniscus-guided coating, solvent evaporation plays an important role on the OSC film formation.[68] For instance, during dip-coating of TIPS-pentacene, continuous and uniform crystals are obtained over large areas with high crystallinity by using low boiling point solvents, such as dichloromethane.[69]

Control over evaporation rate by solvent selection is an efficient way to achieve highly ordered crystalline films. The relation between evaporation rate and coating speed (v) significantly influences the crystal growth of OSCs. Figure 1.8 shows the equilibrium front evaporation rate (E_{efe}) of common solvents at different temperatures, which is obtained by the edge-casting geometry. It shows that the evaporation rate of a solvent is determined by the

boiling point, temperature, and solvent vapor atmosphere. A predictive model for optimizing coating speed is proposed based on E_{efe}, which is applicable to a variety of solvents and substrate temperatures. In this way, a large area crystalline film of C8-BTBT has been obtained by zone-casting.[66]

1.3.2 Fluid flow

Various fluid flow processes are involved in OSC solution processing, such as non-uniform evaporation induced capillary flow (Figure 1.9a), surface tension (γ_{LV}) induced Marangoni flow (Figure 1.9b), and substrate movement induced Couette flow (Figure 1.9c,d).[70] For drop-casting, the fluid flow is influenced by the solvent evaporation and surface tension gradient. The strength (fluid velocity) of the capillary flow is determined by the non-uniform evaporation rate over the surface of the droplet (Figure 1.9a).[71] In the presence of a surface tension gradient, fluid will flow from regions of low surface tension to those of high surface tension. This gradient manifests as a shear stress along the surface which induces recirculating flow in the bulk by mass balance (Figure 1.9b).[72] Therefore, capillary flow and the recirculating Marangoni flow govern the morphology of drop-cast OSC films.

The fluid flow during meniscus-guided coating is more complex than during drop-casting, since the viscous force imposed by the substrate will induce Couette flow near the substrate.[73] Figure 1.9c shows that during dip-coating the flow streamline ending at the stagnation point defines the boundary between an “upward flow region”, which continues into the coating film, and a “recirculation region”, which extends back to the bulk liquid. The positon of the stagnation position (x_{sp}) can influence the thickness of the dip-coated film.[73] For solution shearing, the streamline of various fluid flows is illustrated in Figure 1.9d. The fluid velocity profile under the bulk solution is a combination of pressure-driven (parabolic) and boundary-driven (linear) flow. The fluid at the meniscus is determined by capillary flow,

Marangoni flow and couette flow, during the mass transport of OSCs, resulting in a concentration gradient at the meniscus for the film growth.[74]

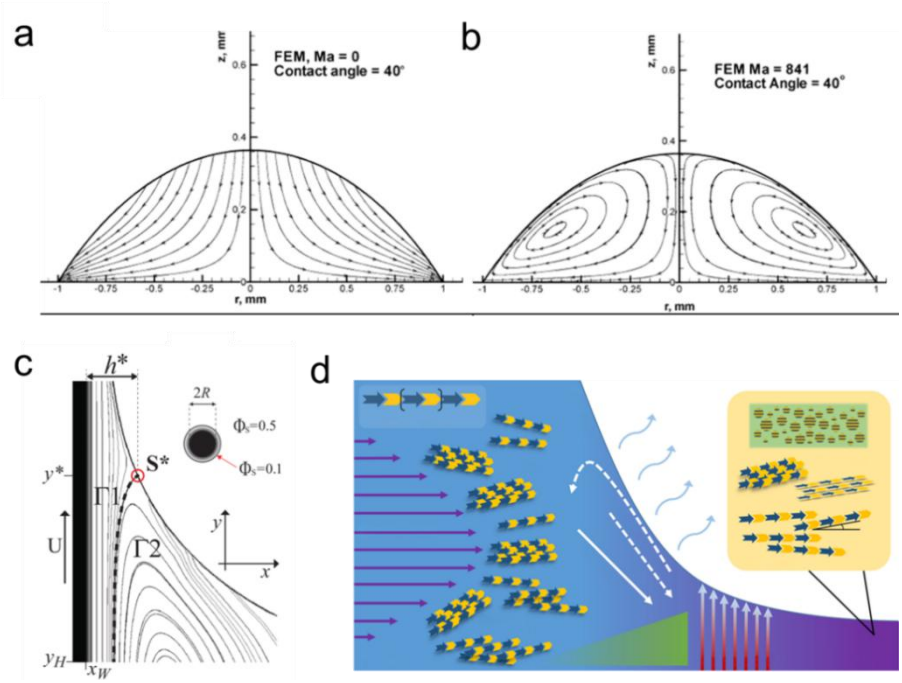

Figure 1.9. (a) Capillary flow[71] and (b) Marangoni flow during drop-casting.[72] (c) Upward flow and recirculation flow regions during dip-coating.[73] (d) Various fluid flow during solution shearing.[74]

1.3.3 Crystallization

The crystallization of OSCs includes nucleation and crystal growth. The nucleation begins with the appearance of small molecular clusters (nuclei) and the phase transformation is associated with Gibbs free energy change (ΔG).[75] This free energy change comprises a change in the volume (bulk) free energy (ΔG_V) due to altered intermolecular interactions within the nascent phase, and a change in surface energy (ΔG_S) due to the creation of a new interface between the nucleus and surrounding fluid.[58] As for a spherical nucleus with a critical radius of r^*, the crystal growth can arise when $r > r^*$ due to the decrease of net ΔG (Figure 1.10a). ΔG^* (at $r = r^*$) is the crucial free energy change for nucleation.

During solution processing, the OSC crystallization is driven by the supersaturated concentration. The supersaturation increases with concentration and a certain amount of

supersaturation can overcome ΔG* for nucleation (Figure 1.10b). For a two-dimensional spherical homogenous nucleation from solution, the energy barrier of ΔG^*_{hom} is determined by concentration (c), solubility (δ), temperature (T), and the surface energy between liquid and crystals (γ_{CL}),

$$\Delta G^*_{hom} = \frac{16\pi^3\gamma_{CL}^3}{3(k_BT)^3\left(\ln\left(\frac{c}{\delta}\right)\right)^2} \qquad \text{Equation (1.5)}$$

where k_B is Boltzmann's constant.

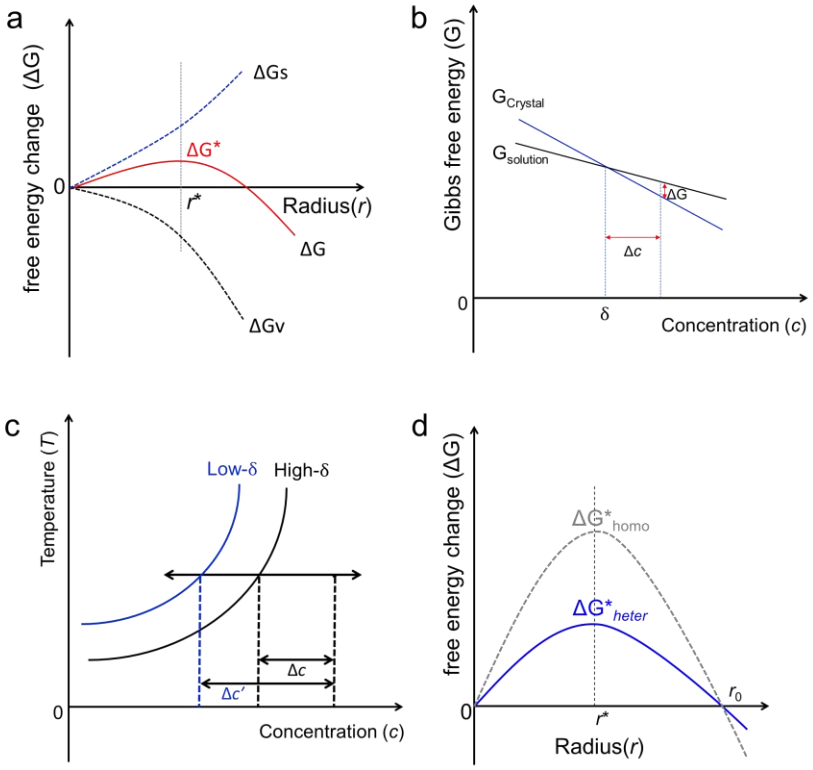

Figure 1.10. (a) Change of Gibbs free energy during crystallization.[76] (b) Gibbs free energy of crystal and solution as a function of solute concentration. (c) Influence of solubility on supersaturation. (d) Nucleation barrier for homogeneous and heterogeneous nucleation.

Figure 1.10c shows that the supersaturation (Δc) is determined by concentration and solubility. For a particular concentration, a low solubility solvent can contribute a higher supersaturation as compared to a high solubility solvent. Therefore, optimizing the solubility during solution processing is a promising route to control the crystallization. As for two-dimensional spherulite heterogeneous nucleation, the substrate surface energy (γ_{SV}) and the

roughness of the substrate also affect the nucleation barrier, which can be described by Equation (1.6), wherein $f(\vartheta)$ is a shape factor influenced by the surface energy of the substrate.

$$\Delta G^*_{heter} = \Delta G^*_{hom} f(\vartheta) = \frac{16\pi^3 \gamma^3_{c-s}}{3(k_B T)^3 \left(\ln\left(\frac{c}{\delta}\right)\right)^2} f(\vartheta) \qquad \text{Equation (1.6)}$$

$$f(\vartheta) = \frac{(2+cos\vartheta)(1-cos\vartheta)^2}{4} \qquad \text{Equation (1.7)}$$

Therefore, the surface energy of the substrate impacts the nucleation barrier for heterogeneous nucleation, ΔG^*_{heter}.[76] For instance, a high surface energy leads to a low $f(\vartheta)$, reducing the nucleation for heterogeneous crystallization (Figure 1.10d).[77]

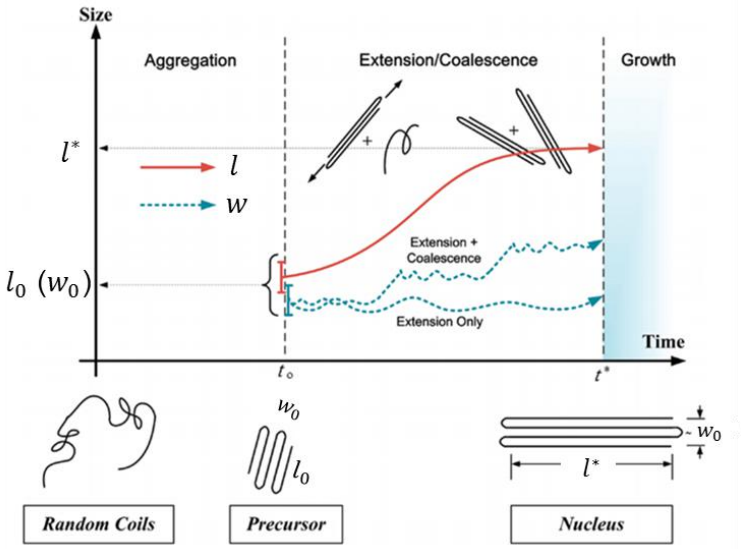

Figure 1.11. Schematic illustration of the nucleation process of polymers in solution: from random coils to precursor and nucleus. *l* and *w* represent the axial and the lateral dimensions of the aggregated precursor. The incipient precursor is characterized by an initial axial length l_o significantly shorter than the critical axial length *l** of fully developed nucleus.[78]

The self-assembly of polymer OSCs in solution is more complex and exhibit experimental difficulties in studying the nucleation process due to the limited size and transient lifetime. Molecular dynamics simulations for the solution-state provides understanding about the self-assembly of simple polymers in solution. Figure 1.11 shows the molecular dynamics results for the nucleation process of PE from random coils in 1,2,4 trichlorobenzene (TCB) solution. The nucleation of PE in solution starts from segmental aggregation into incipient precursors of axial length l_o and comparable lateral width w_o. This

is followed by single-precursor extension into new segments and stems, and the nearby precursors can coalesce via diffusion and oriented attachment, with concomitant axial readjustments to reach l^* and a slight increase in lateral width w. The nucleation process ends here and further stem attachment would correspond to crystal growth.[78] In contrast to simple polymers like PE, conjugated polymers have relatively rigid backbones. The π-π interactions are the primary intermolecular forces in addition to the associative dispersion forces among the alkyl side chains. Thus, pre-aggregates of conjugated polymer often occur in solution due to strong π-π interactions of the backbones.[74]

1.4 Solution processing techniques

Various solution processing techniques were developed during the last decades to obtain thin OSC films for transistor applications. In this section, I discuss the development of solution processing techniques based on spin-coating, drop-casting and meniscus-guided coating, respectively.

1.4.1 Spin-coating

Spin-coating is a widely used solution processing method to deposit uniform film, in which the high angular velocity spreads the OSC solution over the substrate surface and leads to a high solvent evaporation rate. The thickness of spin-coated films is inversely related to spin-coating speed and depends on the solution concentration and viscosity. Since the viscosity of a polymer OSC increases with solution concentration, spin-coating is commonly used to obtain homogenous polymer OSC films. For instance, by spin-coating of P3HT from chlorobenzene at 1500 rpm, the solvent will be almost completely removed and the P3HT solidification is completed in only ten seconds after the substrate spinning is initiated (Figure 1.12a).[79] Due to the insufficient time scale for OSC self-assembly, spin-coated P3HT films

typically exhibit a less ordered molecular organization. The self-assembly progress of P3HT during spin-coating is illustrated in Figure 1.12b. At the first stage of spin-coating, an edge-on oriented layer grows rapidly on the substrate interface, followed by a slower growth of mixed edge-on and face-on layers that form as top bulk layer. The growth of ultrathin ordered interfacial layer and disordered bulk of P3HT results from the competing crystallization at the polymer-substrate interface and polymer-air interface.[80]

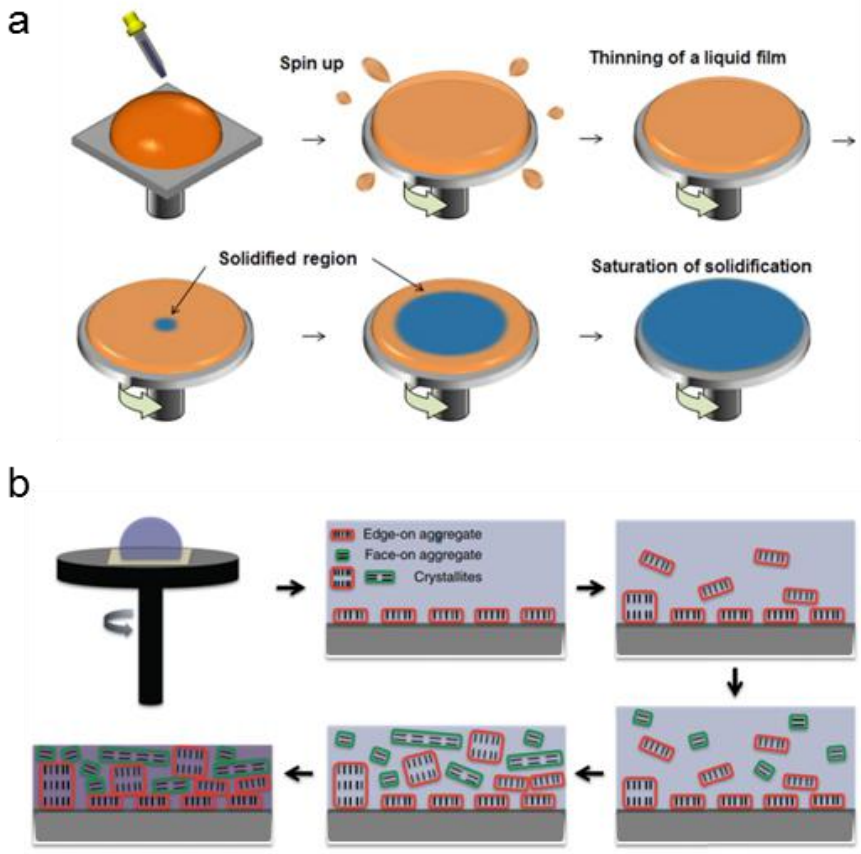

Figure 1.12. (a) P3HT solidification process during of spin-coating.[79] (b) P3HT self-assembly progress during spin-coating.[80]

In contrast to spin-coating of polymer OSCs, spin-coating of small molecule OSCs suffers from dewetting and non-continuous morphology. On-the-fly-dispensing spin-coating provides an efficient method to overcome dewetting and improves the film formation of small molecule OSCs. When the solution is dispensed on the substrate at high rotation rate, the tangential force breaks the static wetting balance on the hydrophobic substrate and enables a quick solution spreading over the substrate within only 0.03 second, leading to the formation

of an ultrathin film (Figure 1.13a).[81] N-type transistors based on ultrathin-crystalline films of small molecule, core-expanded NDIs fused with 2-(1,3-dithiol2-ylidene)malonitrile groups (NDI-DTYM2), processed in this way exhibit an excellent device performance with maximum electron mobility over 1.0 cm^2 V^{-1} s^{-1}. Channel restriction self-assembly during spin-coating is shown Figure 1.13b, wherein photoresist patterns were utilized as template to grow aligned crystalline OSC arrays. This strategy enables the large-scale fabrication of small molecule OSC arrays with accuracy and reliability. [82]

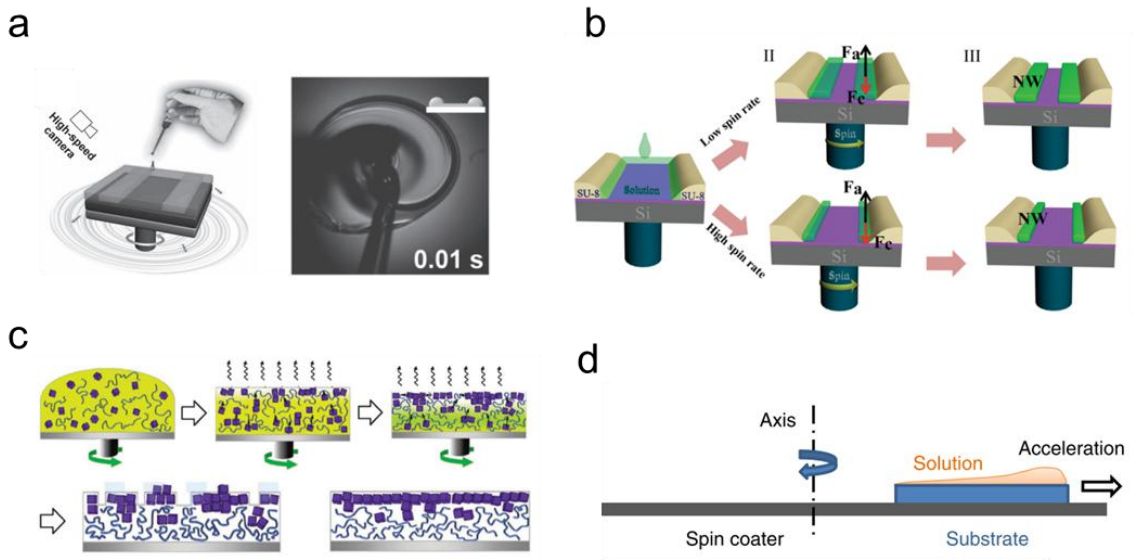

Figure 1.13. (a) On-the-fly-dispensing spin-coating.[81] (b) Channel restricted self-assembly during spin-coating,[82] (c) Self-assembly process during spin-coating OSC:polymer blend.[83] (d) Off-center spin-coating of OSC:polymer blend.[41]

Spin-coating of blends of small molecule OSC and insulating polymer is another method to prevent dewetting and provide the possibility for the small molecule OSCs to crystallize at the OSC/polymer interface (Figure 1.13c). By controlling the solvent evaporation rate during spin-coating, the phase separation of the two components diF-TES-ADT and PMMA can be regulated, which in turn determines the structural development of diF-TES-ADT in the PMMA matrix.[83] Furthermore, ultrahigh mobilities above 25 cm^2 V^{-1} s^{-1} were achieved by off-center-spin-coating of a C8-BTBT:polystyrene (PS) blend, which

was attributed to the formation of a highly aligned, meta-stable crystal packing and vertical phase separation (Figure 1.13d).[41]

1.4.2 Drop-casting

Drop casting is a basic and low-cost method for the fabrication of OSC films. During drop-casting, an evaporation front occurs at the substrate-solution contact line. Thus, the nucleation and self-assembly starts from the contact line and gradually moves to the center region of the drop (or substrate). Its advantages over spin-coating include less OSC wastage and sufficient time scale for OSC self-assembly.[84] Therefore, drop-cast films generally show better charge transport as compared to spin-coated films due to the improved molecular organization, induced by a slower growth processes.[85]

During drop-casting of polymer OSCs, the molecular organization can be tuned from edge-on to face-on through selecting appropriate solvents. For example, the molecular orientation of poly[(5,6-difluoro-2,1,3-benzothiadiazol-4,7-diyl)-alt-(3,3'''-di(2-octyldodecyl)-2,2',5',2'',5'', 2'''-quaterthiophen-5,5'''-diyl)] (PffBT4T-2OD) polymer is edge-on when drop-cast from $CHCl_3$. Interestingly, the edge-on packing is changed to face-on through the gradual adding of TCB into $CHCl_3$. The distinct molecular-orientations are attributed to the different solubility of the polymer in both solvents and the slow film growth process (Figure 1.14a).[60]

A slow solvent evaporation also has been demonstrated to assist the crystallization of small molecule OSCs. Highly ordered crystalline structures of α,ω-dihexylquaterthiophene (DH4T) have been obtained by drop-casting from 1,2-dichlorobenzene, which evaporated over a long time of around 1-2 days. The resulting highly crystalline DH4T exhibits a hole mobility around 0.05-0.1 $cm^2\ V^{-1}\ s^{-1}$.[85] Solvent vapor enhanced drop-casting (SVED) and solvent vapor diffusion provide a convenient route to tune the evaporation time, ensuring the formation of homogenous and ordered OSC layers (Figure 1.14b).[86] For instance, single

crystal OFETs of dithieno[2,3-d;2′,3′-d′]benzo[1,2-b;4,5-b′]dithiophene (DTBDT) obtained by solvent vapor diffusion exhibit a high mobility of more than 3 $cm^2 V^{-1} s^{-1}$. [87]

However, drop-cast films are prone to exhibit non-uniform morphology due to the free solvent evaporation, especially for small molecule OSCs. As shown in Figure 1.15 a, during drop-casting of TIPS-pentacene at free evaporation conditions, the undesirabe "coffee ring pattern" is disadvantageous to the device performance.[88] Covering a drop-cast sample by a glass container is a simple and convenient way to tune solvent evaporation and improve OSC film morphology. Fig 1.15b shows that aligned crystalline morphology of TIPS-pentacene was obtained under controlled evaporation (sample covered by a container).

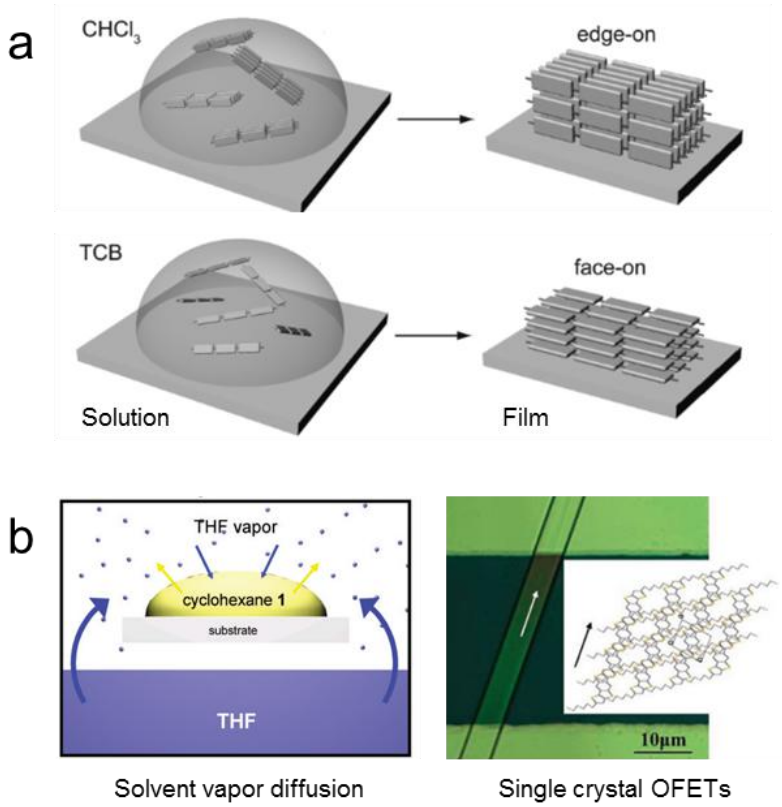

Figure 1.14. (a) Molecular organization controlled by solvent selection during drop-casting.[60] (b) Solvent vapor diffusion to enhance the evaporation time for single crystal OFETs.[87]

In addition, drop-casting on an inclined substrate also induces aligned OSC growth. Aligned N,N′-bis(n-octyl)-x:y,dicyanoperylene-3,4:9,10-bis(dicarboximide) (PDI8-CN2) was obtained in this way, in which the slow-moving evaporation front promotes the growth of

oriented crystalline morphologies.[63] Droplet pinned crystallization is another efficient method to achieve aligned crystals (Figure 1.15c). Here, a small piece of silicon wafer was used to obtain a steady receding contact line shown as Figure 1.15c. The evaporation front slowly moves from the substrate edge and the narrow meniscus results in a steep concentration gradient. As a consequence, an aligned fullerene (C60) single crystal is obtained, exhibiting a high electron mobility of around 11 $cm^2 V^{-1} s^{-1}$.[89] In addition, mixing two solvents with distinct boiling point and surface tension is also efficient to govern the fluid flow and OSC self-assembly. In the case of a mixed-solvent of dodecane and chlorobenzene, the capillary flow and Marangoni flow contribute to the aligned crystalline morphology of TIPS-pentacene (Figure 1.15d).

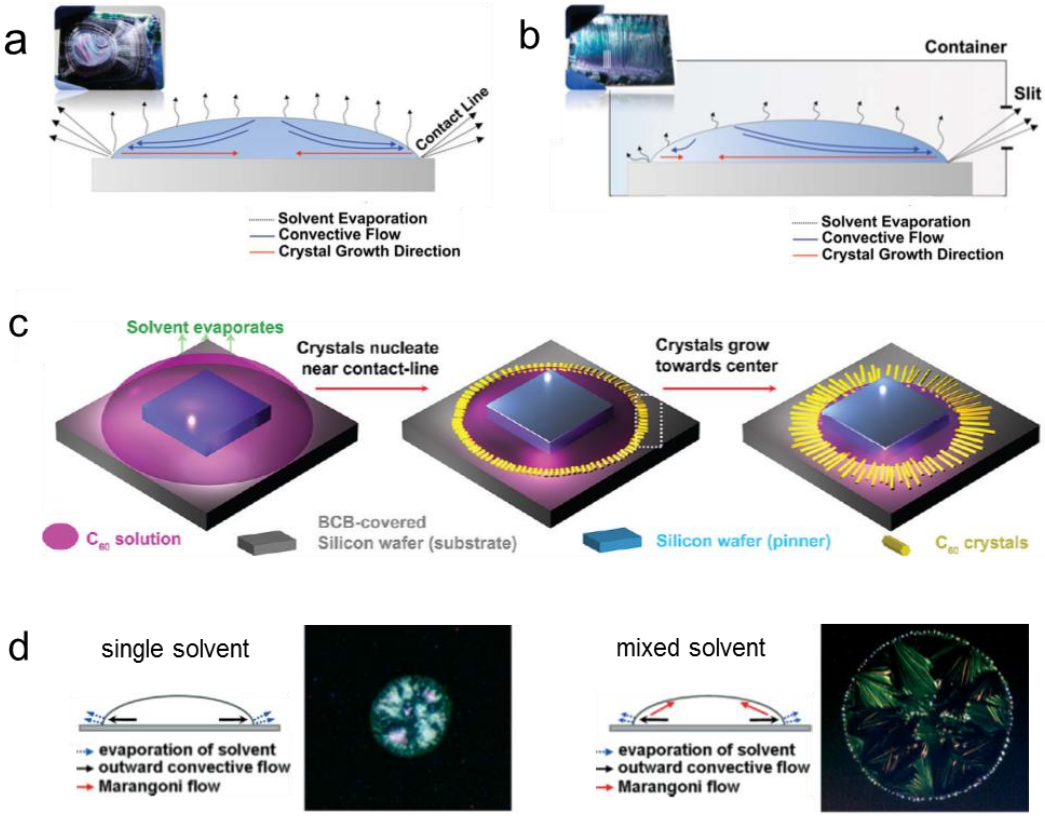

Figure 1.15. (a) Free and (b) controlled solvent evaporation during drop-casting of TIPS-pentacene. [88] (c) Meniscus control for the growth of aligned C60 crystals.[89] (d) Fluid flow control by mixed-solvent during inkjet printing. [90]

Substrate modification provides an approach to tune the nucleation sites, which is called “surface selective deposition”. As shown in Figure 1.16a, different functional groups are used to pattern the substrate into wetting and non-wetting regions. Small molecule OCSs only nucleate at the wetting area, while the non-wetting region repels the OSC solution and inhibits crystal growth. In this way, highly crystalline C8-BTBT films are obtained at the wetting area.[91] To further control the OSC crystallization at the selective area, the wetting regions are patterned into an asymmetric geometry, as shown in Figure 1.16b. Through two solvent inkjet-printing, dimethylformamide solvent and C8-BTBT/$CHCl_3$ solution were dropped at the patterned area in sequence. As a result, an asymmetric solution volume is formed by the asymmetric surface patterns. The nucleation of C8-BTBT occurs preferentially at the protuberance position due to the high surface-area to volume ratio, resulting in a high solvent evaporation rate. Crystalline C8-BTBT thin films grown with this approach reveal a high hole mobility above 10 $cm^2\ V^{-1}\ s^{-1}$.[92]

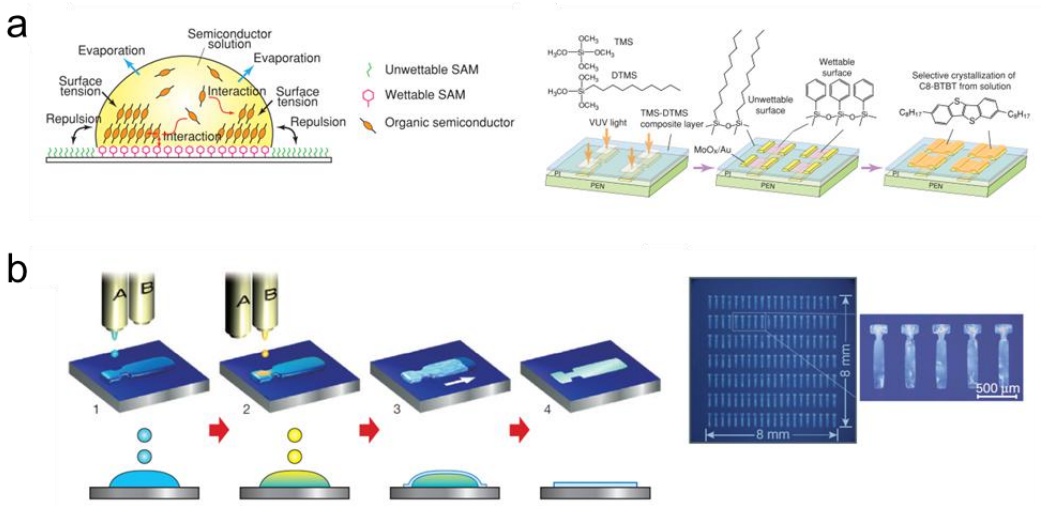

Figure 1.16. (a) Surface selective deposition on patterned wetting and non-wetting substrate.[91] (b) Inkjet printing single crystal films with anti-solvent on asymmetric patterned substrate.[92]

1.4.3 Meniscus-guided coating

Meniscus-guided coating refers to the control of the solution meniscus to grow OSC films, including dip-coating, zone-casting, bar-coating, blade-casting and solution

shearing.[13] Meniscus-guided coating techniques have attracted great attention due to the possibility to deposit aligned morphologies and highly ordered molecular organizations. According to the relation between coating speed and film thickness, meniscus-guided coating is classified into an evaporative, a Landau-Levich, and a mixed-regime (Figure 1.17).[93] The evaporative regime is characterized by a decrease in film deposition thickness (h) as a function of increasing coating speed ($h \propto v^{-1}$). As for the Landau-Levich regime, film deposition thickness increases with coating speed, since high coating speed drags out OSC by viscous force. The transition region is called mixed regime and the minimum film thickness is expected to occur in the mixed regime. During meniscus-guided coating, the film formation and electronic device performance of the obtained films are highly dependent on the relation between solvent evaporation rate and coating speed. The right balance between coating speed and mass transport will contribute to a homogenous crystalline OSC film with high coverage ratio and desired device performance.

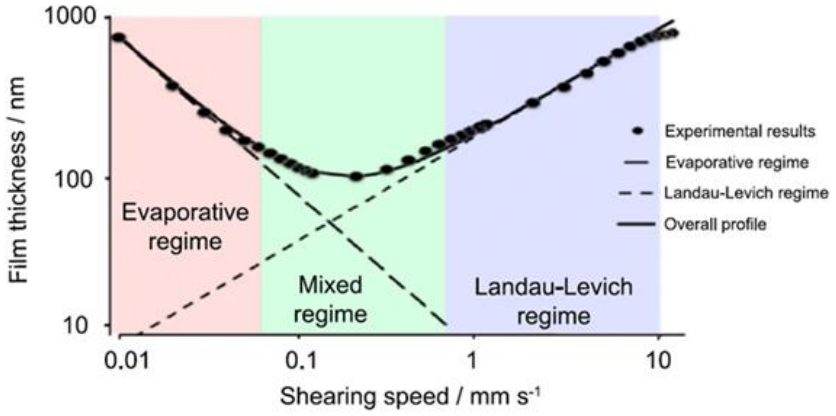

Figure 1.17. (a) Deposition regimes of meniscus-guided coating characterized by differences in film thickness. The regimes are classified into evaporation, Landau-Levich, and mixed-regimes.[74]

Dip-coating is an ideal method to prepare OSC thin layers due to its simplicity, easiness to operate, low-cost and waste-free process. It offers a good control over the OSC film thickness.[94] As shown in Figure 1.18a, a meniscus is formed between substrate and bulk solution during withdrawing the substrate. At optimized dip-coating speed, DTBDT can

be crystallized and grown into dendritic crystalline thin layers.[95] In addition to the control of coating speed, simple wire-bar-coating process[50], blade-casting, and solution shearing[96] provide the possibility of tuning the substrate temperature while zone-casting[97] involves controlling both substrate and solution temperature.[50, 98] Highly ordered DPPDTT and hexa-n-dodecylhexa-peri-hexabenzocoronene (HBC-C12) films are obtained by bar-coating and zone-casting, respectively, as shown in Figure 1.18b,c. Furthermore, meniscus-guided coating of OSC:polymer binder blends also has been used to improve the electronic performance of OFETs. A large-area OSC crystalline film can be obtained from blade-casting of an OSC:polymer blend (Figure 1.18d). As a result, high charge carrier mobilities above 10 cm^2 V^{-1} s^{-1} can be achieved for 3,11-didecyldinaphtho[2,3-d:2′,3′-d′]benzo[1,2-b:4,5-b′]dithiophene (C10–DNBDT–NW)/PMMA or above 6 cm^2 V^{-1} s^{-1} for diF-TES-ADT/PS.[99, 100]

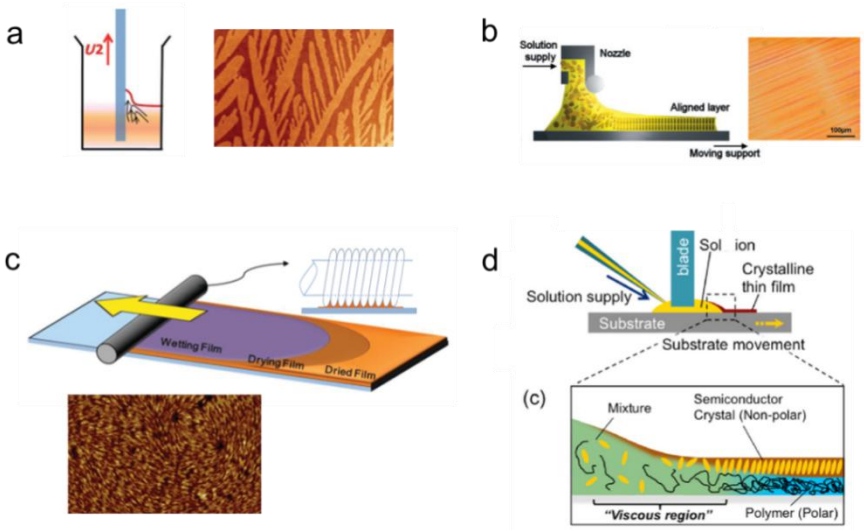

Figure 1.18. (a) Dip-coating[95] and (b) zone-casting of small molecule OSCs.[97] (c) Bar-coating of polymer OSC.[50] (d) Blade casting of OSC:polymer blend.[99]

To better control the OSC film growth by meniscus-guided coating, a micro-patterned substrate and micropillar templated blade have been utilized. Figure 1.19a shows that patterned triangle wetting regions were used to tune the nucleation sites of small molecule OSCs. Through solution shearing on pattered substrate, large area crystals of TIPS-pentacene

have been achieved by the triangle wetting patterns.[101] In the case of polymer OSCs, an ionic-liquid-based dynamic template can be employed to tune the nucleation barrier of the polymer. High birefringence of ionic-liquid-templated films arises from a high degree of alignment or crystallinity (Figure 1.19b).[102] Micropillar templated blade and micro-photoresist channel also have been employed to control the fluid flow and guide OSC film growth.[103, 104] The illustration of the micropillar based solution shearing is shown in Figure 1.19c, in which a high flow velocity occurs between the adjacent pillar. The increased fluid flow enhanced crystallization contributes to highly ordered and aligned TIPS-pentacene crystalline films, leading to a hole mobility between 1.0 and 8.0 $cm^2 V^{-1} s^{-1}$. In another work, aligned single crystalline domains were obtained by channel-restriction controlled self-assembly, as shown in Figure 1.19d.[104] The restricted meniscus with small-size evaporation front allows to rationally control the evaporation and convective flow in the photoresist channels. The homogeneous nucleation can occur along the photoresist channels, enabling the highly aligned growth of an OSC array with uniform morphology and orientation.

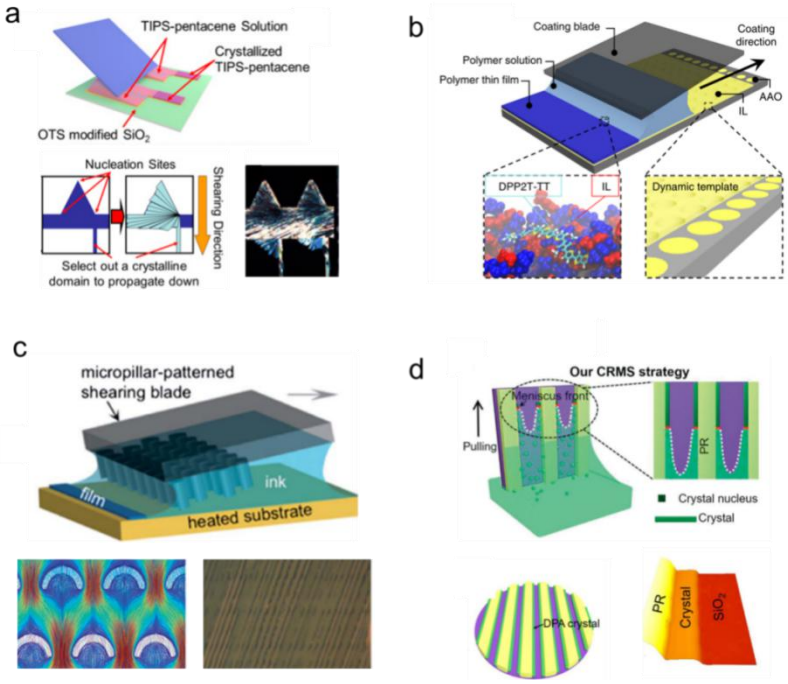

Figure 1.19. (a) Controlled nucleation by patterned substrate.[101] (b) Dynamic-template-directed multiscale assembly.[102] (c) Micro-pillar assisted solution shearing.[103] (d) Channel restriction assisted self-assembly[104].

1.5 Motivation

Over the past 30 years, many pioneering studies on the design and synthesis of OSCs as well as on solution processing have significantly improved the performance of OFETs. As a consequence, OFETs with mobilities above 10 $cm^2 V^{-1} s^{-1}$ have been realized with a variety of small molecule and polymer OSCs.[2, 24, 53, 104] However, the mechanism of the molecular self-assembly and film growth during solution processing is still not fully understood. A fundamental understanding of the involved physical processes during OSC deposition including solvent evaporation, fluid flow, mass transport, concentration gradient, crystallization and phase separation, would greatly support the development of printed organic electronics.[74]

Up to now, fundamentals of the deposition regimes for meniscus-guided coating (relation between coating speed and film thickness) and nucleation (patterned surface wetting) have been well understood. However, the exploration of the correlation between deposition parameters, physical processes and microstructural evolution in thin films is still not complete. The need of combined experimental and computational studies on solution processing of OSCs towards a new insight on the crystallization mechanism is significant.

1.5.1 Role of conjugation length on molecular self-assembly

Molecular structure of OSCs has a key impact on the film morphology and charge transport in OFETs. For instance, the molecular weight of P3HT greatly influences the formation of nanofibers and the side chains of benzothiadiazole-cyclopentadithiophene (CDT-BTZ) copolymer significantly impact the molecular packing.[105, 106] As for small molecule OSCs, a wide range of studies focused on side chain and end groups that impact the molecular packing and film morphology.[39, 107, 108] However, there is little exploration on the role of conjugation length on the self-assembly behavior of small molecule OSCs.

The influence of the conjugation length of small molecule OSCs on the electronic performance of thin film transistors includes two factors. On one hand, the conjugation length leads to different crystallization ability that impacts the molecular microstructure and thus influence charge carrier transport. On the other hand, the conjugation length of small molecule OSCs influences the HOMO/LUMO that determines the charge injection.

In Chapter 2, I focus on the control of the self-assembly and transistor characteristics of an analogous set of pyrene-functionalized diketopyrrolopyrroles (pyrene-DPPs) obtained by "successive incorporation" of DPP motifs. The well-defined pyrene-DPP analogues are systematically examined in correlation of (i) conjugation length of pyrene-DPPs and (ii) the solution-processing conditions employed for the thin film formation. Especially, extending the π-conjugation length of the DPP core is found to reduce the self-assembly ability, but leads to a transition from unipolar to ambipolar OFET characteristics.

1.5.2 Influence of polymer binder on OSC crystallization

Drop-casting and SVED exhibits advantages on controlling the self-assembly of small molecule OSCs and promoting high crystallinity.[86, 87] However, the misaligned crystals often impede the charge carrier transport in OFETs. As discussed in Chapter 1.4.3, meniscus-guided coating is an efficient technique to deposit OSC thin films with well controlled morphologies.[104] To overcome the challenge of depositing small molecule OSCs into large-area, uniform, and continuous crystalline films, blending insulating polymer with small molecule OSCs has been employed to improve the film-forming ability.[100, 109, 110] Even though the phase separation between OSC and insulating polymer is well understood, there are no studies on the influence of polymer binder on OSC crystallization.[100]

In Chapter 3, a new method is presented based on dip-coating a blend consisting of OSC and insulating polymer to control the crystallization of OSCs. A small fraction of amorphous polymer binder efficiently improves the morphology and alignment of dip-coated

small molecule OSCs. The improved crystallization during dip-coating is attributed to two mechanisms: first, the polymer binder leads to a viscosity gradient at the meniscus during dip-coating, facilitating the draw of solute and thus mass transport. Second, the polymer binder solidifies at the bottom layer, providing an appropriate nucleation barrier height of small molecule OSC.

1.5.3 Impact of meniscus shape on OSC crystallization

Meniscus-guided coating yields aligned and highly crystalline morphologies of conjugated small molecules and polymers.[50] Strategies on modulating meniscus-guided coating techniques to achieve high charge carrier mobility have been developed, but only little insight on the fundamentals of the fluid mechanics on the crystal growth of OSCs has been provided. An in-depth study of the role of meniscus shape on fluid mechanical phenomenon and the pivotal fluid mechanical effect on OSC crystallization mechanism are still lacking.

In Chapter 4, I demonstrate the impact of the meniscus shape on the fluid flow and crystallization of OSCs during meniscus-guided coating. The developed angle-dependent dip-coating (ADDC) allows precisely controlling the meniscus shape (meniscus angle). A small meniscus angle favors the upward flow in the meniscus, shifting the stagnation point away from the contact line and increasing the concentration gradient. This fluid flow assisted crystallization at small meniscus angle weakens at elevated nucleation barriers, but strengthens by high supersaturation. The resulting aligned crystalline film with high surface coverage favors the charge carrier transport in C8-BTBT based field-effect transistors.

1.5.4 Coating speed governed morphology formation

Various physical processes are involved during meniscus-guided coating, including solvent evaporation, fluid flow, mass transport, concentration gradient, OSC nucleation and crystallization. The investigation of these physical processes is complex and challenging, but

essential to precisely control the OSC film growth.[58] For instance, the study of the evaporation rate provides a predictive model for optimizing coating speed.[66] The understanding of the fluid flow also favors the development of meniscus-guided coating.[111] However, there is only little work on the dynamics and kinetics of the crystallization process. Comprehensive understanding of the crystallization mechanism of OSCs during meniscus-guided coating is still lacking.

Therefore, in Chapter 5, I focus on the role of zone-casting speed on the nucleation and crystal growth of small molecule DPP(Th_2Bn)$_2$. Precise control of the size of spherulitic and aligned crystals was achieved by zone-casting at appropriate processing temperature. In the evaporation regime, the domain sizes of spherulitic DPP(Th_2Bn)$_2$ increases with the decrease of coating speed. At relatively low speed the spherulites exhibit aligned morphology. The phase field simulation of the in-plane crystallization demonstrates that a slower coating speed leads to lower nucleation density, and thus large crystal domain. A further slow coating speed leads to the aligned morphology owing to the disappearance of nucleation point at the evaporation front. This work demonstrates that the crystal growth during meniscus-guided coating is governed by coating speed and concentration gradient.

References

1. M. Kuik, G.J. Wetzelaer, H.T. Nicolai, N.I. Craciun, D.M. De Leeuw and P.W. Blom, *Adv. Mater.*, 2014, **26**(4): 512-531.
2. H. Dong, X. Fu, J. Liu, Z. Wang and W. Hu, *Adv. Mater.*, 2013, **25**(43): 6158-6183.
3. H. Sirringhaus, *Adv. Mater.*, 2014, **26**(9): 1319-1335.
4. H.-C. Liao, C.-C. Ho, C.-Y. Chang, M.-H. Jao, S.B. Darling and W.-F. Su, *Mater. Today*, 2013, **16**(9): 326-336.
5. S.J. Benight, C. Wang, J.B.H. Tok and Z. Bao, *Prog. Polym. Sci.*, 2013, **38**(12): 1961-1977.
6. Y. Yao, H. Dong and W. Hu, *Adv. Mater.*, 2016, **28**(22): 4513-4523.
7. T. Someya, Z. Bao and G.G. Malliaras, *Nature*, 2016, **540**(7633): 379-385.
8. T. Lei, M. Guan, J. Liu, H.C. Lin, R. Pfattner, L. Shaw, A.F. McGuire, T.C. Huang, L. Shao, K.T. Cheng, J.B. Tok and Z. Bao, *Proc. Natl. Acad. Sci.*, 2017, **114**(20): 5107-5112.
9. O. Knopfmacher, M.L. Hammock, A.L. Appleton, G. Schwartz, J. Mei, T. Lei, J. Pei and Z. Bao, *Nat. Commun.*, 2014, **5**: 2954.
10. S. Wang, J. Xu, W. Wang, G.N. Wang, R. Rastak, F. Molina-Lopez, J.W. Chung, S. Niu, V.R. Feig, J. Lopez, T. Lei, S.K. Kwon, Y. Kim, A.M. Foudeh, A. Ehrlich, A. Gasperini, Y. Yun, B. Murmann, J.B. Tok and Z. Bao, *Nature*, 2018, **555**(7694): 83-88.
11. X. Yang, *Semiconducting Polymer Composites: Principles, Morphologies, Properties and Applications*, John Wiley & Sons, 2012.
12. X. Guo, M. Baumgarten and K. Müllen, *Prog. Polym. Sci.*, 2013, **38**(12): 1832-1908.
13. Y. Diao, L. Shaw, Z. Bao and S.C.B. Mannsfeld, *Energy Environ. Sci.*, 2014, **7**(7): 2145-2159.
14. D. Khim, Y. Xu, K.J. Baeg, M. Kang, W.T. Park, S.H. Lee, I.B. Kim, J. Kim, D.Y. Kim, C. Liu and Y.Y. Noh, *Adv. Mater.*, 2016, **28**(3): 518-526.
15. A. Salleo, *Mater. Today*, 2007, **10**(3): 38-45.
16. A. Facchetti, *Mater. Today*, 2007, **10**(3): 28-37.
17. E.C.P. Smits, T.D. Anthopoulos, S. Setayesh, E. van Veenendaal, R. Coehoorn, P.W.M. Blom, B. de Boer and D.M. de Leeuw, *Phys. Rev. B*, 2006, **73**(20): 205316.
18. K. Zhou, H. Dong, H.L. Zhang and W. Hu, *Phys. Chem. Chem. Phys.*, 2014, **16**(41): 22448-22457.
19. R. Schmechel, M. Ahles and H. von Seggern, *J. Appl. Phys.*, 2005, **98**(8): 084511.

20. D. A. Neamen, *Semiconductor physics and devices: basic principles*, Irwin, 1992.
21. V. Podzorov, *Nat. Mater.*, 2013, **12**(11): 947-948.
22. Y. Yamashita, J. Tsurumi, F. Hinkel, Y. Okada, J. Soeda, W. Zajaczkowski, M. Baumgarten, W. Pisula, H. Matsui, K. Mullen and J. Takeya, *Adv. Mater.*, 2014, **26**(48): 8169-8173.
23. C. Liu, T. Minari, X. Lu, A. Kumatani, K. Takimiya and K. Tsukagoshi, *Adv. Mater.*, 2011, **23**(4): 523-526.
24. X. Xu, Y. Yao, B. Shan, X. Gu, D. Liu, J. Liu, J. Xu, N. Zhao, W. Hu and Q. Miao, *Adv. Mater.*, 2016, **28**(26): 5276-5283.
25. H. Geng, Q. Peng, L. Wang, H. Li, Y. Liao, Z. Ma and Z. Shuai, *Adv. Mater.*, 2012, **24**(26): 3568-3572.
26. C. Liu, Y. Xu and Y.-Y. Noh, *Mater. Today*, 2015, **18**(2): 79-96.
27. I.E. Jacobs and A.J. Moule, *Adv. Mater.*, 2017, **29**(42): 1703063.
28. T. Minari, T. Miyadera, K. Tsukagoshi, Y. Aoyagi and H. Ito, *Appl. Phys. Lett.*, 2007, **91**(5): 053508.
29. T. Minari, and C. Liu, *Origin of large contact resistance in organic field-effect transistors*, 2013 IEEE International Interconnect Technology Conference-IITC.
30. B. de Boer, A. Hadipour, M.M. Mandoc, T. van Woudenbergh and P.W.M. Blom, *Adv. Mater.* , 2005, **17**(5): 621-625.
31. X. Cheng, Y.-Y. Noh, J. Wang, M. Tello, J. Frisch, R.-P. Blum, A. Vollmer, J.P. Rabe, N. Koch and H. Sirringhaus, *Adv. Funct. Mater.* , 2009, **19**(15): 2407-2415.
32. M. Kano, T. Minari and K. Tsukagoshi, *Appl. Phys. Lett.*, 2009, **94**(14): 143304.
33. N.B. Kotadiya, H. Lu, A. Mondal, Y. Ie, D. Andrienko, P.W.M. Blom and G.A.H. Wetzelaer, *Nat. Mater.*, 2018, **17**(4): 329-334.
34. Y. Don Park, J.A. Lim, H.S. Lee and K. Cho, *Mater. Today*, 2007, **10**(3): 46-54.
35. L. L. Chua, J. Zaumseil, J. F. Chang, E. C. W. Ou, P. K. H. Ho, H. Sirringhaus and R. H Friend, *Nature*, 2005, **434**(7030): 194.
36. M. Mamada, H. Katagiri, M. Mizukami, K. Honda, T. Minamiki, R. Teraoka, T. Uemura and S. Tokito, *ACS Appl. Mater. Interfaces*, 2013, **5**(19): 9670-9677.
37. J.H. Dou, Y.Q. Zheng, Z.F. Yao, Z.A. Yu, T. Lei, X. Shen, X.Y. Luo, J. Sun, S.D. Zhang, Y.F. Ding, G. Han, Y. Yi, J.Y. Wang and J. Pei, *J. Am. Chem. Soc.*, 2015, **137**(50): 15947-15956.
38. Q. Miao, *Adv. Mater.*, 2014, **26**(31): 5541-5549.

39. G. Schweicher, V. Lemaur, C. Niebel, C. Ruzie, Y. Diao, O. Goto, W.Y. Lee, Y. Kim, J.B. Arlin, J. Karpinska, A.R. Kennedy, S.R. Parkin, Y. Olivier, S.C. Mannsfeld, J. Cornil, Y.H. Geerts and Z. Bao, *Adv. Mater.*, 2015, **27**(19): 3066-3072.
40. I. Osaka, S. Shinamura, T. Abe and K. Takimiya, *J. Mater. Chem. C*, 2013, **1**(7): 1297-1304.
41. Y. Yuan, G. Giri, A.L. Ayzner, A.P. Zoombelt, S.C. Mannsfeld, J. Chen, D. Nordlund, M.F. Toney, J. Huang and Z. Bao, *Nat. Commun.*, 2014, **5**: 3005.
42. O. D. Jurchescu, S. Subramanian, R. J. Kline, S.D. Hudson, J. E. Anthony, T. N. Jackson and D. J. Gundlach, *Chem. Mater.*, 2008, 20(21): 6733-6737.
43. G. Generali, F. Dinelli, R. Capelli, S. Toffanin, F. di Maria, M. Gazzano, G. Barbarella and M. Muccini, *J. Phys. Chem. C*, 2011, **115**(46): 23164-23169.
44. Y. Qiao, Y. Guo, C. Yu, F. Zhang, W. Xu, Y. Liu and D. Zhu, *J. Am. Chem. Soc.*, 2012, **134**(9): 4084-4087.
45. T. Kakinuma, H. Kojima, M. Ashizawa, H. Matsumoto and T. Mori, *J. Mater. Chem. C*, 2013, **1**(34): 5395.
46. H. Yu, Z. Bao and J.H. Oh, *Adv. Funct. Mater.*, 2013, **23**(5): 629-639.
47. T. Marszalek, M. Li and W. Pisula, *Design directed self-assembly of donor-acceptor polymers*, *Chem. Commun.*, 2016, **52**(73): 10938-10947.
48. K. Mullen and W. Pisula, *J. Am. Chem. Soc.*, 2015, **137**(30): 9503-95035.
49. N. Kleinhenz, C. Rosu, S. Chatterjee, M. Chang, K. Nayani, Z. Xue, E. Kim, J. Middlebrooks, P.S. Russo, J.O. Park, M. Srinivasarao and E. Reichmanis, *Chem. Mater.*, 2015, **27**(7): 2687-2694.
50. D. Khim, H. Han, K.J. Baeg, J. Kim, S.W. Kwak, D.Y. Kim and Y.Y. Noh, *Adv. Mater.*, 2013, **25**(31): 4302-4308.
51. D. Khim, G.S. Ryu, W.T. Park, H. Kim, M. Lee and Y.Y. Noh, *Adv. Mater.*, 2016, **28**(14): 2752-2759.
52. S. Wang, W. Pisula and K. Müllen, *J. Mater. Chem.*, 2012, **22**(47): 24827.
53. Y. Yamashita, F. Hinkel, T. Marszalek, W. Zajaczkowski, W. Pisula, M. Baumgarten, H. Matsui, K. Müllen and J. Takeya, *Chem. Mater.*, 2016, **28**(2): 420-424.
54. Z.-F. Yao, J.-Y. Wang and J. Pei, *Cryst. Growth Des.*, 2017, **18**(1): 7-15.
55. M.A. Reyes-Martinez, A.J. Crosby and A.L. Briseno, *Nat. Commun.*, 2015, **6**: 6948.
56. E.J. Crossland, K. Tremel, F. Fischer, K. Rahimi, G. Reiter, U. Steiner and S. Ludwigs, *Adv. Mater.*, 2012, **24**(6): 839-844.

57. R. Noriega, J. Rivnay, K. Vandewal, F.P. Koch, N. Stingelin, P. Smith, M.F. Toney and A. Salleo, *Nat. Mater.*, 2013, **12**(11): 1038-1044.

58. B.B. Patel and Y. Diao, *Nanotechnology*, 2018, **29**(4): 044004.

59. M.S. Chen, J.R. Niskala, D.A. Unruh, C.K. Chu, O.P. Lee and J.M.J. Fréchet, *Chem. Mater.*, 2013, **25**(20): 4088-4096.

60. M. Li, C. An, T. Marszalek, M. Baumgarten, H. Yan, K. Mullen and W. Pisula, *Adv. Mater.*, 2016, **28**(42): 9430-9438.

61. K.V. Nguyen, M.M. Payne, J.E. Anthony, J.H. Lee, E. Song, B. Kang, K. Cho and W.H. Lee, *Sci. Rep.*, 2016, **6**:33224.

62. L.H. Jimison, M.F. Toney, I. McCulloch, M. Heeney and A. Salleo, *Adv. Mater.* , 2009, **21**(16): 1568-1572.

63. J. Rivnay, L.H. Jimison, J.E. Northrup, M.F. Toney, R. Noriega, S. Lu, T.J. Marks, A. Facchetti and A. Salleo, *Nat. Mater.*, 2009, **8**(12): 952-958.

64. F. Steiner, C. Poelking, D. Niedzialek, D. Andrienko and J. Nelson, *Phys. Chem. Chem. Phys.*, 2017, **19**(17): 10854-10862.

65. T. He, Y. Wu, G. D'Avino, E. Schmidt, M. Stolte, J. Cornil, D. Beljonne, P.P. Ruden, F. Wurthner and C.D. Frisbie, *Nat. Commun.*, 2018, **9**(1): 2141.

66. R. Janneck, F. Vercesi, P. Heremans, J. Genoe and C. Rolin, *Adv. Mater.*, 2016, **28**(36): 8007-8013.

67. E. Josten, E. Wetterskog, A. Glavic, P. Boesecke, A. Feoktystov, E. Brauweiler-Reuters, U. Rucker, G. Salazar-Alvarez, T. Bruckel and L. Bergstrom, *Sci. Rep.*, 2017, **7**(1): 2802.

68. M. He, B. Li, X. Cui, B. Jiang, Y. He, Y. Chen, D. O'Neil, P. Szymanski, M.A. Ei-Sayed, J. Huang and Z. Lin, *Nat. Commun.*, 2017, **8**:16045.

69. J. Jang, S. Nam, K. Im, J. Hur, S.N. Cha, J. Kim, H.B. Son, H. Suh, M.A. Loth, J.E. Anthony, J.-J. Park, C.E. Park, J.M. Kim and K. Kim, *Adv. Funct. Mater.*, 2012, **22**(5): 1005-1014.

70. Y. Tsoumpas, S. Dehaeck, A.Rednikov and P. Colinet, *Langmuir*, 2015, 31(49): 13334-13340.

71. H. Hu and R. G. Larson, *Langmuir*, 2005, **21**(9): 3963-3971.

72. H. Hu and R. G. Larson, *Langmuir*, 2005, **21**(9): 3972-3980.

73. C. E. Colosqui and J. F. Morris, *Phys. Rev. Lett.,* 2013, **110**(18): 188302.

74. X. Gu, L. Shaw, K. Gu, M.F. Toney and Z. Bao, *Nat. Commun.*, 2018, **9**(1): 534.

75. J. W. Mullin, *Crystallization*, Elsevier, 2001.

76. N.T. Thanh, N. Maclean and S. Mahiddine, *Chem. Rev.*, 2014, **114**(15): 7610-7630.
77. Y.Y. Diao and X.Y. Liu, *Adv. Funct. Mater.* , 2012, **22**(7): 1354-1375.
78. Y.-K. Lan and A.-C. Su, *Macromolecules*, 2010, **43**(19): 7908-7912.
79. J.Y. Na, B. Kang, D.H. Sin, K. Cho and Y.D. Park, *Sci. Rep.*, 2015, **5**: 13288.
80. D.T. Duong, M.F. Toney and A. Salleo, *Phys. Rev. B*, 2012, **86**(20).
81. F. Zhang, C.A. Di, N. Berdunov, Y. Hu, Y. Hu, X. Gao, Q. Meng, H. Sirringhaus and D. Zhu, *Adv. Mater.*, 2013, **25**(10): 1401-1407.
82. W. Deng, X. Zhang, L. Wang, J. Wang, Q. Shang, X. Zhang, L. Huang and J. Jie, *Adv. Mater.*, 2015, **27**(45): 7305-7312.
83. W.H. Lee, D. Kwak, J.E. Anthony, H.S. Lee, H.H. Choi, D.H. Kim, S.G. Lee and K. Cho, *Adv. Funct. Mater.* , 2012, **22**(2): 267-281.
84. K. Zhao, X. Yu, R. Li, A. Amassian and Y. Han, *J. Mater. Chem. C*, 2015, **3**(38): 9842-9848.
85. T. Leydecker, D. Trong Duong, A. Salleo, E. Orgiu and P. Samori, *ACS Appl. Mater. Interfaces*, 2014, **6**(23): 21248-55.
86. S. Wang, L. Dossel, A. Mavrinskiy, P. Gao, X. Feng, W. Pisula and K. Mullen, *Small*, 2011, **7**(20): 2841-2846.
87. S. Wang, P. Gao, I. Liebewirth, K. Kirchhoff, S. Pang, X. Feng, W. Pisula and K. Müllen, *Chem. Mater.*, 2011, **23**(22): 4960-4964.
88. C. Pitsalidis, N. Kalfagiannis, N.A. Hastas, P.G. Karagiannidis, C. Kapnopoulos, A. Ioakeimidis and S. Logothetidis, *RSC Adv.*, 2014, **4**(40): 20804-20813.
89. H. Li, B.C. Tee, J.J. Cha, Y. Cui, J.W. Chung, S.Y. Lee and Z. Bao, *J. Am. Chem. Soc.*, 2012, **134**(5): 2760-2765.
90. J.A. Lim, W.H. Lee, H.S. Lee, J.H. Lee, Y.D. Park and K. Cho, *Adv. Funct. Mater.* , 2008, **18**(2): 229-234.
91. T. Minari, C. Lui, M. Kano and K. Tskukagoshi, *Adv. Mater.*, 2012, **24**(2): 299-306.
92. H. Minemawari, T. Yamada, H. Matsui, J. Tsutsumi, S. Haas, R. Chiba, R. Kumai and T. Hasegawa, *Nature*, 2011, **475**(7356): 364-367.
93. M. L. Berre, Y. Chen and D. Baigl, *Langmuir*, 2009, **25**(5): 2554-2557.
94. D. Grosso, *J. Mater. Chem.*, 2011, **21**(43).
95. L. Li, P. Gao, W. Wang, K. Mullen, H. Fuchs and L. Chi, *Angew Chem Int Ed Engl*, 2013, **52**(48): 12530-12535.
96. S. Schott, E. Gann, L. Thomsen, S.H. Jung, J.K. Lee, C.R. McNeill and H. Sirringhaus, *Adv. Mater.*, 2015, **27**(45): 7356-7364.

97. W. Pisula, A. Menon, M. Stepputat, I. Lieberwirth, U. Kolb, A. Tracz, H. Sirringhaus, T. Pakula and K. Müllen, *Adv. Mater.*, 2005, **17**(6): 684-689.

98. A. Tracz, T. Pakula and J. K. Jeszka, *Mater. Sci.-Poland*, 2004, **22**(4): 415-421.

99. J. Soeda, T. Okamoto, C. Mitsui and J. Takeya, *Org. Electron.,* 2016, **39**: 127-132.

100. M.R. Niazi, R. Li, E. Qiang Li, A.R. Kirmani, M. Abdelsamie, Q. Wang, W. Pan, M.M. Payne, J.E. Anthony, D.M. Smilgies, S.T. Thoroddsen, E.P. Giannelis and A. Amassian, *Nat. Commun.*, 2015, **6**: 8598.

101. S. Park, G. Giri, L. Shaw, G. Pitner, J. Ha, J.H. Koo, X. Gu, J. Park, T.H. Lee, J.H. Nam, Y. Hong and Z. Bao, *Proc. Natl. Acad. Sci.*, 2015, **112**(18): 5561-5566.

102. E. Mohammadi, C. Zhao, Y. Meng, G. Qu, F. Zhang, X. Zhao, J. Mei, J.M. Zuo, D. Shukla and Y. Diao, *Nat. Commun.*, 2017, **8**:16070.

103. Y. Diao, B.C. Tee, G. Giri, J. Xu, H. Kim do, H.A. Becerril, R.M. Stoltenberg, T.H. Lee, G. Xue, S.C. Mannsfeld and Z. Bao, *Nat. Mater.*, 2013, **12**(7): 665-671.

104. W. Deng, X. Zhang, H. Dong, J. Jie, X. Xu, J. Liu, L. He, L. Xu, W. Hu and X. Zhang, *Mater. Today*, 2018.

105. R.J. Kline, M.D. McGehee, E.N. Kadnikova, J. Liu and J.M.J. Fréchet, *Adv. Mater.* , 2003, **15**(18): 1519-1522.

106. W. Pisula, H. Tsao, D. Dudenko, D. Cho, S. Puniredd, Y. Zhao, A. Mavrinskiy, J. Shu, M. Hansen, M. Baumgarten and K. Müllen, *Polymers*, 2013, **5**(2): 833-846.

107. F. Zhang, Y. Hu, T. Schuettfort, C.A. Di, X. Gao, C.R. McNeill, L. Thomsen, S.C. Mannsfeld, W. Yuan, H. Sirringhaus and D. Zhu, *J. Am. Chem. Soc.*, 2013, **135**(6): 2338-2349.

108. Y. Ren, A.K. Hailey, A.M. Hiszpanski and Y.L. Loo, *Chem Mater*, 2014, **26**(22): 6570-6577.

109. J. Smith, R. Hamilton, I. McCulloch, N. Stingelin-Stutzmann, M. Heeney, D.D.C. Bradley and T.D. Anthopoulos, *J. Mater. Chem.*, 2010, **20**(13): 2562.

110. W. Lee and Y. Park, *Polymers*, 2014, **6**(4): 1057-1073.

111. G. Qu, J.J. Kwok and Y. Diao, *Acc. Chem. Res.*, 2016, **49**(12): 2756-2764.

Chapter 2 Long-range molecular self-assembly of π-extended pyrene-functionalized diketopyrrolopyrroles

2.1 Introduction

Most solution-processable small molecule OSCs with meaningful carrier mobilities transport only one type of carriers (holes or electrons), and organic field effect transistors (OFETs) made thereof are said to be unipolar.[1, 2] Some of the best molecular OSCs have reached carrier mobilities >10 cm^2 V^{-1} s^{-1}, for both holes and electrons.[3, 4] In contrast, molecular OSCs with ambipolar characteristics are not common, and in general their hole and electron mobilities have remained modest and/or unbalanced. Molecular OSCs with established ambipolar behavior were in general vacuum-sublimed into films, and the few reported instances of solution-processable analogues have shown fairly low performance.[5-7] One of the main difficulties in achieving efficient charge transport with small molecules is related to the requirement for a high valence band edge and/or a low conduction band edge conducive to a sufficiently low band gap.[8] In turn, rational molecular design principles geared to the development of solution-processable ambipolar OSCs remain at the forefront of research on organic electronics.

In earlier studies, solution-processable DPP-based small molecules have been described as promising materials for OPVs and OFETs.[9] A few instances of DPP-based ambipolar small molecules with added strong electron-deficient units have been described, leading to balanced hole and electron mobilities of 0.01 cm^2 V^{-1} s^{-1}.[10, 11] In separate work, hydrogen-bonding DPP-based analogues with pronounced intermolecular interactions and suppressed LUMO energy level exhibited ambipolar behavior as well, with hole and electron mobilities as high as 0.01 cm^2 V^{-1} s^{-1}.[12] Therefore, DPP-based π-conjugated small molecules are promising candidates for use in ambipolar OFETs, but an efficient, rational

molecular design approach remains to be developed to further improve their ambipolar carrier transport characteristics towards higher mobility values and a controlled self-assembly.

In this Chapter, I describe an analogous set of pyrene-DPPs (namely, **SM1–3**) obtained by "successive incorporation" of DPP motifs to reveal the influence of conjugation length on self-assembly behavior and charge transport performance. SVED was utilized to control the film growth of **SM1-3**.[13, 14] Distinct crystal morphologies for **SM1-3** can be obtained from SVED with $CHCl_3$, whereas SVED with THF induces various fiber morphologies. In particular, extending the π-conjugation of the DPP core is found to mitigate the long-range self-assembly of **SM1–3** and, in turn, to lower crystal size and fiber length. Furthermore, extending the π-conjugation length by incorporating additional DPP motifs along the main-chain in **SM1-3** suppresses the LUMO level, which in turn promotes electron injection from the transistor gold electrode into the active layer. As a result, **SM3** exhibits mobilities of ca. 0.06 $cm^2\ V^{-1}\ s^{-1}$ for hole and ca. 0.02 $cm^2\ V^{-1}\ s^{-1}$ for electrons, which are among the best ambipolar carrier mobility values reported so far for solution-processed oligomeric systems.[1]

2.2 Pyrene-DPP analogues

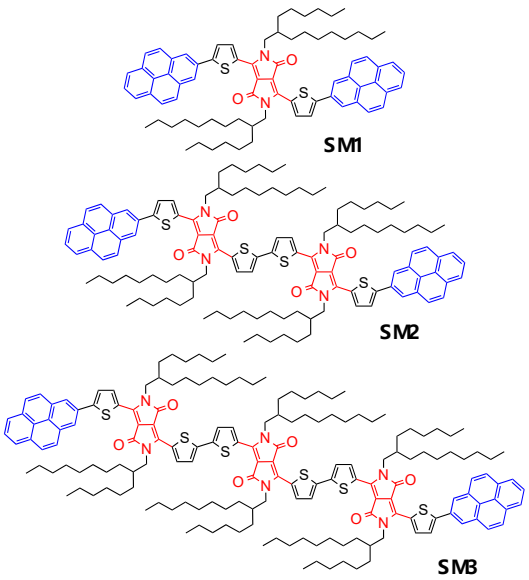

Figure 2.1. Molecular structure of Pyrene-DPP analogues **SM1-3**.

Figure 2.1 provides the molecular structures of the pyrene-DPP analogues **SM1-3** synthesized by Dr. Philipp Wucher. For this study the conjugation length was extended via incremental incorporation of DPP motifs and overall extension of π-conjugation. The incorporation of C2-symmetric pyrene end-groups is expected to promote the π-stacking of **SM1-3** and facilitate their long-range molecular self-assembly.

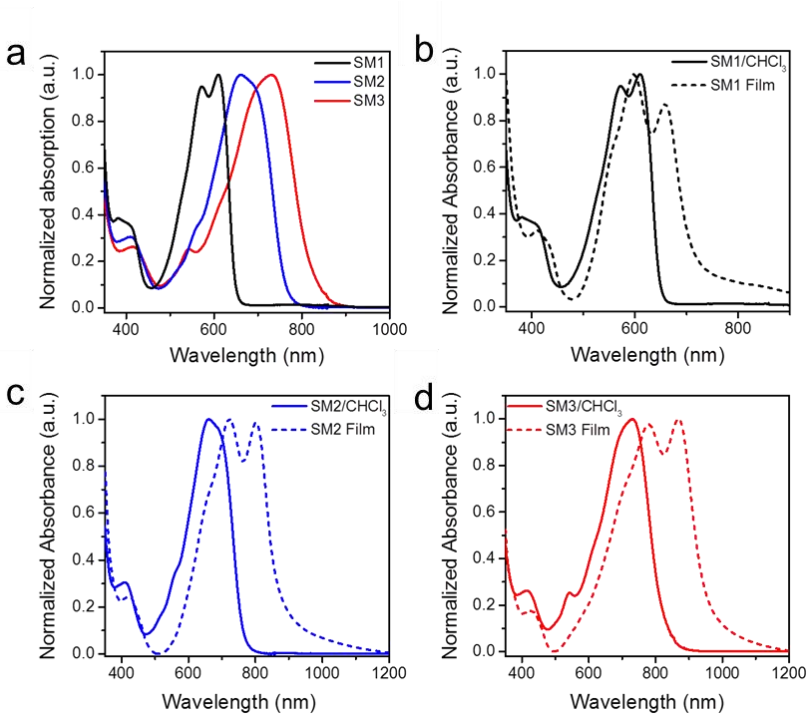

Figure 2.2. (a) Normalized solution ($CHCl_3$) optical absorption spectra of **SM1**, **SM2**, **SM3**; solution and spin-coated film optical absorption spectra for (b) **SM1**, (c) **SM2** and (d) **SM3**.

In Figure 2.2, the solution absorption of **SM1** in $CHCl_3$ shows two transition peaks (0-1 transition at ca. 571 nm and 0-0 transition at ca. 610 nm). The absorption peak of **SM2** is observed at ca. 660 nm (0-1 transition), with a long-wavelength shoulder at ca. 692 nm (0-0 transition). **SM3** exhibits the absorption peak at ca. 730 nm (0-0 transition) and a short-wavelength absorption shoulder at ca. 694 nm (0-1 transition). The absence of defined spectral features in **SM2** and **SM3** suggests that higher side-chain density resulting from the incorporation of several DPP motifs reduces π-aggregation. The thin-film optical absorption spectra of **SM1-3** provided in Figure 2.2b-d show significant red-shifts as π-conjugation extends from **SM1**, to **SM2** and to **SM3**: onsets of absorption shifting from ca. 700 nm, to ca.

900 nm, to ca. 1,000 nm in thin films, respectively. The appearance of two vibronic peaks and significant red shifts for spin-coated **SM1-3** films result from a much stronger aggregation in solid films than in solution.

As shown in Table 2.1, the ionization potentials (IP) determined by photoelectron spectroscopy in air (PESA) for **SM1-3** fall in the range (-) 5.0-5.2 eV (Carried out by Dr. Philipp Wucher). The electron affinity (EA) estimates are provided from consideration of the IP and optical gap (E_{opt}) values inferred from the onset of thin-film absorption: here EA values increases from (-) 3.36 eV to (-) 3.69 eV and to (-) 3.87 eV upon extending the π-conjugation as in **SM1**, **SM2** and **SM3**, respectively.

Table 2.1. Optical and electrochemical parameters for **SM1-3**, estimated by PESA and thin-film optical absorption.

Pyrene-DPPs	λ_{solu}[a] [nm]	λ_{film}[b] [nm]	E_{opt}[d] [eV]	IP[c] [eV]	EA[e] [eV]
SM1	571, 610	600, 660	1.72	-5.08	-3.36
SM2	660, 692*	722, 801	1.39	-5.08	-3.69
SM3	694*, 730	778, 874	1.28	-5.15	-3.87

[a] Optical absorption spectra in $CHCl_3$ solution. [b] Optical absorption spectra in thin films. [c] Estimated from the optical absorption spectra (films). [d] Estimated by photoelectron spectroscopy in air (PESA). [e] Inferred from PESA-estimated IPs and Eopt values. *Peak of absorption shoulder.

2.3 Spin-coating and drop-casting of pyrene-DPPs

To probe charge carrier transport in **SM1-3**, solution-processed OFETs were fabricated with a BGTC geometry on S_{HMDS}. Turning to spin-casting, homogeneous layers of **SM1-3** could easily be achieved from the 2 mg/mL $CHCl_3$ solution, and those were then subjected to thermal annealing at 150 °C to remove any residual solvent. Source and drain electrodes were deposited by gold evaporation. As shown in Figure 2.3 and Table 2.2, the hole mobility of spin-coated films of **SM1** was found to be 5×10^{-4} cm^2 V^{-1} s^{-1} and 2.5 - 4.0 $\times$ 10^{-3} cm^2 V^{-1} s^{-1} for **SM2** and **SM3**, respectively (Figure 2.3).

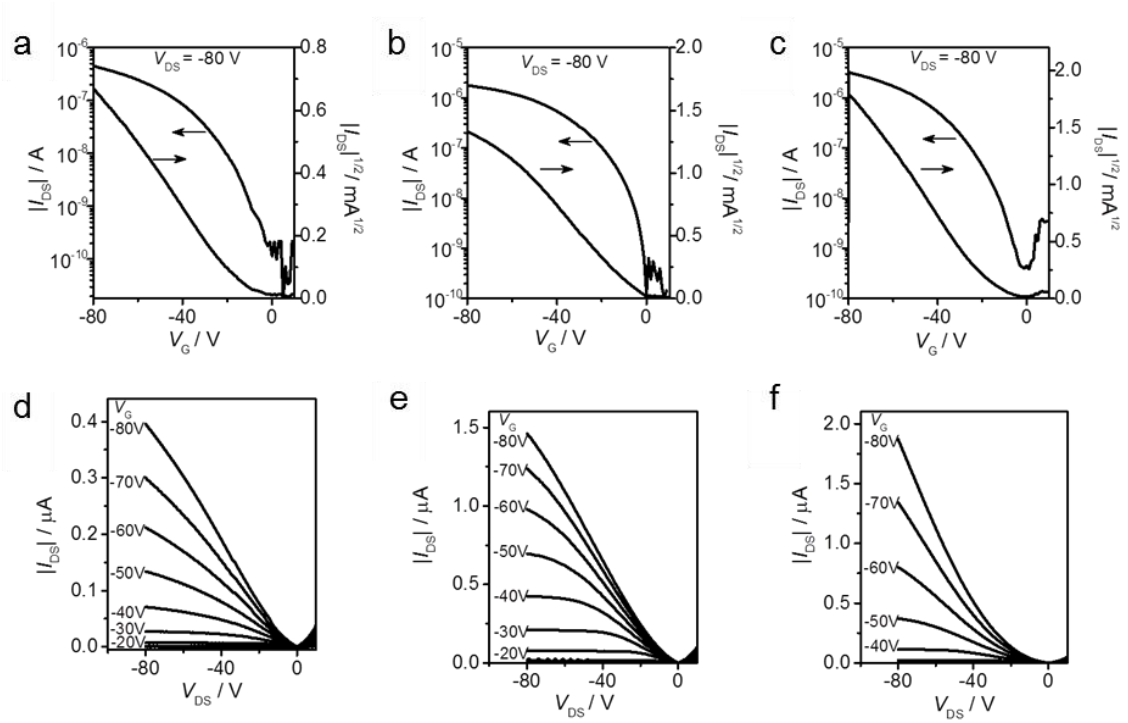

Figure 2.3. Transistor transfer (V_{ds}= -80 V) and output curves based on spin-coated **SM1-3** films obtained from a 2 mg/ml $CHCl_3$ solution on S_{HMDS}: (a, d) **SM1**, (b, e) **SM2**, and (c, f) **SM3**.

These relatively modest mobility values in spin-coated films can be attributed to the limited molecular ordering occurring in the rapid spin-coating and solidification steps (Figure 2.4). When **SM1-3** were drop-cast from a $CHCl_3$ solution at a concentration of 2 mg/ml, only inhomogeneous and disordered macroscopic patches could be obtained. Changing the concentration of **SM1-3** in $CHCl_3$ did not improve film quality.

Table 2.2. OFET characteristics of **SM1-3** processed by spin-coating from 2 mg/mL $CHCl_3$ solution.

Pyrene-DPPs	Spin-coating	μ_{hole} [cm^2V^{-1} s^{-1}]	V_T[V]
SM1	1000 rpm	$(5.2 \pm 1.3) \times 10^{-4}$	-14
SM2	1000 rpm	$(2.0 \pm 0.8) \times 10^{-3}$	-6
SM3	1000 rpm	$(4.2 \pm 0.7) \times 10^{-3}$	-16

Average value and standard deviation are calculated from 10 individual devices. BGTC transistors are fabricated after annealing 60 min at 150 °C based on S_{HMDS}.

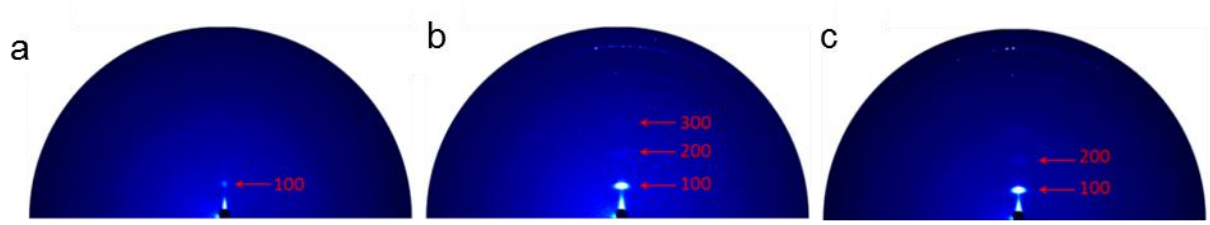

Figure 2.4. GIWAXS patterns of spin-coated **SM1-3** films obtained from a 2 mg/ml $CHCl_3$ solution on S_{HMDS}: (a) **SM1**, (b) **SM2**, and (c) **SM3**.

2.4 SVED of pyrene-DPPs

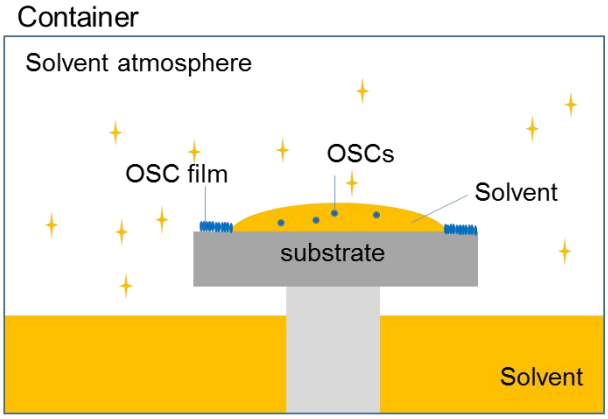

Figure 2.5. Solvent vapor enhanced drop-casting (SVED).

In order to improve the film-forming propensity and molecular organization of **SM1-3** in solution-cast layers, SVED approach shown as Figure 2.5 was followed to (i) minimize dewetting effects and (ii) mitigate the solvent evaporation rate.[13] During SVED, the drop-cast solution, deposited on a S_{HMDS}, was exposed to an atmosphere of saturated solvent vapor in a solvent container with a covered lid (nearly airtight). $CHCl_3$ was selected as the solvent because of its relatively low boiling point of 61.2 °C and high partial pressure, and because of the good solubility the **SM1-3** analogues in that solvent. And the solubility of **SM1-3** gradually decreased with the increase of conjugation length. The Hansen solubility parameters of $CHCl_3$, such as dispersion force, polar force and hydrogen bonding, are 17.8, 3.1 and 5.7, respectively.

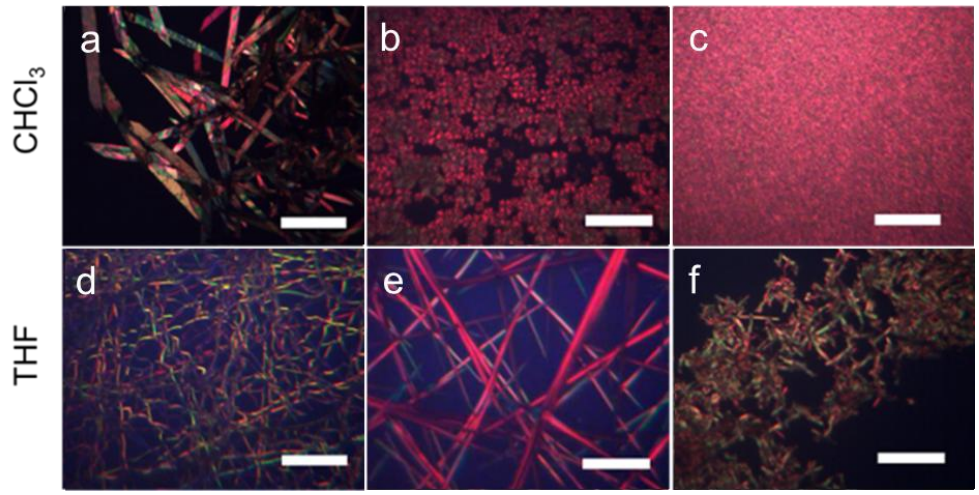

Figure 2.6. Polarized microscopy images of images of (a,d) **SM1**, (b,e) **SM2** and (c,f) **SM3** layers obtained by SVED from $CHCl_3$ (top images) and THF (bottom images). Scale bars: 100 μm.

As SVED processing protocol, 0.15 mL $CHCl_3$ solution of **SM1-3** at a concentration of 2 mg/mL was cast on the substrate and was subsequently exposed to saturated $CHCl_3$ vapor atmosphere. At the slow solvent evaporation rate during SVED, the concentration of **SM1-3** increased leading to a gradual self-assembly of **SM1-3**. After 8 hours, **SM1-3** solidified into semicrystalline films and were annealed at 150 °C for 60 min to remove residual solvent and promote an equilibrium molecular organization across the layers. In Figures 2.6a-c and 2.7a-c, the polarized optical microscopy and atomic force microscopy images of the thin films cast by SVED show the occurrence of very distinct morphologies and morphological length scales. In particular, crystal domain sizes are found to decrease on going from layers obtained with **SM1**, **SM2** and with **SM3**, i.e. as π-conjugation length extends across the Pyrene-DPP analogues. $CHCl_3$-mediated SVED leads to the formation of diamond-shaped crystals with **SM1**, with lengths and widths of 80-250 μm and 30-35 μm, respectively (thickness: 1.5-2 μm). In contrast, spherical-crystals are obtained with **SM2**, with diameters of 5-10 μm (thickness: 0.6-1 μm). Meanwhile, $CHCl_3$-mediated SVED yields a grain-like morphology with **SM3**, with significantly smaller features of 1-2 μm in size. The large crystallites developed in **SM1**-based layers are characteristic of long-range macroscopic order and, as a general trend,

microstructure size decreases for the more extended molecular analogues **SM2** and **SM3**, pointing to an evident correlation between molecular length and crystal feature size. By increasing the number of DPP motifs along the main-chain of the Pyrene-DPP analogues, the side-chain density also increases and, in turn, the self-assembly pattern of **SM1-3** changes with an apparent mitigation of aggregation as the density of pyrene end-groups decreases on going from **SM1** to **SM2** and to **SM3**.

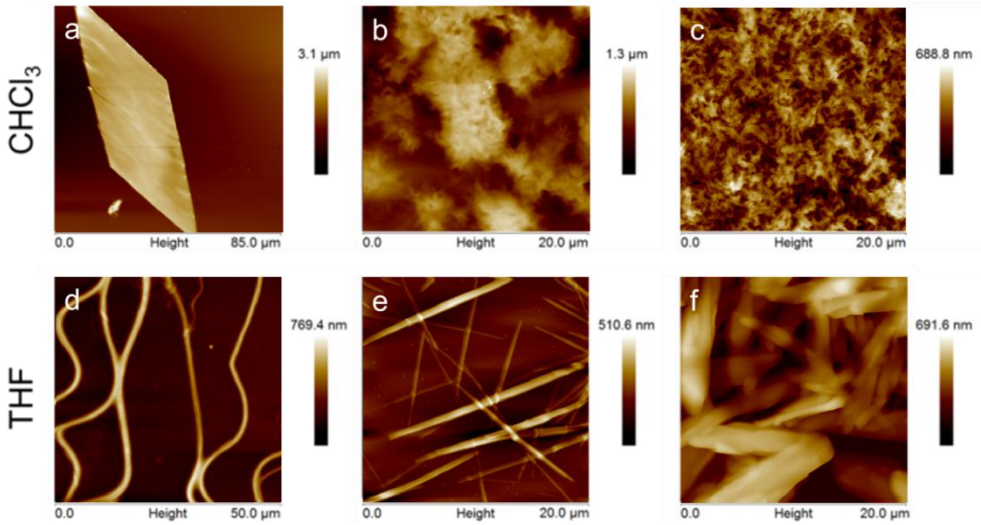

Figure 2.7. Tapping-mode of atomic force microscopy images of (a,d) **SM1**, (b,e) **SM2** and (c,f) **SM3** layers obtained by SVED from $CHCl_3$ (top images) and THF (bottom images).

The boiling point, polarity and solubility of the solvent greatly influence the thermodynamics and crystallization kinetics of π-conjugated, solution-processable molecules. To investigate the influence of solvent on the self-assembly of **SM1-3**, THF was taken as a second solvent for a direct comparison to $CHCl_3$, considering that both solvents possess a similar boiling point (65.4 °C for THF and 61.2 °C for $CHCl_3$) and close polarity (4.0 for THF and 4.1 for $CHCl_3$). It is important to note however that the Hansen solubility parameter of THF is different in the dispersion force, polar force and hydrogen bonding values of 16.8, 5.7 and 8.0, respectively.[15] In contrast to CHCl3, THF shows a lower dispersion force, but a higher polar force and hydrogen bonding power, suggesting that the solubility of **SM1-3** in THF may be lower than that in $CHCl_3$. For this reason, a longer time is actually needed for the

complete dissolution of **SM1-3** in THF, compared to $CHCl_3$. In addition, we observed a stronger propensity for **SM1-3** to aggregate in THF during the SVED processing step, compared to what we observed for $CHCl_3$-mediated SVED.

Figures 2.6d-f and 2.7d-f show that in THF-mediated SVED protocols, **SM1-3** self-order into various types of fibers in a wide range of length scale and aspect ratio. **SM1** forms one-dimensional wavelike-fibers, with lengths varying from 200 µm to 10 mm, while the widths of these fibers are 2-5 µm (thickness: 0.3-0.5 µm). As for **SM2**, needle-like fibers with smaller aspect ratios are formed that are 150 µm to 1 mm in length and 1-20 µm in width (thickness: 0.1-3 µm). In consistency with the outcome of the $CHCl_3$-mediated SVED protocol, **SM2** forms shorter fibers compared to **SM1** (likely due to the same reasons), and **SM3** forms the shortest fibers of 10-50 µm in length. These observations are in agreement with the correlation seen between molecular structure and self-assembly patterns for **SM1-3** subjected to the $CHCl_3$-mediated SVED protocol.

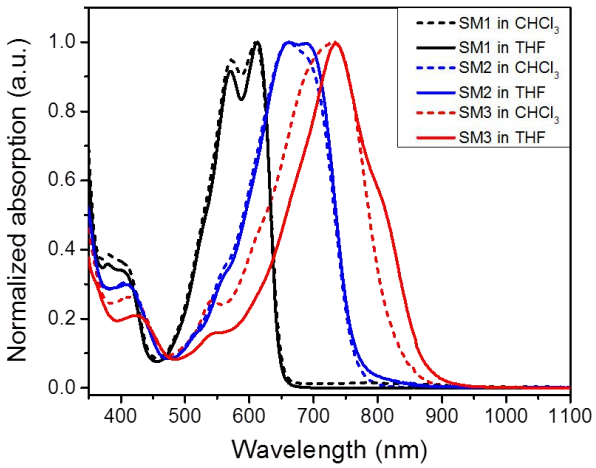

Figure 2.8. Normalized optical absorption spectra of **SM1-3** (0.01 mg/mL) in $CHCl_3$ (dash line) and THF (solid line).

The remarkable morphological differences observed comparing the self-assembly patterns of **SM1-3** from $CHCl_3$- and THF-mediated SVED is directly connected to the solubility and aggregation propensity differences of the **SM1-3** analogues in the two solvents. As stated earlier, the solubility of **SM1-3** in THF is slightly lower than in $CHCl_3$, owing to the

weaker molecule-solvent interactions between pyrene and THF. In Figure 2.8, the normalized solution optical absorption spectra of **SM1-3** (0.01 mg/mL) in THF and $CHCl_3$ imply that the aggregation of **SM1-3** in different solvents governs the film morphology. The optical absorption of **SM3** in THF exhibits a long-wavelength shoulder at 810 nm in contrast to $CHCl_3$, indicating **SM3** tends to form initial aggregates during THF-mediated SVED. The A_{0-0}/A_{0-1} ratios of **SM1-2** in THF are slightly higher than in $CHCl_3$, suggesting **SM1-2** may be more prone to self-assembly into aggregates due to their reduced solubility in THF.

2.5 Molecular organization

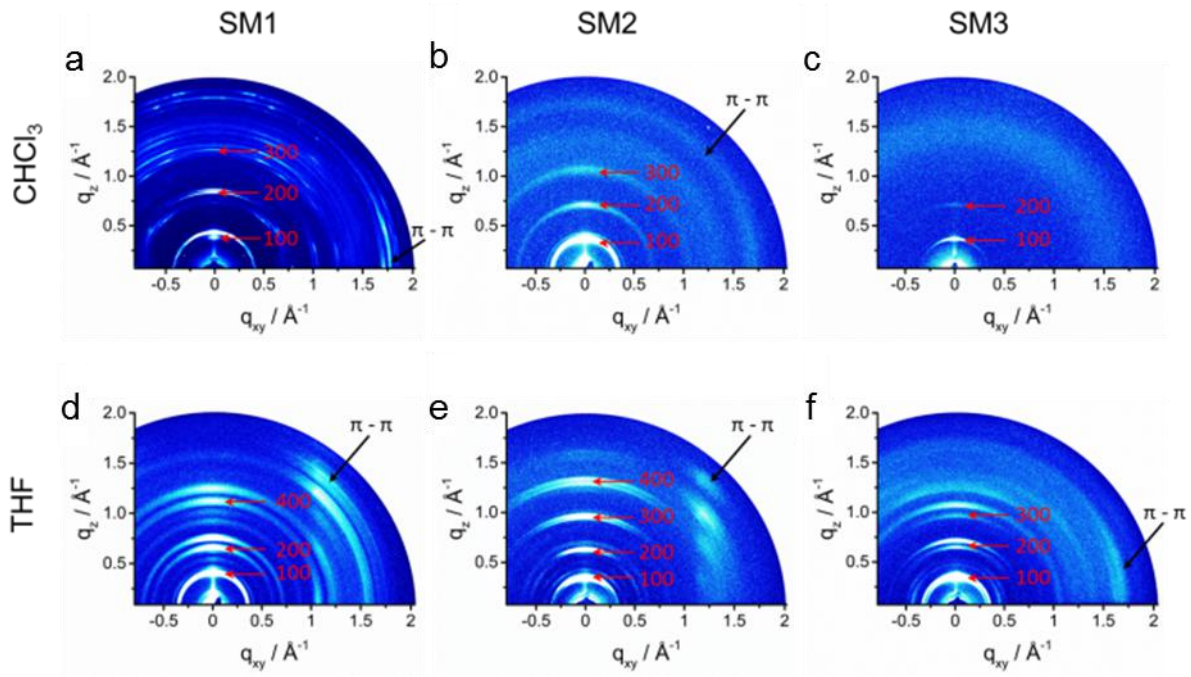

Figure 2.9. GIWAXS patterns of (a,d) **SM1**, (b,e) **SM2** and (c,f) **SM3** layers obtained by SVED from $CHCl_3$ (top images) and THF (bottom images). Reflections related to the layer structure and π-stacking are indicated in the patterns.

The correlated effects of π-conjugation length and side-chain density on the self-organization of the Pyrene-DPP analogues during the SVED treatment was further examined via grazing incidence wide-angle X-ray scattering (GIWAXS, performed by Dr. Tomasz Marszalek). The corresponding GIWAXS patterns are shown in Figure 2.9. The surface

orientation of **SM1-3** on the S_{HMDS}, as well as the interlayer and π-stacking distance parameters are summarized in Table 2.3. The GIWAXS pattern for $CHCl_3$-mediated SVED-processed **SM1** films shown in Figure 2.9a possesses a notably high number of reflections characteristic of a crystalline film. The distinct out-of-plane scattering intensity at $q_z = 0.43$ Å^{-1} for $q_{xy} = 0$ Å^{-1} is assigned to an interlayer distance of 14.6 Å and a preferential edge-on organization where the long molecular axis is aligned in the in-plane direction, parallel to the surface.

Table 2.3. Summary of the interlayer and π-stacking distance parameters for **SM1-3** as determined by GIWAXS. $R_{in/out}$ for the interlayer peak is derived to gain information about the surface arrangement. $R_{in/out} = 1$ - random crystal orientation on the surface; $R_{in/out} > 1$ - face-on; $R_{in/out} < 1$ – edge-on orientation of the molecules.

Pyrene-DPPs	SVED	Interlayer distance (Å)	π-stacking distance(Å)	$R_{in/out\ Interlayer}$ (-)
SM1	$CHCl_3$	14.6	3.5	0.02
SM2	$CHCl_3$	17.0	3.7	0.23
SM3	$CHCl_3$	17.0	-*	0.70
SM1	THF	16.5	3.5	0.07
SM2	THF	19.2	3.5	0.02
SM3	THF	19.2	3.5	0.02

*no corresponding reflection.

The surface arrangement of the molecules **SM1-3** is derived from the azimuthal intensity integration of the main 100 interlayer peak - marked in Figure 2.10a, which can be quantified by the $R_{in/out}$ parameter.[16] This value is defined as a ratio between the in-plane and the out-of-plane intensity of a corresponding reflection. If $R_{in/out}$ is equal 1, the azimuthal intensity distribution on the pattern is isotropic, indicating a random orientation of the crystals or domains on the surface. If the value is significantly higher or lower that 1, the film bears a preferential face-on or edge-on orientation of the molecules. For $CHCl_3$-mediated SVED-processed **SM1** films, a $R_{in/out} = 0.02$ points to an edge-on organization of the molecules relative to the substrate surface. The wide-angle off-equatorial reflection at $q_z = 0.47$ Å^{-1} for $q_{xy} = 1.77$ Å^{-1} is associated to a π-stacking distance of 3.5 Å between two pyrene units which

are tilted by about 15° with respect to the out-of-plane direction. This angle can be directly derived from the position of the maximum peak intensity of the π-stacking reflection. The π-stacking interactions between pyrene units of **SM1** molecules are proven by recently published single crystal data.[17] As shown in Figure 2.11, the DPP core is also titled, but by an angle of -15° with respect to the out-of-plane (cf. schematic illustration of the surface organization). The in-plane reflection at q_z = 0 $Å^{-1}$ and q_{xy} = 0.85 $Å^{-1}$ is associated to a distance of 0.74 nm and corresponds to two times the π-stacking value, as well as to the a parameter of the single crystal unit cell, implying a lateral shift of the molecules along their long axis.[17]

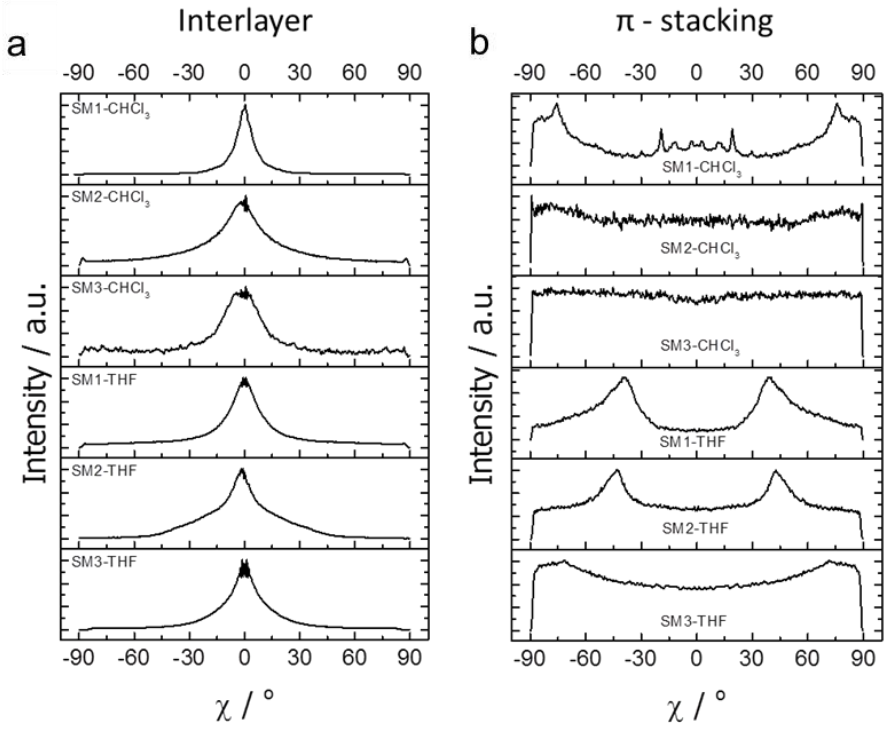

Figure 2.10. Azimuthally integrated intensity of (a) interlayer and (b) π-stacking reflections obtained for **SM1**, **SM2** and **SM3** films deposited from $CHCl_3$ and THF.

The GIWAXS pattern for THF-mediated SVED-processed **SM1** films shown in Figure 2.9d describes a larger interlayer and an identical π-stacking distance. The smearing out along the azimuthal direction set aside, the reflections are broader, suggesting slightly lower crystallinity compared to the films obtained by $CHCl_3$-mediated SVED (Figure 2.9a). For

THF-mediated SVED-processed **SM1** films, the pyrene units are tilted by a larger angle of ca 45° with respect to the out-of-plane as evident from the corresponding off-reflections at q_z = 1.37 $Å^{-1}$; q_{xy} = 1.23 $Å^{-1}$ assigned to the π-stacking (see Figure 2.9d - π-π), while the DPP main-chain maintains an orientation tilt of -15°. The larger tilt angle of the pyrene motifs with respect to the DPP main-chain inferred from GIWAXS analyses indicated a dihedral out-of-plane rotation of the pyrene moieties relative to the DPP core by ca. 30°. The surface arrangement/orientation of **SM1**, processed from $CHCl_3$ and THF, is schematically illustrated in Figure 2.11. The expansion of the interlayer distance from 14.6 Å to 16.5 Å by changing the solvent from changing the solvent from $CHCl_3$ to THF may be explained by subtle variations in alkyl side-chain packing and inter-digitation thereof in the films obtained from two different solvents. The degree of the surface alignment of **SM1** achieved from THF is slightly reduced in comparison to that seen in the crystals obtained from $CHCl_3$, as indicated by the rise of the $R_{in/out}$ parameter from 0.02 to 0.07.

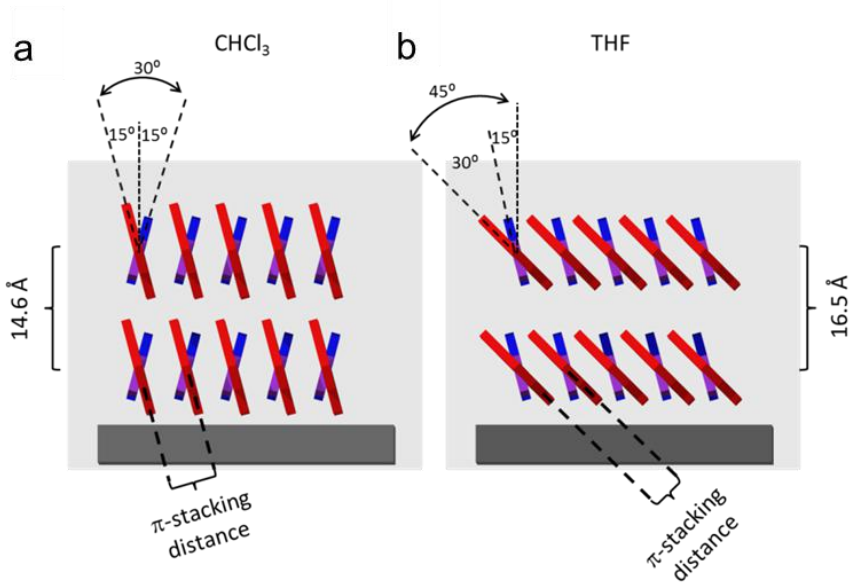

Figure 2.11. Side view of the schematic illustration for the organization of **SM1** in thin film deposited from a) $CHCl_3$ and b) THF. The pyrene units are indicated by red color, while the DPP core in blue. For the sake of simplicity, alkyl side chains are omitted.

Contrasting with the highly crystalline patterns of **SM1** obtained from $CHCl_3$-mediated SVED, Figure 2.9b,c show that self-organization in **SM2** and **SM3** is shorter-ranged,

as evident from the reduced number of reflections across the GIWAXS patterns. Both **SM2-3** analogues also show a layered organization with an interlayer spacing of about 17.0 Å and some extent of edge-on arrangement as indicated by the maximum intensity of the out-of-plane interlayer reflections (Figure 2.10). However, the domains are found to be more randomly ordered on the surface, as the $R_{in/out}$ parameter increases to 0.23 for **SM2** and 0.70 for **SM3**. The larger interlayer distance found for **SM2** and **SM3**, in comparison to **SM1**, can be explained by the greater number of DPP motifs in the former-motifs appended with sterically demanding branched side-chains.[18] The near-identical interlayer distance estimated for **SM2** and **SM3** can be related to subtle changes in the in-plane organization relative to the surface. Both compounds are only weakly in-plane packed (Figure 2.10), as the corresponding π-stacking peak shows a rather low intensity for **SM2** (π-stacking distance of 3.7 Å) or is absent in the case of **SM3**. The reduction in structural order on going from **SM1** to **SM2** and to **SM3** is in agreement with the data obtained from optical spectra (discussed in earlier sections), from which it was noted that the more π-extended SM analogues aggregated more weakly in solution (likely due to the side-chain effect).

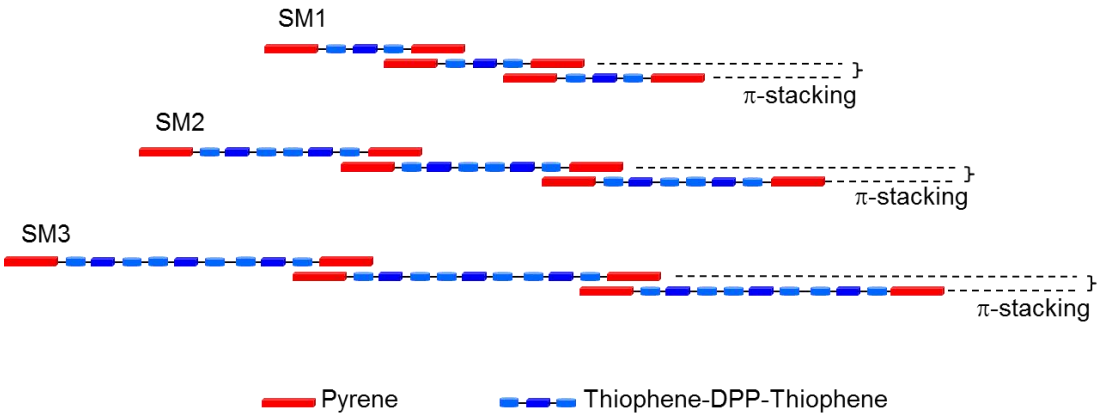

Figure 2.12. Schematic illustration of the π-stacking for **SM1-3** film deposited by SVED from $CHCl_3$ and THF.

The GIWAXS patterns of **SM1-3** shown in Figures 2.19d-f and 2.10, and obtained from THF-mediated SVED, indicate a different organizational pattern in comparison to those discussed above for $CHCl_3$-mediated SVED. In contrast to **SM1**, for which structural order

was found to decrease slightly on changing the SVED solvent from $CHCl_3$ to THF, the crystallinity of **SM2** and **SM3** improves by THF-mediated SVED processing. This is reflected in the greater number of distinct higher-order interlayer and π-stacking reflections in the corresponding patterns in Figure 2.6e,f. In both cases, the molecules are organized preferentially edge-on ($R_{in/out}$ = 0.02 for **SM2** and **SM3**), with interlayer and π-stacking distances of 19.2 Å and 3.5 Å for **SM2** and 19.2 Å and 3.5 Å for **SM3**. Although the X-ray results do not provide strong evidence about the molecular packing, it is assumed based on the structural data of **SM1** that the π-stacking interactions occur between pyrene units also for **SM2** and **SM3** (Figure 2.12). Similar to **SM1**, the angle of the wide-angle off-reflections for **SM2** also suggest a 45° tilt of the pyrene motifs with respect to the surface. For **SM3**, the molecular packing is significantly enhanced by using THF in comparison to $CHCl_3$, yielding a distinct in-plane π-stacking reflection associated to a distance of 3.5 Å. The in-plane position of this peak is characteristic for a non-tilted arrangement of the pyrenes. While a close correlation between conjugation length in **SM1-3** and thin-film crystallinity exists for films processed from $CHCl_3$–mediated SVED, those are not as prominent for films processed from THF–mediated SVED. The films obtained from THF show a distinct layer organization for all three SM analogues, with only a modest suppression of molecular packing with increasing π–conjugation length, whereas the degree of surface alignment tends to drop.

2.6 OFETs

To examine the influence of morphology and molecular organization on the carrier transport in **SM1-3**, BGTC transistors were fabricated following the same protocol as that developed for the spin-coated films. As shown in Figure 2.13 and Table 2.4, transistors based on **SM2** obtained from $CHCl_3$-mediated SVED afford unipolar transport with a hole mobility of 0.12 $cm^2\ V^{-1}\ s^{-1}$ and a threshold voltage V_T of -5 V. Meanwhile, transistors based on **SM3**

achieve ambipolar transport with a hole mobility of 0.06 cm^2 V^{-1} s^{-1} and a rather balanced electron mobility of 0.02 cm^2 V^{-1} s^{-1}. In the forward drain mode for $V_{ds} > 0$ V, the crossover point from hole- to electron-dominated current is at approximately $V_g = 40$ V (Figure 2.13b). On the other hand, the crossover point from electron- to hole-dominated current in the reverse drain mode is at around $V_g = 4$ V (Figure 2.13b).

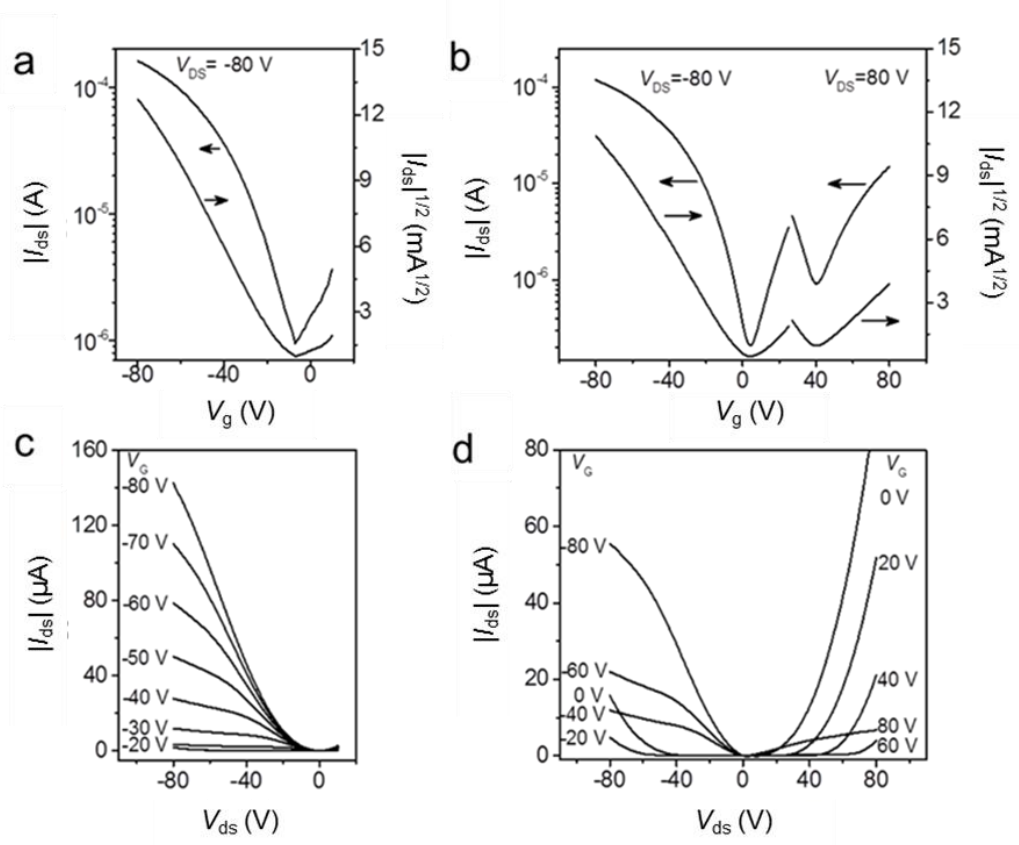

Figure 2.13. Transistor transfer and output curves of (a,c) **SM2** and (b,d) **SM3** films obtained by SVED from $CHCl_3$.

The output curve indicates contact resistance for **SM2-3**. This can be related partly to a mismatch between the HOMO of the compounds and work function of the gold electrodes. More importantly, the distinct crystalline morphologies of **SM2** and **SM3** also influence the semiconductor/electrode interface leading to different contact resistances. We assign the transition from unipolar transport in **SM2** to ambipolar transport in **SM3** to the suppressed LUMO level induced on extending the π-conjugation through successive incorporation of the DPP motifs. The decrease of the hole mobility from 0.12 cm^2 V^{-1} s^{-1} in **SM2** to 0.06 cm^2 V^{-1} s^{-}

[1] in **SM3** origins from the less of π-stacking and the reduced grain domain size in $CHCl_3$-mediated SVED-processed **SM3**.

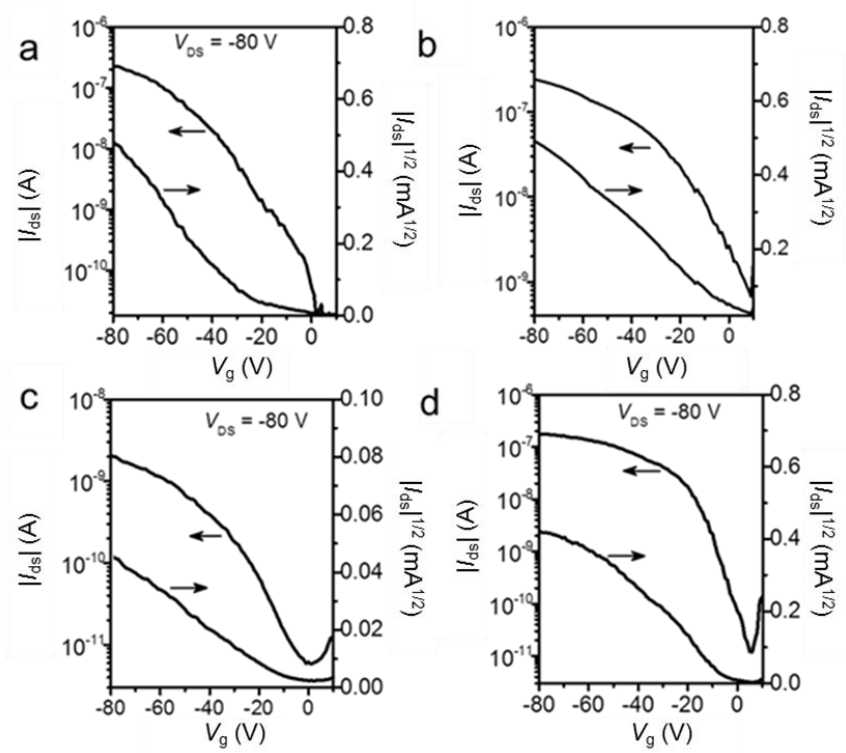

Figure 2.14. Typical transfer (V_{ds} = - 80 V) curves of **SM1-3** transistors owning gold source and drain electrodes: **SM1** obtained from a) $CHCl_3$ SVED, b) and THF SVED, as well as c) **SM2**, and d) **SM3** both obtained from THF SVED.

Table 2.4. OFET characteristics of **SM1-3** processed by $CHCl_3$-mediated and THF-mediated SVED. BGTC transistors are fabricated on S_{HMDS} after annealing 60 min at 150 °C.

Pyrene-DPPs	Electrode	SVED[#]	μ_{hole} / $\mu_{electron}$ [$cm^2 V^{-1} s^{-1}$]	V_T [V]
SM1	Au	$CHCl_3$	$(6.0 \pm 1.2) \times 10^{-4}$ / N/A	- 3
	Au	THF	$(2.1 \pm 0.8) \times 10^{-4}$ / N/A	- 3
SM2	Au	$CHCl_3$	$(1.2 \pm 0.1) \times 10^{-1}$ / N/A	- 5
	Au	THF	$(4.2 \pm 1.4) \times 10^{-4}$ / N/A	- 7
SM3	Au	$CHCl_3$	$(6.1 \pm 0.1) \times 10^{-2}$ / $(2.0 \pm 0.2) \times 10^{-2}$	4 / 40*
	Au	THF	$(3.4 \pm 0.9) \times 10^{-4}$ / N/A	-3.0
SM2	Al	$CHCl_3$	$(4.1 \pm 0.2) \times 10^{-2}$ / $(1.2 \pm 0.2) \times 10^{-2}$	-4 / 38*
SM3	Al	$CHCl_3$	$(2.0 \pm 0.1) \times 10^{-2}$ / $(2.1 \pm 0.1) \times 10^{-2}$	-27 / 22*

♯SVED,*crossover point in forward and reverse drain mode. Average value and standard deviation are calculated from 10 individual devices.

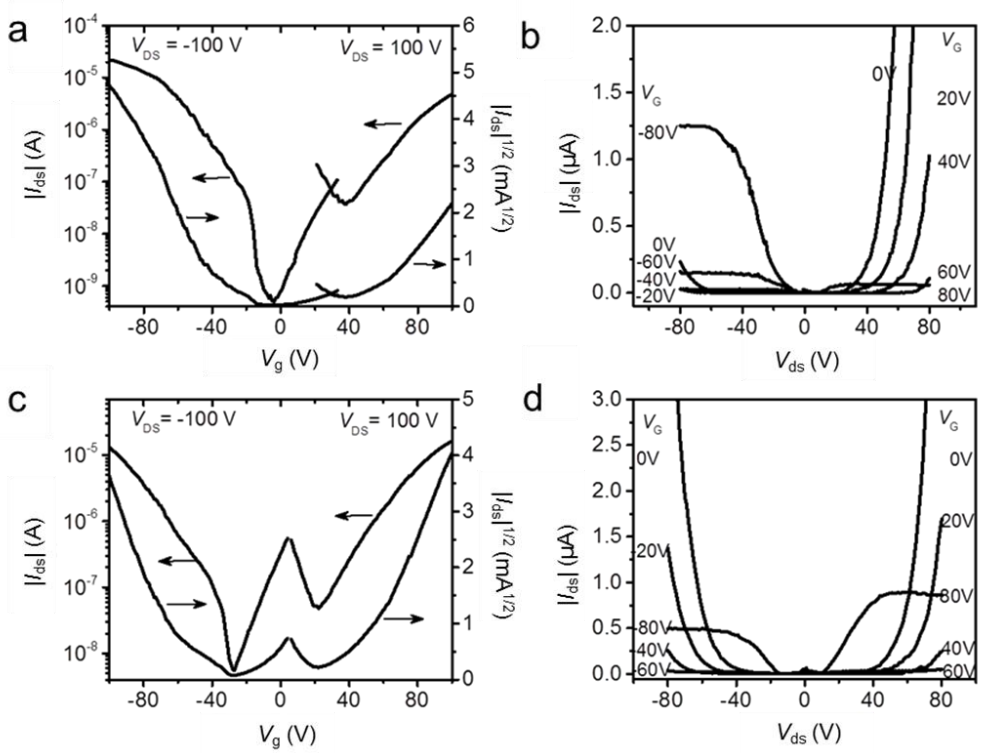

Figure 2.15. Transfer and output curves of **SM1-3** transistor owning Al source and drain electrodes: a), b) **SM2**, and c), d) **SM3** obtained from $CHCl_3$ SVED.

Surprisingly perhaps, transistors based on **SM1** and fabricated from $CHCl_3$-mediated SVED and those made with **SM1-3** and fabricated from THF-mediated SVED afforded only modest hole mobilities of less than 0.001 $cm^2\ V^{-1}\ s^{-1}$ (Figure 2.14 and Table 2.4). The random orientations of crystals and/or fibers leading to a high density of grain boundaries and the voids formed between crystals and/or fibers may be at the origin of those limitations. Therefore, **SM1** diamond-like crystals and **SM1-3** fibers obtained from THF processing tend to show higher molecular order, but lower carrier mobilities compared to $CHCl_3$-mediated SVED processed OFETs with **SM2** and **SM3**.

To lower the injection barrier for electrons in OFETs processed from $CHCl_3$-mediated SVED with **SM2**, we tentatively used aluminum source and drain electrodes. As shown in Figure 2.15 and Table 2.4, these transistors based on **SM2** achieve ambipolar behavior with a hole mobility of 0.04 $cm^2\ V^{-1}\ s^{-1}$ and an electron mobility of 0.01 $cm^2\ V^{-1}\ s^{-1}$. Here, it is worth

noting that ambipolar transport is achieved via the low work-function of aluminum (ca. 4.2 eV), promoting electron injection into the semiconductor layer in spite of the shallower LUMO of **SM2** compared to that of **SM3**. At the same time, the energy offset between the HOMO of **SM2** and the metal work-function increases, resulting in reduced hole injection and hole mobility values following this device engineering approach.

2.7 Conclusion

In summary, I have demonstrated that the extension of π-conjugation length across the set of well-defined, analogous pyrene-functionnalized DPP molecules **SM1-3** induces critical changes in their self-assembly when the molecules are subjected to SVED protocols. In particular, I found that the more extended pyrene-DPP analogues tend to form smaller crystal sizes and very distinct morphologies as a result. The self-assembly also depends on the nature of the solvent used in the SVED protocols. The formation of the one-dimensional fibers of **SM1-3** in THF is attributed to initial aggregation in solution, owing to the reduced solubility and strong π-π stacking interactions. Furthermore, swapping $CHCl_3$ for THF also improves structural order for the more π-extended molecular systems (**SM2**, **SM3**). Further incorporations of DPP motifs into the main-chain of the small molecules induces a significant narrowing of the energy gap, mainly through a suppression of the LUMO level on going from **SM1**, to **SM2** and to **SM3**. While OFETs based on **SM2** show unipolar hole transport characteristics only, OFETs made with **SM3** exhibit ambipolar field-effect behavior.

The content of this chapter has been published in: Chemistry of Material

Reprinted with permission from (Chem. Mater. 2018, 30, 15, 5032-5040)

Reference

1. Y. Zhao, Y. Guo and Y. Liu, *Adv. Mater.*, 2013, **25**(38): 5372-5391.
2. H. Dong, X. Fu, J. Liu, Z. Wang and W. Hu, *Adv. Mater.*, 2013, **25**(43): 6158-6183.
3. Y. Yuan, G. Giri, A.L. Ayzner, A.P. Zoombelt, S.C. Mannsfeld, J. Chen, D. Nordlund, M.F. Toney, J. Huang and Z. Bao, *Nat. Commun.*, 2014, **5**: 3005.
4. X. Xu, Y. Yao, B. Shan, X. Gu, D. Liu, J. Liu, J. Xu, N. Zhao, W. Hu and Q. Miao, *Adv. Mater.*, 2016, **28**(26): 5276-5283.
5. Z. Liang, Q. Tang, J. Xu and Q. Miao, *Adv. Mater.*, 2011, **23**(13): 1535-1539.
6. D. Gupta and Y. Hong, *Org. Electron.,* 2010, **11**(1): 127-136.
7. R. J. Chesterfield, J.C. McKeen, C. R. Newman, P. C. Ewbank, D. A. S. Filho, J-L. Brédas, L. L. Miller, K. R. Mann and C. D. Frisbie, *J. Phys. Chem. B*, 2004, 108, 50, 19281-19292.
8. H. Hwang, D. Khim, J.-M. Yun, E. Jung, S.-Y. Jang, Y.H. Jang, Y.-Y. Noh and D.-Y. Kim, *Adv. Funct. Mater.*, 2015, **25**(7): 1146-1156.
9. A. Tang, C. Zhan, J. Yao and E. Zhou, *Adv. Mater.*, 2017, **29**(2): 1600013.
10. G. Lin, Y. Qin, J. Zhang, Y.-S. Guan, H. Xu, W. Xu and D. Zhu, *J. Mater. Chem. C*, 2016, **4**(20): 4470-4477.
11. Y. Zhang, C. Kim, J. Lin and T.-Q. Nguyen, *Adv. Funct. Mater.*, 2012, **22**(1): 97-105.
12. Y. Suna, J. Nishida, Y. Fujisaki, and Y. Yamashita, *Org. Lett.*, 2012, **14**(13): 3356-3359.
13. S. Wang, L. Dossel, A. Mavrinskiy, P. Gao, X. Feng, W. Pisula and K. Mullen, *Small*, 2011, **7**(20): 2841-2846.
14. S. Wang, M. Kappl, I. Liebewirth, M. Muller, K. Kirchhoff, W. Pisula and K. Mullen, *Adv. Mater.*, 2012, **24**(3): 417-420.
15. K.-C. Choi, E.-J. Lee, Y.-K. Baek, M.-J. Kim, Y.-D. Kim, P.-W. Shin and Y.-K. Kim, *RSC Adv.*, 2014, **4**(14): 7160.
16. M.S. Chen, O.P. Lee, J.R. Niskala, A.T. Yiu, C.J. Tassone, K. Schmidt, P.M. Beaujuge, S.S. Onishi, M.F. Toney, A. Zettl and J.M. Frechet, *J. Am. Chem. Soc.*, 2013, **135**(51): 19229-19236.
17. O.P. Lee, A.T. Yiu, P.M. Beaujuge, C.H. Woo, T.W. Holcombe, J.E. Millstone, J.D. Douglas, M.S. Chen and J.M. Frechet, *Adv. Mater.*, 2011, **23**(45): 5359-5363.

18. X. Guo, S.R. Puniredd, M. Baumgarten, W. Pisula and K. Mullen, *Adv. Mater.*, 2013, **25**(38): 5467-5472.

Chapter 3 Crystallization control of organic semiconductors during meniscus-guided coating by blending with polymer binder

3.1 Introduction

Small molecule OSCs show advantages to form highly ordered crystalline films and some of the best carrier mobilities have reached up to 10 $cm^2 V^{-1} s^{-1}$.[1-3] However, solution processed small molecule OSCs are prone to suffer from their uncontrolled nucleation and growth limiting their functionality in electronic devices.[4] In Chapter 2, **SM1** diamond-like crystals fabricated from $CHCl_3$-mediated SVED and **SM1-3** crystalline fibers fabricated from THF-mediated SVED show higher molecular order but yielded low hole mobilities of less than 0.001 $cm^2 V^{-1} s^{-1}$. The limited mobility results from the random orientations of crystals and fibers and the voids formed between crystals and/or fibers. Alignment of the growing OSC thin film can be achieved by dip-coating due to the directional motion of substrate.[5-7] However, it is also challenging to dip-coat small molecule OSCs into large-area continuous, crystalline thin films due to the low viscosity and dewetting propensity of their solutions.[8]

Blending small molecule OSCs with insulating polymers has been demonstrated as an effective way to fabricate high performance OFETs with high reproducibility,[1, 9, 10] including OSCs such as rubrene,[11] TIPS-pentacene,[12] C8-BTBT,[1] diF-TES-ADT.[13, 14] Therefore, dip-coating of OSCs and polymer blends may mitigate the challenges associated to solution processing of small molecule OSCs since the polymer binder is expected to improve the film-forming ability. Especially, the understanding of the correlation between the coating conditions and the resulted morphology in terms of the crystallization mechanism of small molecule OSCs in the blend is still incomplete.

This chapter describes that a small fraction of amorphous PMMA efficiently improves the crystallization of dip-coated small OSCs, DH4T and diketopyrrolopyrrole-sexithiophene

(DPP6T). The maximum charge carrier mobilities of dip-coated OSC:PMMA films are significantly higher than drop-cast blend and comparable with OSC single crystals. The high charge carrier mobility originates from a continuous alignment of the crystalline films and stratified OSC and PMMA layers. The improved crystallization is attributed to the elevated mass transport induced by viscosity gradient.

3.2 Dip-coating of DH4T:PMMA blend

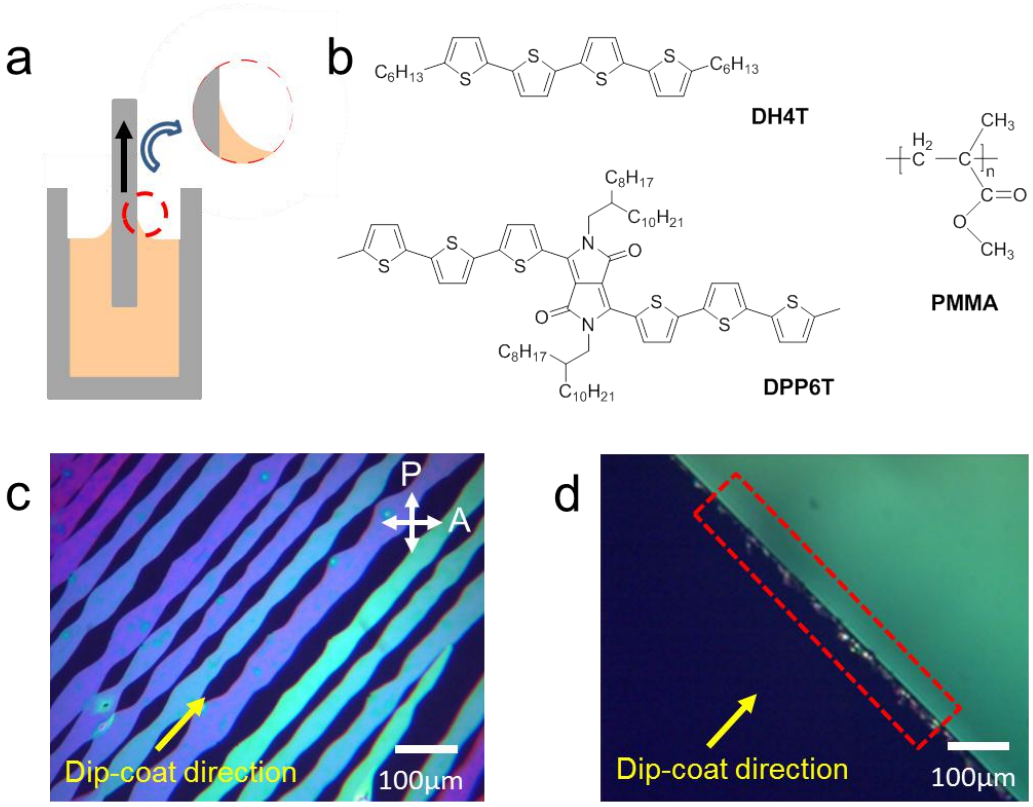

Figure 3.1. (a) Schematic illustration of the dip-coating process (inset: magnification of meniscus). (b) Molecular structures of DH4T, DPP6T and PMMA. Polarized optical microscopy images of (c) dip-coated DH4T:PMMA$_{(100\ kDa,\ 10\%)}$ and (d) dip-coated DH4T.

Meniscus-guided coating is an efficient approach for deposition of OSCs films.[15, 16] The schematic in Figure 3.1a illustrates the dip-coating process involving a concave solution meniscus during the vertical withdrawal of a substrate from solution. The molecular structures of DH4T, DPP6T, and insulator polymer PMMA are presented in Figure 3.1b. Three different

MWs of PMMA, 2 kDa, 100 kDa, and 2480 kDa were studied. The DH4T:PMMA$_{(100\ kDa,\ 10\%)}$ blend was dip-coated from a 3 mg/mL $CHCl_3$ solution at a speed of 5 μm/s on a Si/SiO_2 substrate treated by oxygen plasma (S_{plasma}). Here $CHCl_3$ was selected as the solvent because of its good solubility of small molecule OSCs and relatively low boiling point of 61.2°C with high partial pressure.[17] The oxygen plasma treatment leads to high substrate surface energy and thus wettable property, assisting the film formation during solution processing.[18] Polarized optical microscopy images in Figure 3.1c display aligned crystalline ribbons of the DH4T:PMMA$_{(100\ kDa,\ 10\%)}$ film. These structures are highly birefringent and optically anisotropic indicating high order and long-range macroscopic orientation of DH4T molecules. In contrast, when dip-coating pristine DH4T only few aggregates were formed at the edge of the S_{plasma} but no nucleation on the substrate surface occurred, as shown in Figure 3.1d.

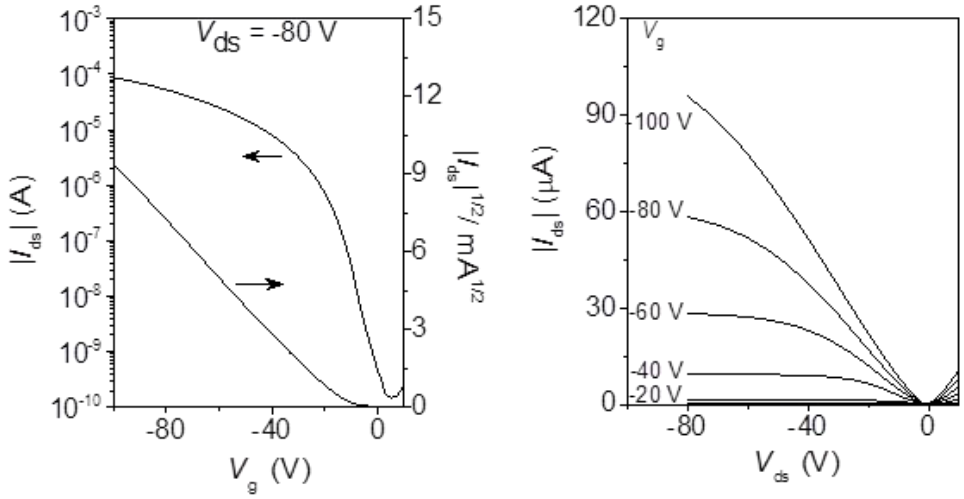

Figure 3.2. Transfer and output characteristics of dip-coated DH4T:PMMA$_{(100\ kDa,\ 10\%)}$ film.

BGTC transistors based on the dip-coated DH4T:PMMA$_{(100\ kDa,\ 10\%)}$ film were fabricated with the channel parallel to the alignment of the crystalline ribbons. Typical transfer and output curves are shown in Figure 3.2. A hole mobility of 0.05 $cm^2\ V^{-1}\ s^{-1}$ is obtained with an on/off ratio of around 10^6 and a threshold voltage of -17 V.

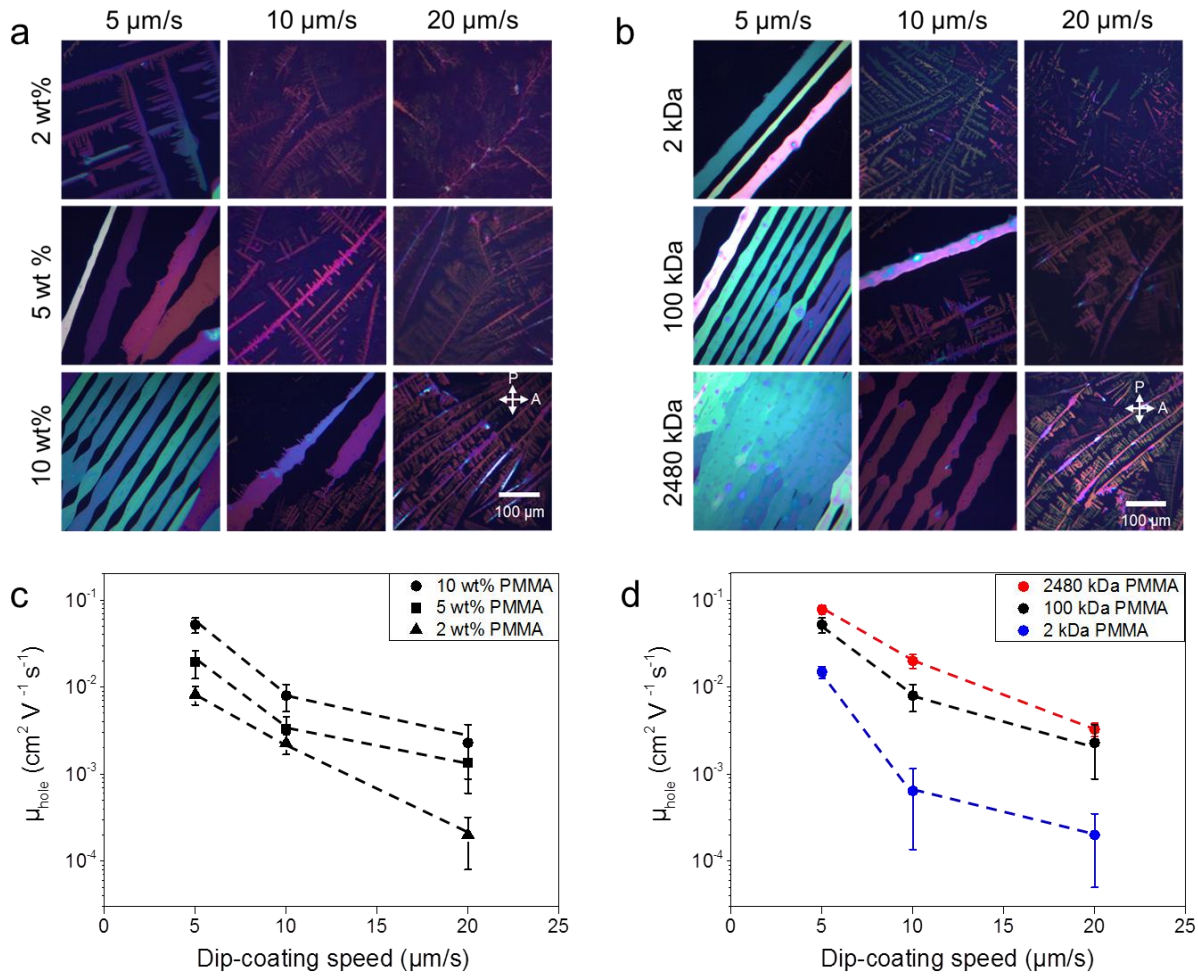

Figure 3.3. Polarized optical microscopy images and hole charge carrier mobility of dip-coated DH4T:PMMA films for various (a,c) weight fractions of PMMA (at 100 kDa) and (b,d) MWs of PMMA (at 10 wt%).

To understand the effect of PMMA on the crystallization kinetics of DH4T during dip-coating, systematic studies were performed with the focus on the role of wt% and MW of PMMA. As shown in Figures 3.3a and 3.4, Polarized optical microscopy and atomic force microscopy images exhibit the morphology of DH4T:PMMA$_{(100\ kDa)}$ for the dip-coating speeds of 5 µm/s, 10 µm/s and 20 µm/s and different wt% of PMMA from 2 wt%, to 5 wt% and 10 wt%. During dip-coating, solvent evaporation and substrate withdraw lead to solute supersaturation at the meniscus, inducing nucleation and crystal growth at the contact line.[16] By decreasing the dip-coating speed of the DH4T:PMMA blend, dendritic crystals gradually change into long-range aligned crystalline ribbons and the film thickness increases continuously from 20 nm to 250 nm. The dendritic crystals originate from mismatch the

crystal growth. Interestingly, blending of PMMA can enhance the mass transport and improve the crystal growth of DH4T. In this way, the formation of dendritic crystals is inhibited and crystalline ribbons with high coverage are grown.

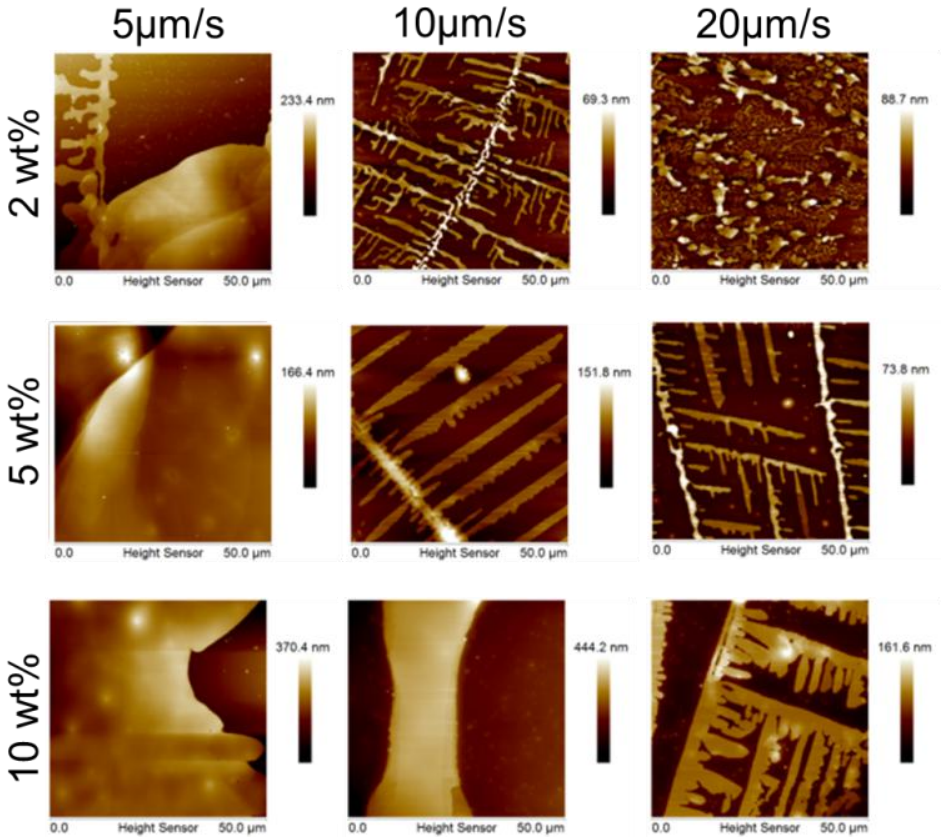

Figure 3.4. Atomic force microscopy images of dip-coated DH4T:PMMA films by varying the dip-coating speed and the weight fraction (wt%) of $PMMA_{(100\ kDa)}$.

The MW of PMMA was varied from 2 kDa to 100 kDa and 2480 kDa for DH4T:$PMMA_{(10\%)}$ to understand the effect of MW of PMMA on the growth of DH4T. Low-MW $PMMA_{(2\ kDa)}$ leads to dendritic crystals at a high dip-coating speed of 20 μm/s and to crystalline ribbons with a low coverage at 5 μm/s (Figure 3.3b). The high-MW $PMMA_{(2480\ kDa)}$ favors the alignment of the dendritic crystals at 20 μm/s and significantly enhances the coverage density of crystalline ribbons at 5 μm/s. The morphology characterization proves that blending of a small wt% of the polymer binder can efficiently improve the crystallization of small molecule OSCs during dip-coating.

However, this does not mean that higher wt% or Mw of PMMA can continue improve the morphology of dip-coated DH4T:PMMA. For instance, the dip-coated DH4T:PMMA$_{(2480\ kDa,\ 50\%)}$ films obtained at 5 µm/s exhibit stick-slip-morphology (Figure 3.5).[19] Therefore, the high quality crystalline morphology requires an appropriate wt% of PMMA and coating parameters.

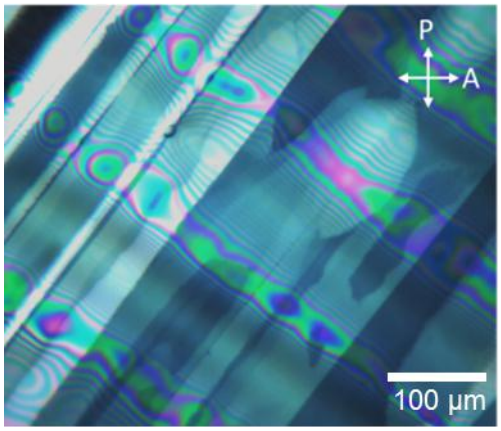

Figure 3.5. Polarized optical microcopy image of the stick-slip morphology of dip-coated DH4T:PMMA(2480 kDa, 50%) obtained at 5 µm/s.

BGTC transistors based on dip-coated DH4T:PMMA films were fabricated, in which the crystalline ribbons were aligned along the channel. As shown in Figure 3.3c, the mobilities of dip-coated DH4T:PMMA$_{(100\ kDa)}$ films increase with the decrease of the dip-coating speed. For the same dip-coating speed, high-wt% PMMA leads to a higher charge carrier mobility (Figure 3.3c). In the case of 5 µm/s, DH4T blending with 10 wt% PMMA$_{(100\ kDa)}$ exhibits an average mobility of 0.05 $cm^2\ V^{-1}\ s^{-1}$ which is 2 and 6 times higher than that with 5 wt% and 2 wt% PMMA, respectively. Concerning the MW of PMMA, high-MW PMMA results in more homogeneous morphologies and thereby higher charge carrier mobilities (Figure 3.3d). A maximum mobility of 0.1 $cm^2\ V^{-1}\ s^{-1}$ is obtained for the dip-coated DH4T:PMMA$_{(2480\ kDa,\ 10\%)}$ film at 5 µm/s which is on par with the highest values for DH4T single crystals and vacuum sublimated films.[20] However, the device performance of dip-coated DH4T:PMMA films depends on their crystalline morphology. A high void area and low degree of alignment lead to a low charge carrier mobility.

3.3 Spin-coating and drop-casting of DH4T:PMMA blend

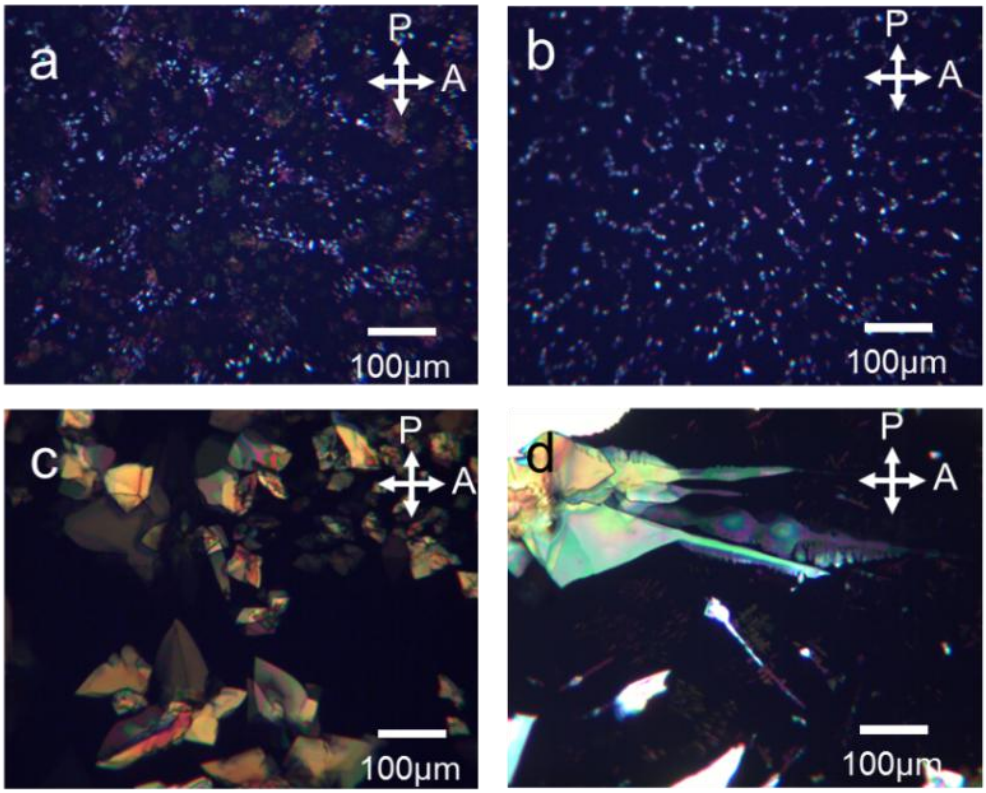

Figure 3.6. Polarized optical microscopy images of spin-coated (a) DH4T and (b) DH4T:PMMA$_{(2480\ kDa,\ 10\%)}$, drop-cast (c) DH4T and (d) DH4T:PMMA $_{(2480\ kDa,\ 10\%)}$.

For spin-coated and drop-cast film, the influence of a small fraction of PMMA on the DH4T crystallization is minor. Discontinuous aggregates are formed after spin-coating both pristine DH4T and DH4T:PMMA$_{(2480\ kDa,\ 10\%)}$, as shown in Figure 3.6. After drop-casting, pristine DH4T grows into randomly distributed crystal flakes, while the drop-cast DH4T:PMMA$_{(2480\ kDa,\ 10\%)}$ film reveals mainly flake-like crystals and few dendritic one (Figure 3.6). These results indicate that PMMA weakly influences the crystallization of DH4T during spin-coating and drop-casting. The charge carrier mobilities for drop-cast pristine DH4T and DH4T:PMMA$_{(2480\ kDa,\ 10\%)}$ films are 0.015 $cm^2\ V^{-1}\ s^{-1}$ and 0.013 $cm^2\ V^{-1}\ s^{-1}$, respectively (Figure 3.7).

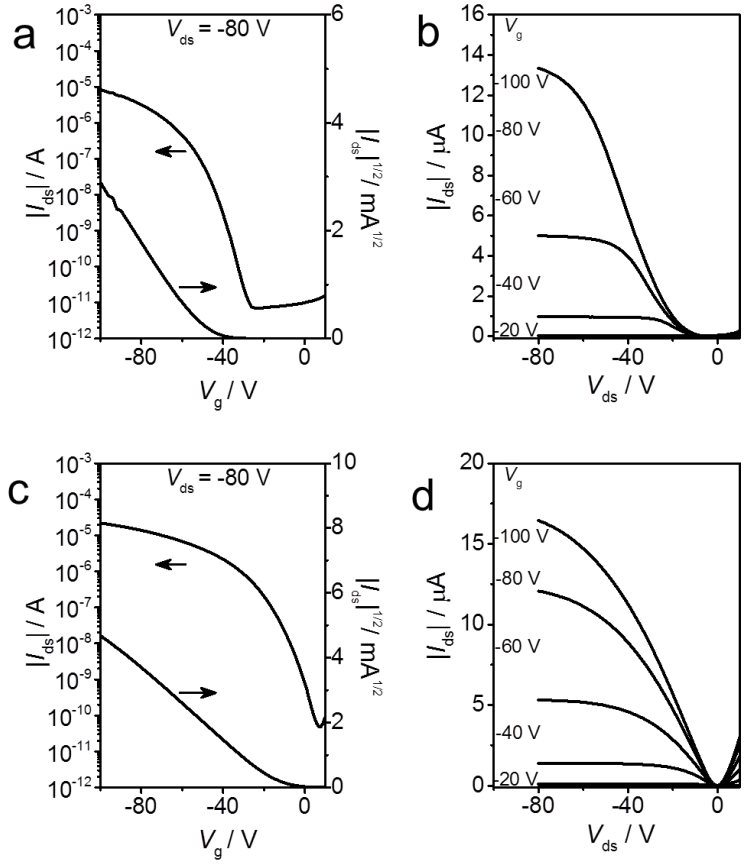

Figure 3.7. Transfer and output curves of drop-cast (a, b) DH4T and (c, d) DH4T:PMMA$_{(2480\ kDa,\ 10\%)}$.

3.4 Role of polymer binder on OSC crystallization

3.4.1 Meniscus angle and viscosity

To understand the origin of the improved crystallization induced by blending PMMA during dip-coating of DH4T, the meniscus angle and solution viscosity were studied. As shown in Figure 3.8, the meniscus angle for the dilute PMMA/$CHCL_3$ solution (less than 3 mg/mL) is around 32-34°, which is independent on wt% and MW of PMMA, and corresponds to the meniscus angle of $CHCl_3$. In addition, the meniscus angle of the PMMA/$CHCL_3$ (3 mg/mL) solution keeps stable during the drawdown of liquid level, indicating a stable meniscus angle during dip-coating. The stable meniscus angle results from the low surface tension of $CHCl_3$ (26.7 mN/m).[21] This proves that a small fraction of PMMA does not influence the dip-coating meniscus angle of the $CHCl_3$ solution.

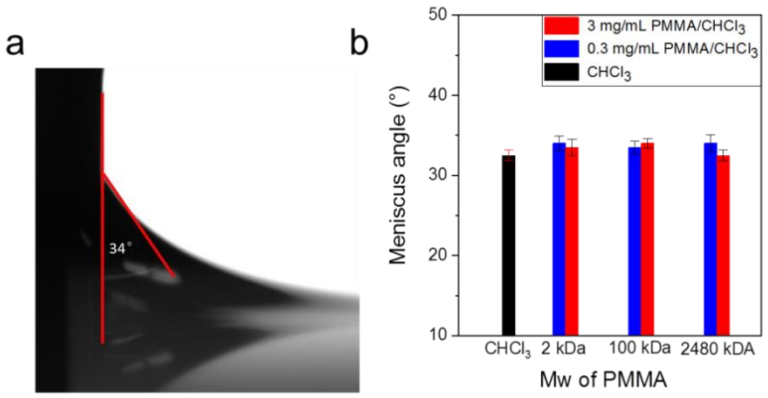

Figure 3.8. (a) Photographs of the meniscus angle of the S_{plasma} immersed in 0.3 mg/ $PMMA_{(2480\ kDa)}/CHCl_3$. (b) Meniscus angle of $PMMA/CHCl_3$ solution during dip-coating.

The dynamic viscosity of a solution containing small conjugated molecules mainly depends on the solvent viscosity in contrast to a polymer solution.[22] In our case, we assumed that only PMMA influence the viscosity of solution, since PMMA chains entangle at the increased concentration and result in stronger interchain forces leading to a high viscosity.[23] Thereby, the viscosity of the $DH4T/CHCl_3$ solution is a constant and identical to that of $CHCl_3$ (η_0 = 0.61 cP), while the viscosity of the $DH4T:PMMA/CHCl_3$ solution is attributed to the wt% and MW of PMMA. The dynamic viscosity of dilute $PMMA/CHCl_3$ solution was measured by an Ostwald capillary viscometer, fitted according to the Huggins equation[24]

$$\eta = f(c_{PMMA}) = \eta_0 \left(1 - \frac{0.05 * c_{PMMA}}{0.00005 + c_{PMMA}}\right)(1 + 560 * c_{PMMA} + 39733 * (c_{PMMA})^2)$$

(Equation 3.1)

wherein, η_0=0.61 cP, c_{PMMA}=0.3 mg/mL.

As shown in Figure 3.9a, the viscosity of the dilute $PMMA/CHCl_3$ solution increases with wt% and MW of PMMA. At a concentration of c_{PMMA} = 0.3 mg/mL (corresponding to the 10 wt% PMMA in 3 mg/mL $DH4T:PMMA/CHCl_3$), the viscosity of the bulk solution (η_{bulk}) of $PMMA_{(2480\ kDa)}/CHCl_3$ is around 0.68 cP, only slightly higher than η_0 (Table 3.1).

However, the viscosity at the meniscus during dip-coating is expected to be higher due to the increased solution concentration caused by solvent evaporation.

Table 3.1. The dynamic viscosity of PMMA/$CHCl_3$ solution.

Concentration	Dynamic viscosity [cP]			
	$CHCl_3$	$PMMA_{(2\ kDa)}$	$PMMA_{(100\ kDa)}$	$PMMA_{(2480\ kDa)}$
0.06 mg/mL	0.61	0.61	0.61	0.61
0.12 mg/mL		0.61	0.61	0.63
0.3 mg/mL		0.61	0.62	0.68
3.0 mg/mL		0.62	0.65	1.75

The viscosity of defined DH4T/$CHCl_3$ and defined DH4T:$PMMA_{(2480\ kDa,\ 10\%)}$/$CHCl_3$ at the meniscus is estimated by COMSOL. As shown in Figure 3.9b, a viscosity gradient of defined DH4T:$PMMA_{(2480\ kDa,\ 10\%)}$/$CHCl_3$ is formed at the meniscus due to blending of PMMA in contrast to the constant viscosity of defined DH4T/$CHCl_3$. The calculated result exhibits an obvious viscosity-gradient at the meniscus, and an even higher viscosity is expected at the solution-substrate contact line in reality. As a consequence, the thickness of dip-coated $PMMA_{(2480\ kDa)}$ is higher than those for $PMMA_{(100\ kDa)}$ and $PMMA_{(2\ kDa)}$, as shown in Figure 3.9c. It demonstrates that viscosity-gradient at the meniscus contributes to the increased mass transport for the film deposition. Therefore, the viscosity-gradient at the meniscus plays a crucial role on improving the crystallization of DH4T.

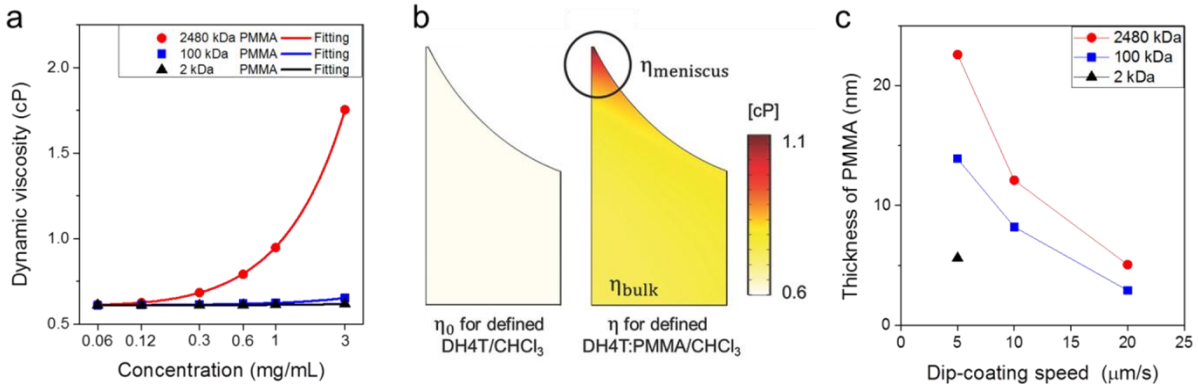

Figure 3.9. (a) Dynamic viscosity of dilute PMMA/$CHCl_3$ bulk solution. (b) Calculated dynamic viscosity at the meniscus of defined DH4T/$CHCl_3$ solution (η_0 = 0.61 cP) and defined DH4T:PMMA/$CHCl_3$ solution (η_{bulk} = 0.68 cP). (c) Average thicknesses of dip-coated PMMA from 0.3mg/mL $CHCl_3$ obtained at different coating speed.

3.4.2 Phase separation

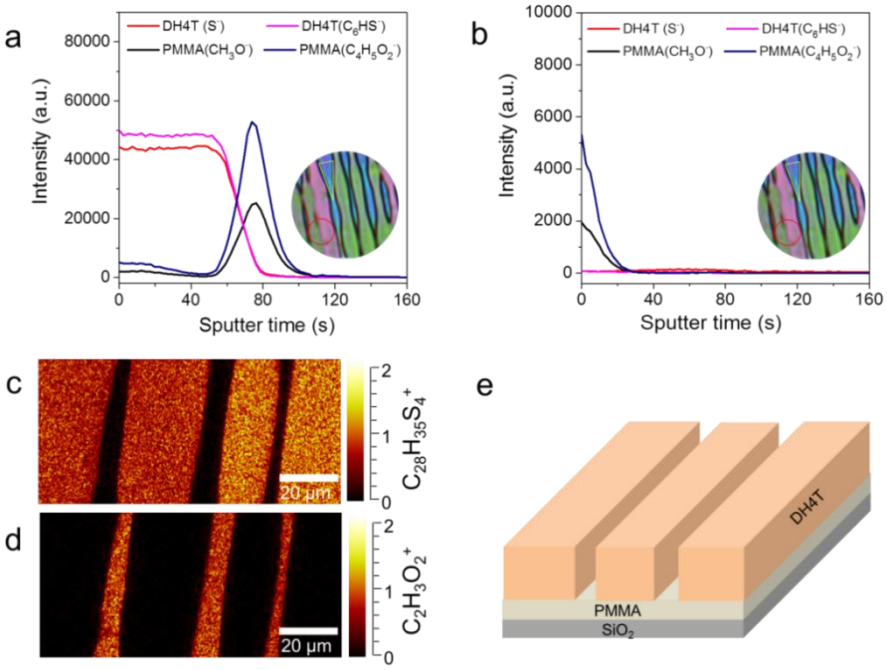

Figure 3.10. ToF-SIMS depth profiles of dip-coated DH4T:PMMA$_{(2480\ kDa,\ 10\%)}$ films reconstructed from the areas indicated by (a) red circle shapes and (b) yellow triangle. (c) and (d) lateral distributions of characteristic secondary ion signals on the top surface of dip-coated DH4T:PMMA films obtained by ToF-SIMS imaging analysis. (e) Schematic cross-section diagram of the DH4T and PMMA distribution in the dip-coated films.

To reveal the phase separation and distribution of the two components in the dip-coated DH4T:PMMA film, time-of-flight secondary ion mass spectrometry (ToF-SIMS) were performed (carried out by Lothar Veith). Depth profiles in the negative secondary ion polarity of the DH4T:PMMA$_{(2480\ kDa,\ 10\%)}$ film were acquired in the ToF-SIMS dual-beam depth profiling mode (Figure 3.10a,b). For the crystalline area (Figure 3.10a, highlighted circle in the inset optical image), the depth profile shows in the sputter time from 0 s to 60 s a constant high intensity of DH4T-specific ions (S^-, C_6HS^-) and low intensity of PMMA- specific ones (CH_3O^-, $C_4H_5O_2^-$). After this sputter time, the DH4T signals decrease, while the PMMA signals increase. This indicates a vertical phase separation in the dip-coated DH4T:PMMA film with a top DH4T layer and bottom PMMA layer. In the non-crystalline area (highlighted triangle in the inset optical image of Figure 3.10b), PMMA (CH_3O^-, $C_4H_5O_2^-$) signals decrease from the beginning within the first 20 s indicating a thin PMMA layer, while no

DH4T (S^-, C_6HS^-) were detected (Figure 3.10b). The lateral signal distribution of compound-specific positive ions on the film top surface exposes the complementary distribution of DH4T ($C_{28}H_{35}S_4^+$, Figure 3.10c) and PMMA ($C_2H_3O_2^+$, Figure 3.10d).

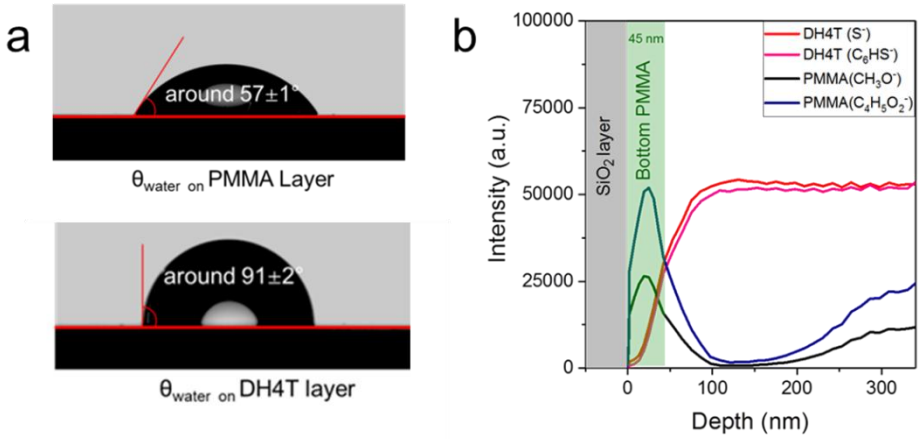

Figure 3.11. (a) Contact angle of water on PMMA layer and DH4T layer. PMMA layer is obtained by spin-coating and DH4T layer is obtained by dip-coating with PMMA (DH4T appears at the top surface). (b) ToF-SIMS depth profiles of dip-coated DH4T:PMMA$_{(2480\ kDa,\ 10\%)}$ as a function of depth.

The vertical distribution between DH4T and PMMA is induced by the difference of surface energy.[25] As shown in Figure 3.11, the contact angle of water on PMMA layer (57±1°) is lower than that on DH4T layer (91±2°), indicating that the surface energy of DH4T is lower than PMMA. Therefore, DH4T is preferentially enriched at the top free surface to reduce the overall energy.[26] The average thickness of bottom PMMA layer for DH4T:PMMA$_{(2480\ kDa,\ 10\%)}$ is around 45 nm (Figure 3.11b).

3.4.3 Crystallization process

The schematic illustrations of the dip-coating process for PMMA, DH4T, and DH4T:PMMA (optimized wt% and MW of PMMA) are shown in Figure 3.12. In the evaporation regime, solvent evaporation leads to the film growth at the solution-substrate contact line.[16] Dip-coating of PMMA from $CHCl_3$ yields a continuous film (Figure 3.12a). Since the concentration of PMMA in the meniscus increases with solvent evaporation, a

higher viscosity occurs at the dip-coating meniscus. The entanglement of polymer coils results in strong interchain forces, contributing to the film formation.[23] In contrast, pure DH4T poorly nucleates since the insufficient mass transport of solute inhibits the nucleation of DH4T crystals (Figures 3.12b and 3.1d). As for dip-coating of DH4T:PMMA, a viscosity gradient at the meniscus is established due to the blending of PMMA (Figure 3.12c). The increased viscosity draws more DH4T from solution to the solution-substrate contact line. Further solvent evaporation results in supersaturation at the meniscus near the contact line. The entangled PMMA chains are more prone to solidify on the substrate surface than DH4T. As consequence, PMMA firstly solidifies at the contact line and forms a continuous layer on the substrate. The solidified bottom PMMA layer provides an appropriate nucleation barrier for nucleation and thus induces large-scale growth of DH4T by suppressing random creation of spontaneous nucleation.[27] The MW of PMMA plays also an important role on the DH4T crystallization. High-MW PMMA shows higher interchain forces stronger supporting the formation of aligned DH4T crystal ribbons, while low-MW PMMA leads only to dendritic crystals of DH4T.

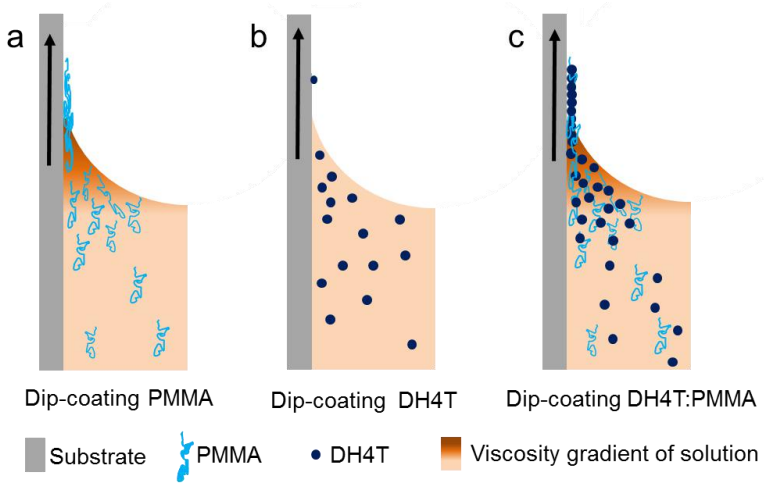

Figure 3.12. Schematic illustration for the dip-coating of (a) PMMA, (b) DH4T, and (c) DH4T:PMMA (with optimized wt% and MW of PMMA).

3.4.4 Molecular organization

To understand the effect of the polymer binder on the DH4T molecular organization, the dip-coated DH4T:PMMA$_{(2480\ kDa,\ 10\%)}$ film was further examined via GIWAXS and

selected area electron diffraction (measured by Katrin Kirchhoff). The corresponding GIWAXS and selected area electron diffraction patterns are shown in Figure 3.13 and the unit cell parameters are listed in Table 3.2. For drop-cast pristine DH4T film, the GIWAXS pattern exhibits a notably high number of reflections, implying a pronounced crystallinity (Figure 3.13a). The main meridional reflection at q_z = 0.22 Å^{-1} for q_{xy} = 0 Å^{-1} is assigned to an interlayer distance of 2.84 nm. The wide-angle equatorial scattering intensity at q_z = 0 Å^{-1} for q_{xy} = 1.61 Å^{-1} is related to a π-stacking distance of 0.39 nm. The reflections for the drop-cast DH4T:PMMA$_{(2480\ kDa,\ 10\%)}$ film are located on identical positions, but are smeared over the azimuthal direction of the pattern (Figure 3.13b) characteristic for randomly oriented crystals on the surface. In contrast, the dip-coated DH4T:PMMA$_{(2480\ kDa,\ 10\%)}$ film shows a sufficient scattering intensity indicating still a high crystallinity of oriented DH4T (Figure 3.13c).

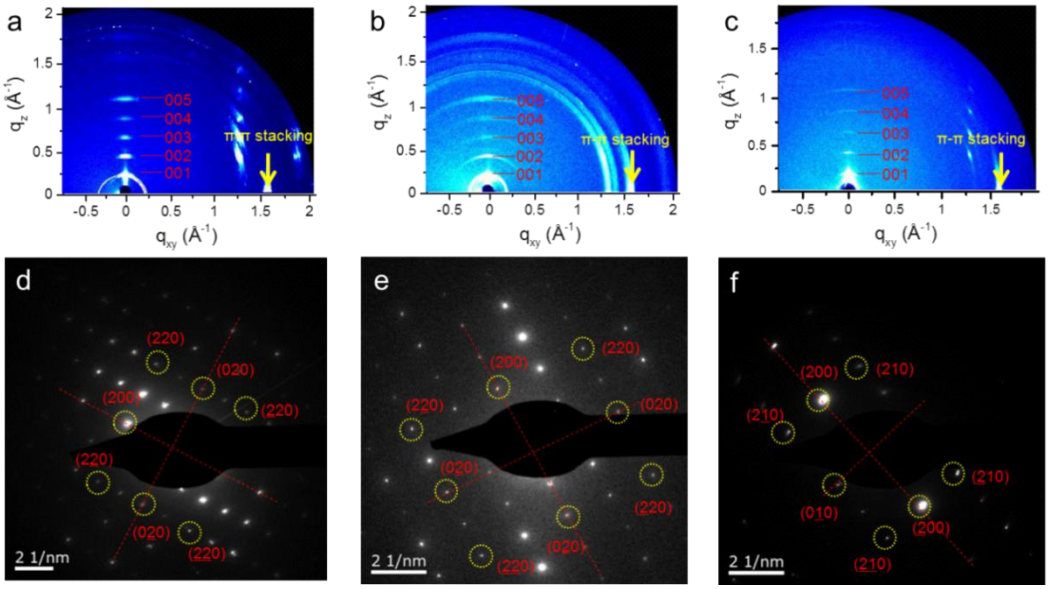

Figure 3.13. GIWAXS and selected area electron diffraction patterns of (a,d) drop-cast DH4T, (b,e) drop-cast and (c,f) dip-coated DH4T:PMMA$_{(2480\ kDa,\ 10\%)}$. Miller indices are used to assign the reflections.

The interlayer distance and π-stacking distance of dip-coated DH4T:PMMA film are 2.85 nm and 0.39 nm, respectively, verifying an identical molecular organization as found for drop-cast DH4T (schematic illustration in Figure 3.14). Figure 3.13d-f presents the highlighted diffraction peaks in the selected area electron diffraction patterns for indexing the

unit cell. Based on the GIWAXS and [001] zone electron diffraction patterns, a *monoclinic* unit cell of a_0=5.93 Å, b_0=7.88 Å, and c_0=28.42 Å for drop-cast DH4T is derived. These parameters are identical to the reported DH4T unit cell of thermally evaporated films.[28] The structural analysis revealed nearly unchanged monoclinic parameters for the drop-cast DH4T:PMMA film with a_1=5.88 Å, b_1=7.70 Å, c_1=28.24, and for dip-coated DH4T:PMMA with a_2=5.81 Å, b_2=7.70 Å, c_2=28.53. This indicates that no polymorph of DH4T is formed in the dip-coated DH4T:PMMA film, different with the case of TIPS-pentacene blended with P3HT during slow solution crystallization.[29] Therefore it can be concluded that amorphous PMMA efficiently assists the crystallization of dip-coated small molecule OSCs with high crystallinity without influencing the unit cell parameters.

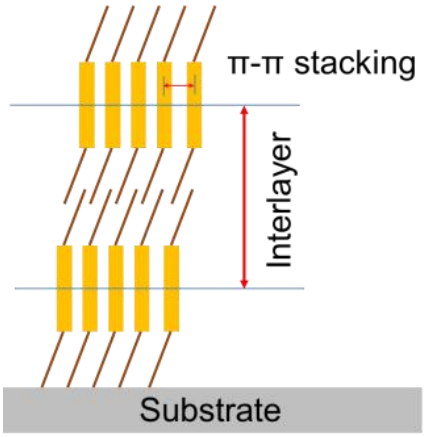

Figure 3.14. Illustration for the molecule packing of DH4T on the substrate in the dip-coated DH4T:PMMA$_{(2480\ kDa,\ 10\%)}$ film.

Table 3.2. Unit cell parameters of DH4T in films based on drop-cast DH4T, drop-cast and dip-coated DH4T:PMMA$_{(2480\ kDa,\ 10\%)}$.

Parameter	Drop-cast DH4T	Drop-cast DH4T:PMMA$_{(2480\ kDa,\ 10\%)}$	Dip-coated DH4T:PMMA$_{(2480\ kDa,\ 10\%)}$
a/A°	5.93	5.88	5.81
b/A°	7.78	7.70	7.70
c/A°	28.42	28.24	28.53

3.5 Dip-coating of DPP6T:PMMA blend

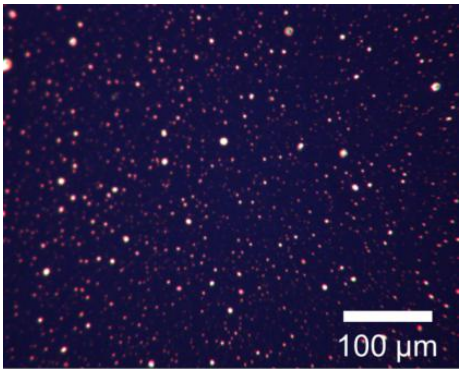

Figure 3.15. Polarized optical microscopy image of a dip-coated DPP6T obtained at 5 µm/s (3 mg/mL in $CHCl_3$).

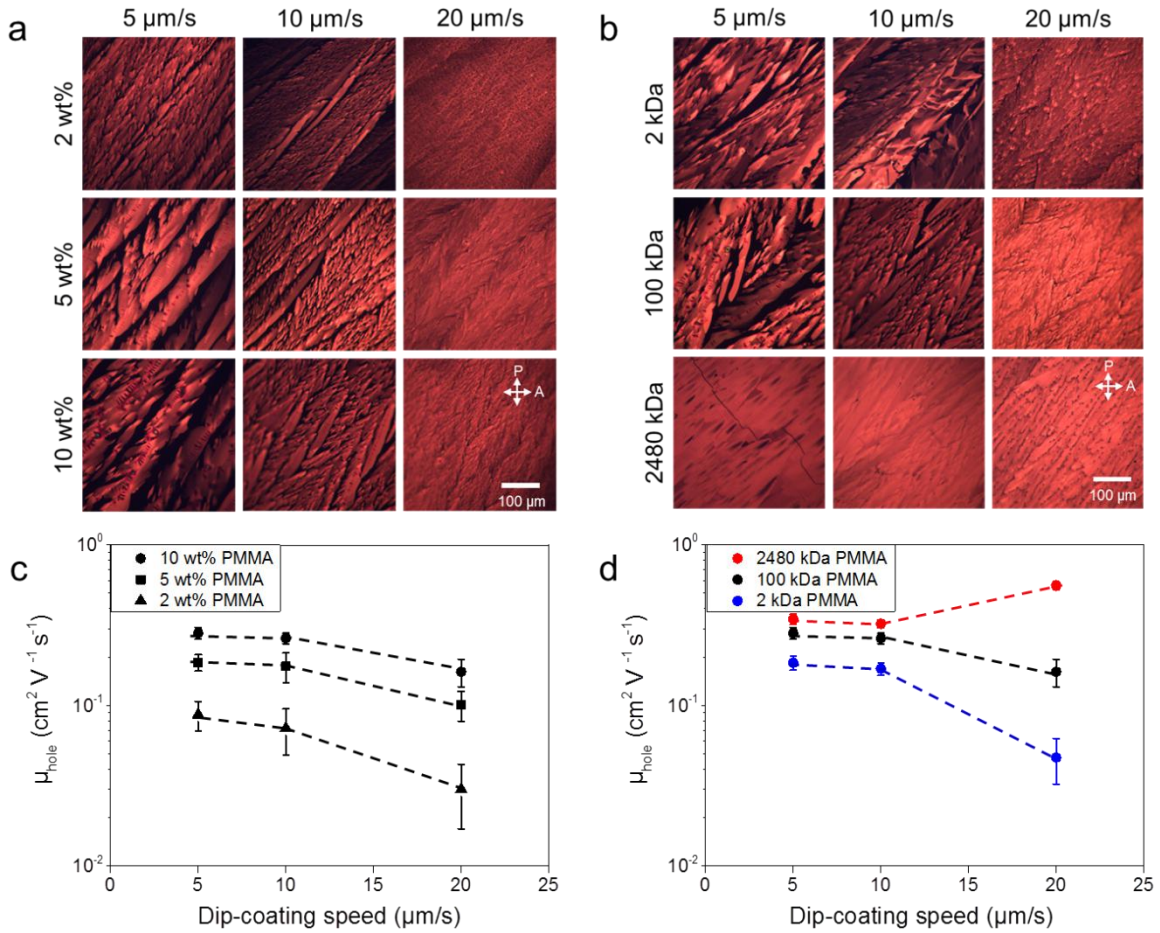

Figure 3.16. Polarized optical microscopy images and hole charge carrier mobility of dip-coated DPP6T:PMMA films for varying (a,c) the weight fraction of PMMA (100 kDa) and (b,d) MW of PMMA (10 wt%).

To prove the general character of the polymer binder on the crystallization of small molecule OSCs during dip-coating, DPP6T was additionally chosen as model compound

since its transistor performance suffers from the uncontrolled crystal growth during drop-casting. For pristine DPP6T, only discontinuous small crystals were obtained by dip-coating at 3 mg/mL from $CHCl_3$ due to the poor film-formation ability (Figure 3.15). Varying dip-coating speed did not improve the film morphology. For dip-coating DPP6T:PMMA, the fraction (2 wt%, 5 wt%, and 10 wt%) and MW (2 kDa, 100 kDa, and 2480 kDa) of PMMA were varied (Figure 3.16). As shown in Figure 3.16a, blending 100 kDa PMMA induces an alignment of the DPP6T crystals, while a higher wt% of PMMA and slower dip-coating speed lead to larger crystal domains. The increase in MW of PMMA improves the film homogeneity (Figure 3.16b). However, few cracks and wrinkles appear in the high-MW blend when the dip-coating speed decreases to 10 µm/s and 5 µm/s due to stress induced during film drying (Figures 3.16b and 3.17).[30]

The charge carrier mobility of dip-coated DPP6T:PMMA films with crystals aligned along transistor channel is summarized in Figure 3.16c,d. The mobility of the DPP6T:PMMA films increases with wt% and MW of PMMA (Figure 3.16), owing to its homogenous morphology, which is in agreement with the trend observed for the dip-coated DH4T:PMMA blend. In contrast to the DH4T:PMMA blend, the highest mobility of 0.55 $cm^2\ V^{-1}\ s^{-1}$ of the $DPP6T:PMMA_{(2480\ kDa,\ 10\%)}$ blend is found for the highest dip-coating speed of 20 µm/s. This suggests that the dip-coating speed need to be carefully optimized for each special small molecule OSC due to their different self-assembly ability.

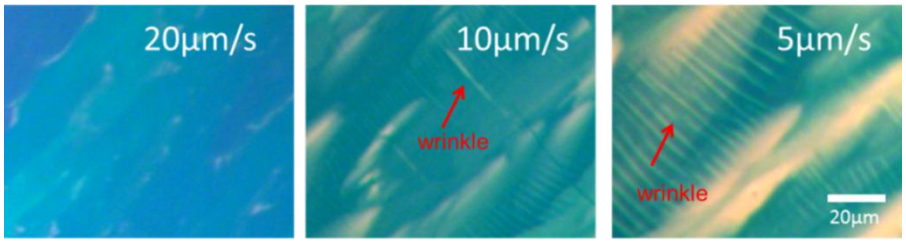

Figure 3.17. Optical microscpoy images of the morphology of dip-coated $DPP6T:PMMA_{(2480\ kDa,\ 10\%)}$ films with wrinkles obtained at different speeds.

For spin-coated DPP6T and $DPP6T:PMMA_{(2480\ kDa,\ 10\%)}$, mobilities of around 0.05 $cm^2\ V^{-1}\ s^{-1}$ and 0.02 $cm^2\ V^{-1}\ s^{-1}$, respectively, were determined. These low values arise from the

low film crystallinity (Figures 3.18a,b and 3.19a,c). The low mobility of 0.005 $cm^2\ V^{-1}\ s^{-1}$ of drop-cast DPP6T films is caused by the rough interface between semiconductor and dielectric (Figure 3.18c,d and 3.19e,g).[31] Drop-cast DPP6T:$PMMA_{(2480\ kDa,\ 10\%)}$ exhibits spherulite crystals and leads to a mobility of 0.2 $cm^2\ V^{-1}\ s^{-1}$ which is lower than that of dip-coated DPP6T:$PMMA_{(2480\ kDa,\ 10\%)}$ since grain boundaries between spherulite crystals of the drop-cast DPP6T:PMMA film inhibit the charge transport. These results prove that a small fraction of the polymer binder also significantly improve the crystallization and charge carrier transport in dip-coated DPP6T:PMMA films.

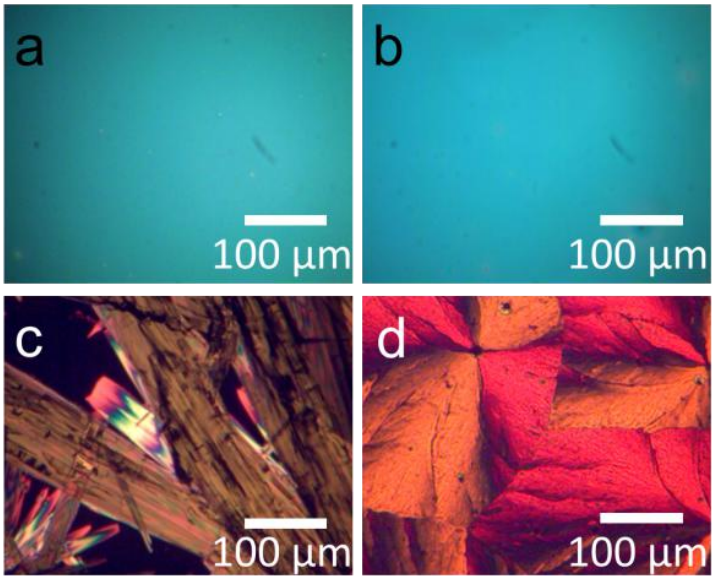

Figure 3.18. Optical microscopy images of spin-coated (a) DPP6T and (b) DPP6T:$PMMA_{(2480\ kDa,\ 10\%)}$, Polarized optical microscopy image of drop-cast (c) DPP6T and (d) DPP6T:$PMMA_{(2480\ kDa,\ 10\%)}$.

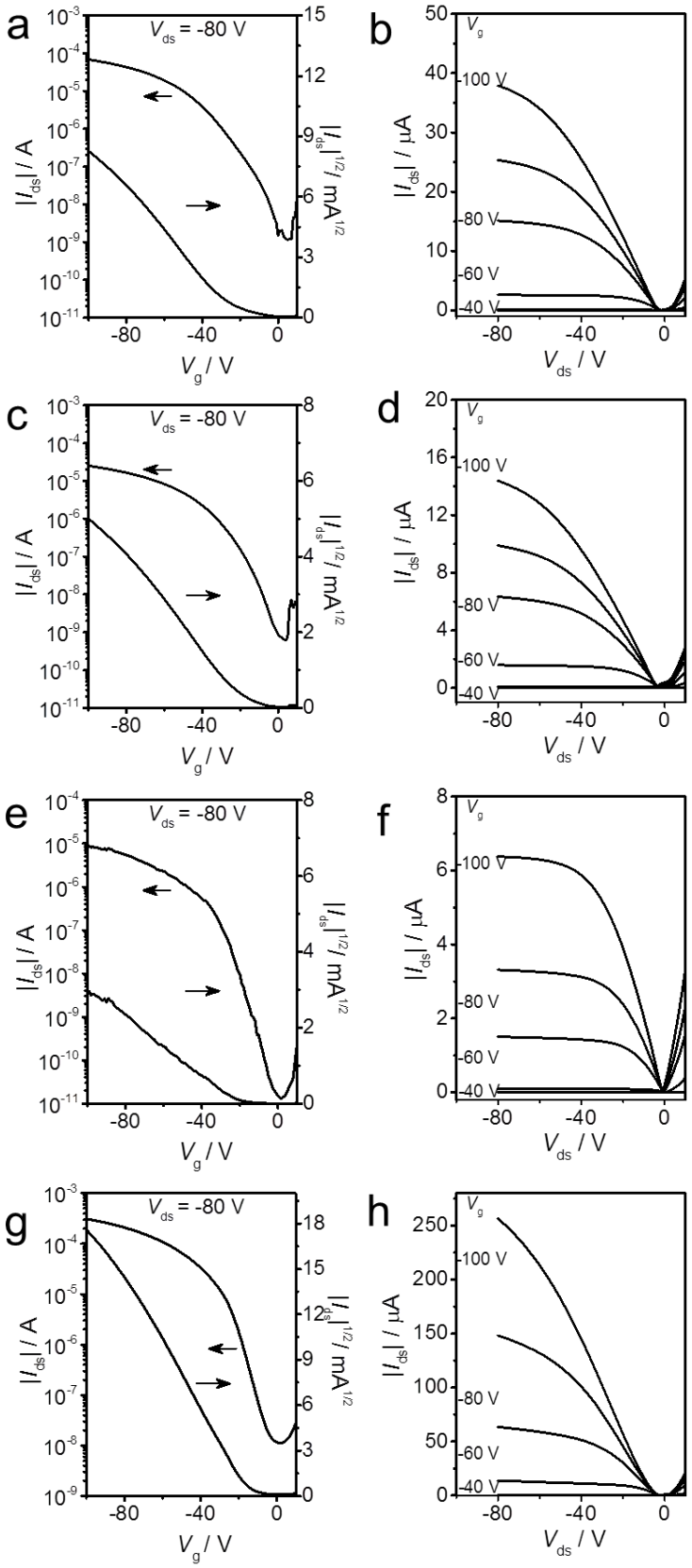

Figure 3.19. Transfer and output curves for spin-coated (a,b) DPP6T, (c,d) DPP6T:PMMA$_{(2480\ kDa,\ 10\%)}$ and drop-cast (e,f) DPP6T, (g,h) DPP6T:PMMA$_{(2480\ kDa,\ 10\%)}$.

3.6 Conclusion

This chapter demonstrates that using a minor amount of an insulating amorphous polymer binder efficiently improves the crystallization of small molecule OSCs during dip-coating. The crystalline morphology of DH4T is governed by blending PMMA, where high ratio and high molecule weight of PMMA contribute to high coverage ratio and alignment. The continuous aligned crystalline films show a stratified DH4T/PMMA layers: top DH4T layer and bottom PMMA layer. The alignment and phase separation of DH4T and PMMA contributes to an enhanced charge carrier transport in transistors. Maximum mobilities for dip-coated DH4T:PMMA are 6 times higher than those of corresponding drop-cast ones, and are comparable with those of vacuum sublimated films and single crystals. The role of polymer binder on the crystallization of small molecule OSCs are proved by dip-coating of DPP6T:PMMA. The mobility of dip-coated DPP6T:PMMA is 2.5 times higher than the drop-cast DPP6T:PMMA. The improved crystallization is attributed to the elevated mass transport induced by viscosity gradient owing to the polymer binder.

The content of this chapter has been published in: Advanced Functional Materials

Reprinted with permission from (Adv. Funct. Mater.2018, 28, 1805594)

Reference

1. Y. Yuan, G. Giri, A.L. Ayzner, A.P. Zoombelt, S.C. Mannsfeld, J. Chen, D. Nordlund, M.F. Toney, J. Huang and Z. Bao, *Nat. Commun.*, 2014, **5**: 3005.
2. A. Yamamura, S. Watanabe, M. Uno, M. Mitani, C. Mitsui, J. Tsurumi, N. Isahaya, Y. Kanaoka, T. Okamoto, and J. Takeya, *Sci.adv.*, 2018, **4**(2): eaao5758.
3. X. Xu, Y. Yao, B. Shan, X. Gu, D. Liu, J. Liu, J. Xu, N. Zhao, W. Hu and Q. Miao, *Adv. Mater.*, 2016, **28**(26): 5276-5283.
4. Y. Diao, L. Shaw, Z. Bao and S.C.B. Mannsfeld, *Energy Environ. Sci.*, 2014, **7**(7): 2145-2159.
5. X. Zhang, J. Jie, W. Deng, Q. Shang, J. Wang, H. Wang, X. Chen and X. Zhang, *Adv. Mater.*, 2016, **28**(13): 2475-2503.
6. H. Sun, Q. Wang, J. Qian, Y. Yin, Y. Shi and Y. Li, *Semicond. Sci. Technol.*, 2015, **30**(5): 054001.
7. W. Deng, X. Zhang, H. Dong, J. Jie, X. Xu, J. Liu, L. He, L. Xu, W. Hu and X. Zhang, *Mater. Today*, 2018.
8. K. Wu, H. Li, L. Li, S. Zhang, X. Chen, Z. Xu, X. Zhang, W. Hu, L. Chi, X. Gao and Y. Meng, *Langmuir*, 2016, **32**(25): 6246-6254.
9. W. Lee and Y. Park, *Polymers*, 2014, **6**(4): 1057-1073.
10. J. Smith, R. Hamilton, I. McCulloch, N. Stingelin-Stutzmann, M. Heeney, D.D.C. Bradley and T.D. Anthopoulos, *J. Mater. Chem.*, 2010, **20**(13): 2562.
11. P.S. Jo, D.T. Duong, J. Park, R. Sinclair and A. Salleo, *Chem. Mater.*, 2015, **27**(11): 3979-3987.
12. B.K. Kjellander, W.T. Smaal, J.E. Anthony and G.H. Gelinck, *Adv. Mater.*, 2010, **22**(41): 4612-4616.
13. M.R. Niazi, R. Li, E. Qiang Li, A.R. Kirmani, M. Abdelsamie, Q. Wang, W. Pan, M.M. Payne, J.E. Anthony, D.M. Smilgies, S.T. Thoroddsen, E.P. Giannelis and A. Amassian, *Nat. Commun.*, 2015, **6**: 8598.
14. K. Zhao, O. Wodo, D. Ren, H.U. Khan, M.R. Niazi, H. Hu, M. Abdelsamie, R. Li, E.Q. Li, L. Yu, B. Yan, M.M. Payne, J. Smith, J.E. Anthony, T.D. Anthopoulos, S.T. Thoroddsen, B. Ganapathysubramanian and A. Amassian, *Adv. Funct. Mater.*, 2016, **26**(11): 1737-1746.
15. X. Gu, L. Shaw, K. Gu, M.F. Toney and Z. Bao, *Nat. Commun.*, 2018, **9**(1): 534.
16. G. Qu, J.J. Kwok and Y. Diao, *Acc. Chem. Res.*, 2016, **49**(12): 2756-2764.

17. R. Janneck, F. Vercesi, P. Heremans, J. Genoe and C. Rolin, *Adv. Mater.*, 2016, **28**(36): 8007-8013.
18. S. Kaya, P. Rajan, H. Dasari, D.C. Ingram, W. Jadwisienczak and F. Rahman, *ACS Appl. Mater. Interfaces*, 2015, **7**(45): 25024-25031.
19. H. Bodiguel, F. Doumenc and B. Guerrier, *Langmuir*, 2010, **26**(13): 10758-10763.
20. T. Leydecker, D. Trong Duong, A. Salleo, E. Orgiu and P. Samori, *ACS Appl. Mater. Interfaces*, 2014, **6**(23): 21248-21255.
21. M.J. Large, S.P. Ogilvie, A.A.K. King and A.B. Dalton, *Langmuir*, 2017, **33**(51): 14766-14771.
22. S. Feng, D. Ma, Y. Qiu and L. Duan, *RSC Advances*, 2018, **8**(8): 4153-4161.
23. K. Norrman, A. Ghanbari-Siahkali and N.B. Larsen, *Annual Reports Section "C" (Physical Chemistry)*, 2005, **101**: 174.
24. R. Cheng, Y. Shao, M. Liu, R. Qian, Eur. Polym. J, *1998*, **34**(11): 1613-1619.
25. J.Y. Oh, W.S. Jang, T.I. Lee, J.-M. Myoung and H.K. Baik, *Appl. Phys. Lett.*, 2011, **98**(2): 023303.
26. Q. Yang, J. Wang, X. Zhang, J. Zhang, Y. Fu and Z. Xie, *Sci. China Chem.*, 2014, **58**(2): 309-316.
27. S. Kwon, J. Kim, G. Kim, K. Yu, Y.R. Jo, B.J. Kim, J. Kim, H. Kang, B. Park and K. Lee, *Adv. Mater.*, 2015, **27**(43): 6870-6877.
28. M. Moret, M. Campione, A. Borghesi, L. Miozzo, A. Sassella, S. Trabattoni, B. Lotz and A. Thierry, *J. Mater. Chem.*, 2005, **15**(25): 2444.
29. J. Chen, M. Shao, K. Xiao, Z. He, D. Li, B.S. Lokitz, D.K. Hensley, S.M. Kilbey, J.E. Anthony, J.K. Keum, A.J. Rondinone, W.-Y. Lee, S. Hong and Z. Bao, *Chem. Mater.*, 2013, **25**(21): 4378-4386.
30. C.J. Brinker, *Chemical Solution Deposition of Functional Oxide Thin Films*, Springer, Vienna, 2013.
31. Z.-T. Huang, C.-C. Fan, G.-B. Xue, J.-K. Wu, S. Liu, H.-B. Li, H.-Z. Chen and H.-Y. Li, *Chin. Chem. Lett.*, 2016, **27**(4): 523-526.

Chapter 4 Key role of meniscus shape on crystallization of organic semiconductors during meniscus-guided coating

4.1 Introduction

As Chapter 3 described, dip-coated pristine DH4T and DPP6T films are prone to non-uniform morphology and void formation due to the limited-mass-transport.[1] A small fraction of amorphous polymer binder efficiently improves the crystallization of DH4T and DPP6T. It was found that during dip-coating of OSC:polymer blend, polymer binder leads to the increase of mass transport for film growth. However, control of the self-assembly and morphology of pristine OSCs is still challenging but important for printed electronics. Especially, the crystallization mechanism of pristine OSCs during meniscus-guided coating is still not fully understood.[2]

As discussed in Chapter 4.1.3, the correlation between coating speed and film thickness during meniscus-guided coating has been well understood.[3, 4] In addition, a predictive model about optimizing coating speed to grow OSC film is proposed for meniscus-guided coating.[5] However, only little insight on the fundamental principles of the fluid mechanics and OSC crystallization has been provided. A comprehensive study of the relation between meniscus shape, fluid mechanical process and OSC crystal growth during meniscus-guided coating is still required.

In this chapter, I focus on the role of deposition parameters (meniscus shape and surface energy of substrate) on the physical processes such as fluid flow, mass transport and crystallization. Angle-dependent dip-coating (ADDC) is applied to precisely control the meniscus shape.[6] The experimental results on ADDC of C8-BTBT and two-dimensional fluid simulations reveal that the streamline stagnation point between the upward and recirculation flow is mainly affected by the meniscus shape. A narrow meniscus shape at

small β facilitates an upward flow leading to a larger concentration-gradient near the contact line favoring the crystal growth of the OSC. This fluid flow assisted crystallization is also favored by higher supersaturation caused by a lower solubility of the OSC. On the other hand, the crystallization is limited on substrates with low surface energy due to an elevated nucleation barrier. This work gives a comprehensive insight into the OSC crystallization behavior during meniscus-guided coating taking into account fluid mechanical processes.

4.2 ADDC of C8-BTBT

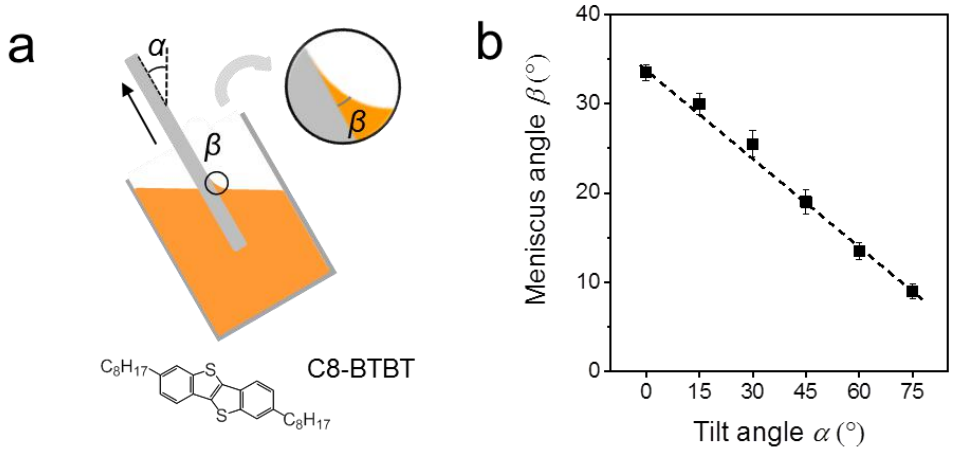

Figure 4.1. (a) Schematic diagram of ADDC and molecular structure of C8-BTBT (black arrow indicates coating direction). (b) Relation between β_{CHCl3} and α.

During meniscus-guided coating of OSCs, the meniscus refers to the liquid shape between substrate and coating head or bulk solution, which is determined by a combination of surface tension and external forces (usually gravity).[7] The meniscus shape (described by β) is not only influenced by surface energy of substrate and surface tension of solvent, but also depends on the substrate tilt angle (α) during dip-coating (Figure 4.1a) or the distance of coating head to the substrate during slot coating and zone-casting. When a S_{plasma} is immerged into $CHCl_3$, a capillary action occurs at the interface between S_{plasma} and bulk solvent and a

stable meniscus is achieved immediately. The meniscus angle of $CHCl_3$ (β_{CHCl3}) decreases from 33° to less than 10° when S_{plasma} is tilted from $\alpha_{0°}$ to $\alpha_{75°}$ (Figures 4.1b and 4.2).

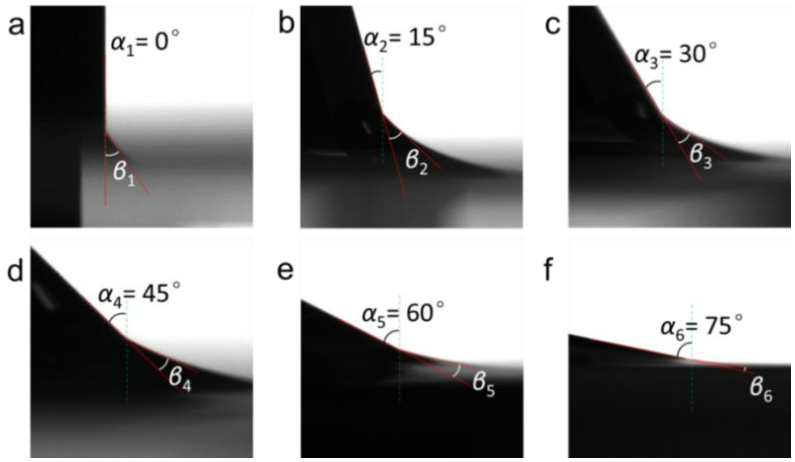

Figure 4.2. Meniscus shape on the S_{plasma} in $CHCl_3$ at tilt angles of (a) $\alpha_{0°}$, (b) $\alpha_{15°}$, (c) $\alpha_{30°}$, (d) $\alpha_{45°}$, (e) $\alpha_{60°}$, (f) $\alpha_{75°}$. The meniscus shape is described by the meniscus angle (β).

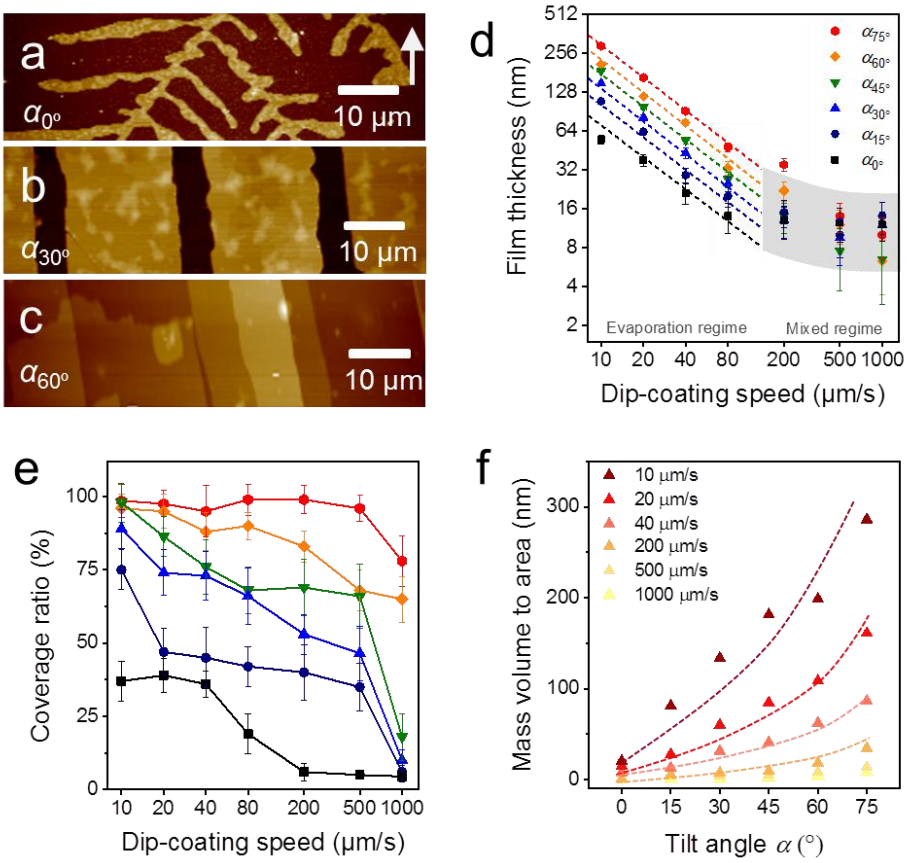

Figure 4.3. Morphology of C8-BTBT crystals obtained at (c) $\alpha_{0°}$, (d) $\alpha_{30°}$ and (e) $\alpha_{60°}$ by ADDC at 20 µm/s (the white arrow indicates coating direction). (f) Film thickness and (g) coverage ratio of C8-BTBT as a function of dip-coating speed for different α. (h) Mass deposition of C8-BTBT for different dip-coating speeds as a function of α.

To investigate the role of the meniscus shape on the OSC deposition, C8-BTBT was coated by ADDC on S_{plasma} from $CHCl_3$. During dip-coating of C8-BTBT at 20 µm/s, β_{CHCl3} on S_{plasma} was precisely controlled by solely varying α.[8] At $\alpha_{0°}$ dendritic crystals are grown due to the limited-mass-transport of C8-BTBT (Figure 4.3a).[3, 9] When the substrate is tilted to $\alpha_{30°}$, the growth of dendritic crystals is suppressed and the film turns into crystalline ribbons aligned in the coating direction (Figure 4.3b). This implies an enhanced mass transport for the crystal growth caused by the substrate tilting. At further substrate tilting of $\alpha_{60°}$, a terrace-like crystalline morphology is formed (Figure 4.3c).

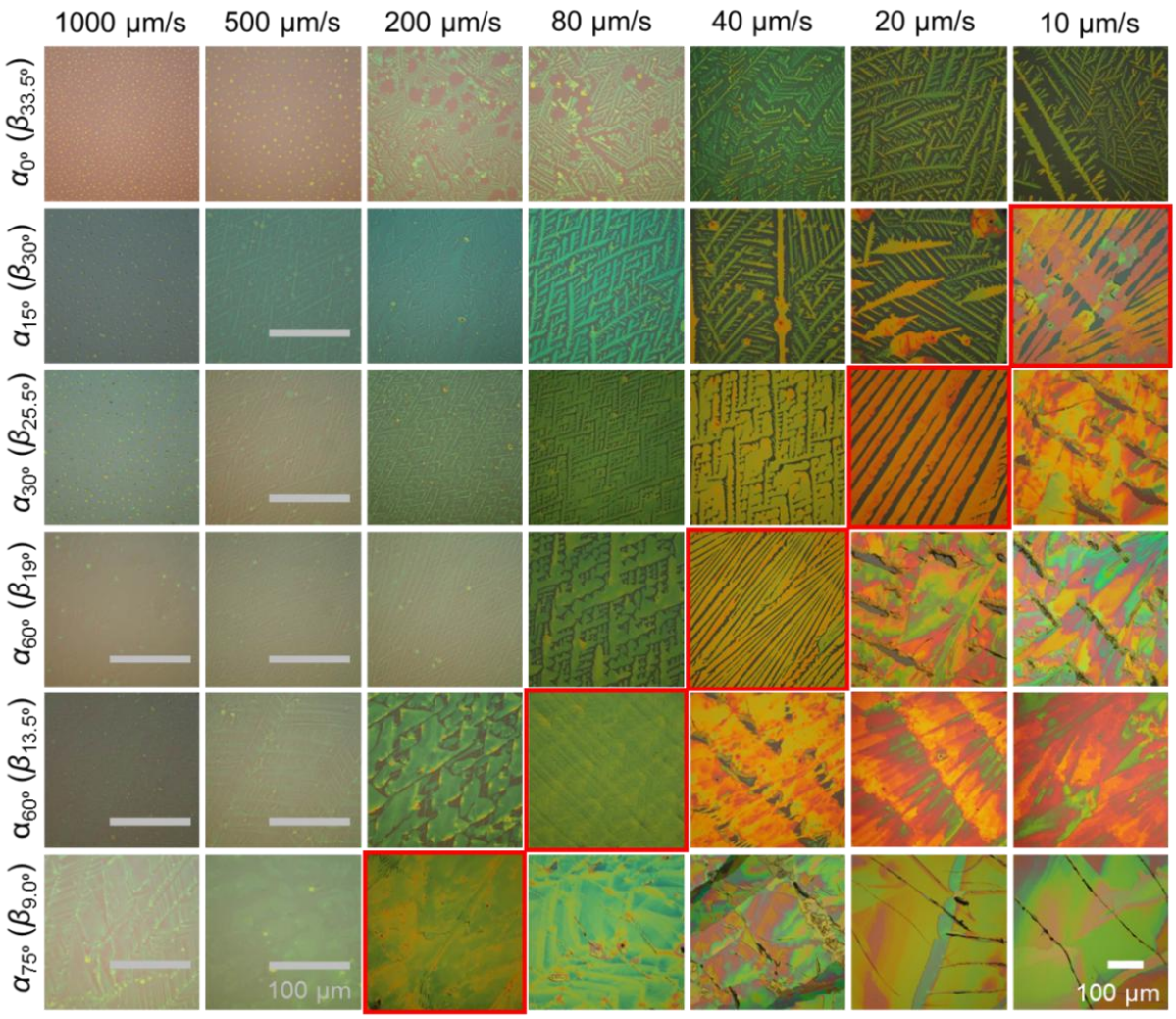

Figure 4.4. Optical microscopy images of C8-BTBT film morphologies cast by ADDC at different dip-coating speeds and α. The grey and white scale bars represent 100 µm; the white scale bar corresponds to the images with bar. Images of aligned crystalline ribbons are indicated by a red frame.

During ADDC of C8-BTBT in speeds range from 10 µm/s to 1000 µm/s, the deposition regimes are characterized by the resulting film thickness. As shown in Figure 4.3d, the evaporation regime is established for deposition speeds from 10 µm/s to 80 µm/s characterized by a power-law decrease (exponent -1) in film thickness, while the mixed regime is found between 200 µm/s and 1000 µm/s. Interestingly, in the evaporation regime of ADDC, the film thickness is greatly influenced by α. For instance, for a dip-coating speed of 10 µm/s, the film thickness is around 200 nm at $\alpha_{60°}$ and 3 times higher than at $\alpha_{0°}$ (Figure 4.3d). In addition, the coverage of the crystalline C8-BTBT film also improves with larger α, as show in Figures 4.3e and 4.4. For dip-coating speeds between 20 µm/s to 500 µm/s, the coverage ratio is below 50% for α between 0° and 15°, and increases to above 75% for α between 60° and 75°. The mass deposition (mass volume to area) of C8-BTBT for different dip-coating speeds derived from the thickness and coverage ratio implies that a large α (or small β) enhances the mass transport for the film deposition (Figure 4.3f).

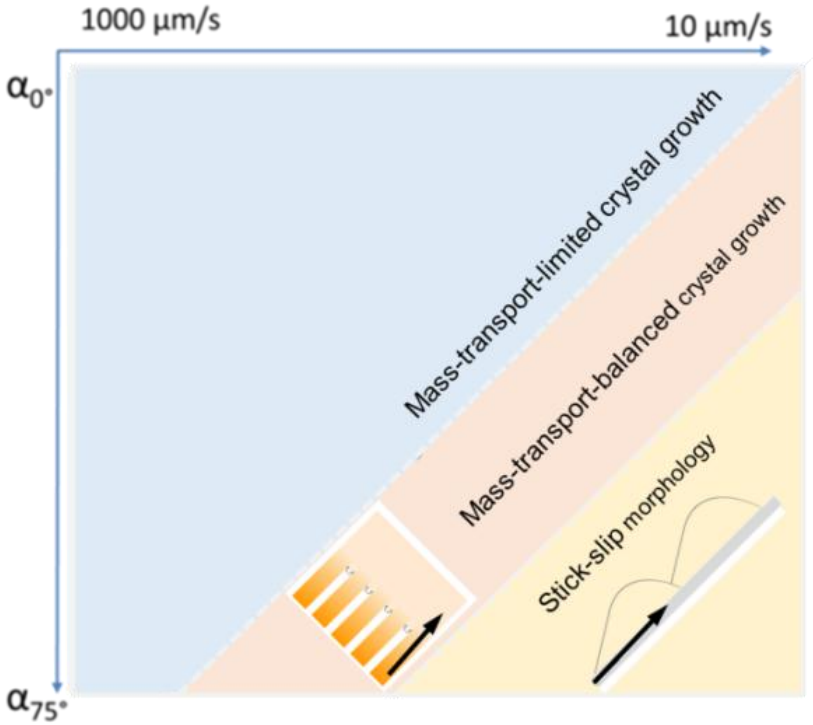

Figure 4.5. Subdivision of different growth regimes during ADDC of C8-BTBT (compare to Figure 4.4).

The crystalline C8-BTBT films obtained at different dip-coating speeds and α, exhibit distinct morphologies, such as crystalline dots, dendrites, ribbons, and slip-stick structures (Figures 4.4 and 4.5).[10, 11] Aligned crystalline ribbons result from balanced-mass-transport at appropriate dip-coating speed and α, as highlighted by the red frame of the corresponding optical microscopy images in Figure 4.4. Limited-mass-transport in the regimes of elevated dip-coating speed and low α leads to crystal-dots and dendritic growth. On the other hand, in regime of low dip-coating speed and large α, the competition between pinning and depinning forces induces a "stick-slip" morphology with a certain spacing/stripe ratio.[2] The reduced spacing at high α contributes to the raised coverage ratio. It implies that the formation of the stick-slip morphology is subjected to the meniscus shape.

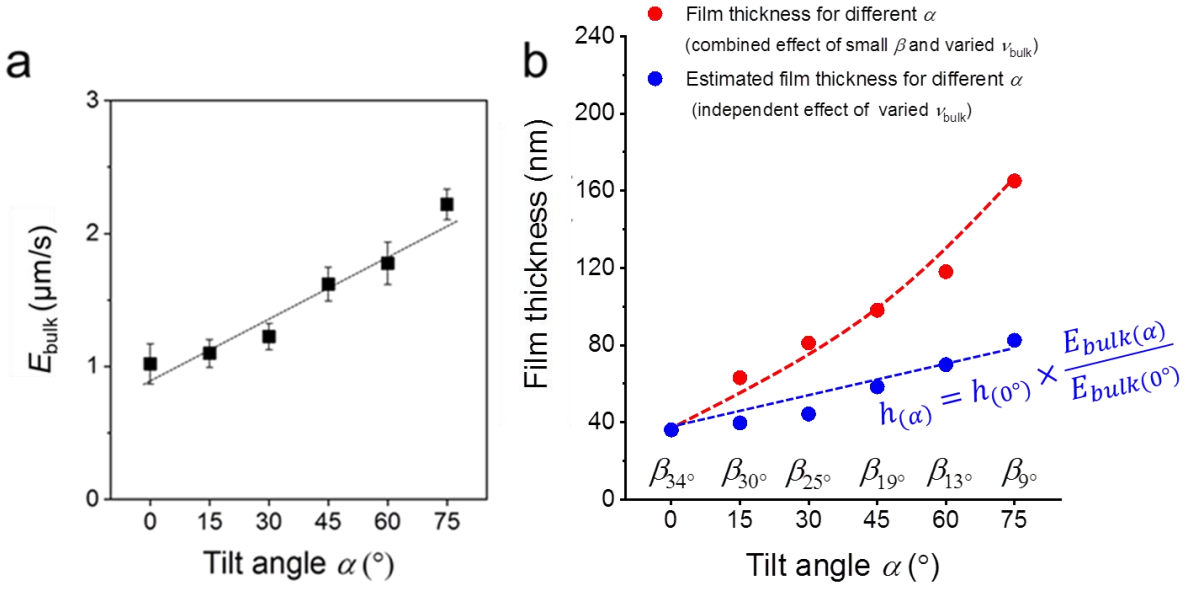

Figure 4.6. (a) Average evaporation rates for bulk solution (E_{bulk}) for different α determined by the decrease of the liquid level of the bulk solution in container per second. (b) Film thickness of C8-BTBT obtained by ADDC at 20 µm/s is indicated by red dots. Dashed lines are eye guides. The film thickness for varied E_{bulk} (blue dots) is estimated from the included equation.

Since the thickness of the dip-coated films is proportional to the evaporation rate of the bulk solution (E_{bulk}),[4] $E_{bulk(\alpha)}$ was measured to clarify its influence on film thickness at various α. During ADDC of C8-BTBT from a not completed solvent filled vial (15 mL),

$E_{bulk(75°)}$ is around 2.3 times larger than $E_{bulk(0°)}$ at $\alpha_{0°}$ (Figure 4.6a), wherein this difference (varied $E_{bulk(\alpha)}$) is attributed to the change of the liquid level during tilting the vial (Figure 1a). To perform fluid simulation, average $E_{bulk(\alpha)}$ for different α are estimated by

$$E_{bulk} = \frac{V}{A * t}$$

wherein V is the evaporated solvent volume, A is the area of solution-air interface in container, t is time (Figure 4.6a).

On the other hand, the film thickness at $\alpha_{75°}$ is 4.5 times higher than at $\alpha_{0°}$, and thus different from the $E_{bulk(75°)}/E_{bulk(0°)}$ ratio (Figure 4.6b), indicating a substantial impact of the meniscus shape on the mass deposition during ADDC.

4.3 Fluid flow at the meniscus

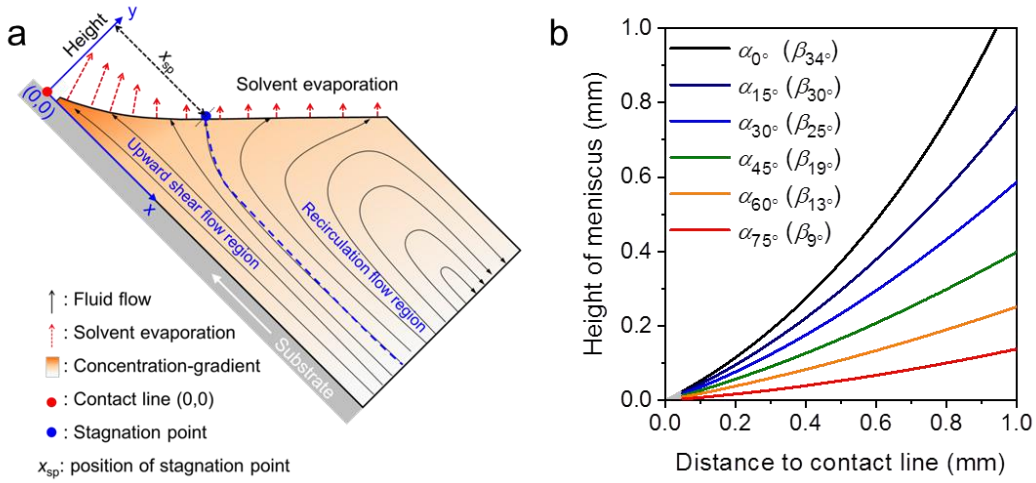

Figure 4.7. Two-dimensional (2D) fluid simulation for ADDC. (a)Key parameters in the applied meniscus model. (b) Meniscus height for different β derived from optical images in Figure 4.2.

To better understand the role of the meniscus shape on the film formation during meniscus-guided coating, the fluid mechanical process at the meniscus has been explored. During ADDC, the fluid flows involve capillary flow induced by non-uniform solvent

evaporation, Marangoni flow caused by surface tension gradient, and Couette flow driven by substrate movement.[12] A fundamental feature is the presence of a stagnation point, where the streamline is perpendicular to the solution surface, separating the fluid into “upward flow region” and “recirculation flow region” (Figure 4.7). Modelling the fluid flow at the meniscus is challenging including various factors, such as surface tension of solvent, and surface energy of substrate, viscosity. Alternatively, we focus on the fundamental role of the meniscus shape on the fluid mechanical process and film growth. A two-dimensional fluid simulation was performed based on the Stokes flow, whereby the Marangoni effect is ignored. All fluid simulations were performed in the evaporation regime at a dip-coating speed of 20 µm/s. The meniscus shapes for different β were derived from the optical images in Figure 4.2. The plots in Figure 4.7b demonstrate that the meniscus height and β decrease simultaneously, whereby for $\beta < 15°$ the height is less than 0.25 mm at $x < 1$ mm. The meniscus model for different geometries was established including solvent evaporation, fluid flow, and concentration gradient. The x-axis of the Cartesian coordinate represents the distance along the substrate from the contact line, while y-axis is related to the height perpendicular to the substrate (Figure 4.7).

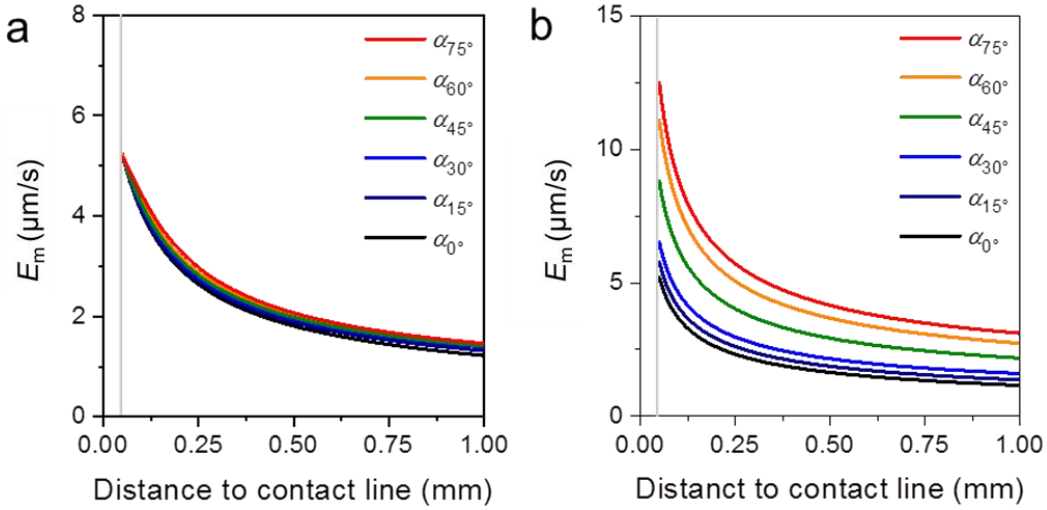

Figure 4.8. E_m is calculated based on (a) constant $E_{bulk(0°)}$ and (b) varied $E_{bulk(\alpha)}$.

The evaporation rate at the meniscus (E_m) for different α is determined by the solvent vapor pressure, which is related to meniscus height and $E_{bulk(\alpha)}$.[4] The results calculated by the fluid simulation are shown in Figure 4.8. To exclude the influence of varied $E_{bulk(\alpha)}$, the fluid simulations for different β were performed at constant $E_{bulk(0°)}$. Under these conditions, E_m is independent on β and decreases with the distance from contact line (Figure 4.8a). At the same time, the distance of the stagnation point (x_{sp}) from the contact line shifts from 0.26 mm to 3.40 mm when β declines from 33.5° to 9° (Figure 4.9a). This implies that a small β favors the upward flow and in this way transports more solute to the contact line for crystallization, inducing a larger concentration gradient at the meniscus (Figure 4.10). For instance, at x = 0.1 mm, the solute concentration (c_m) at $\beta_{13°}$ ($\alpha_{60°}$) is 2 and 3 times higher than at $\beta_{25°}$ ($\alpha_{30°}$) and $\beta_{34°}$ ($\alpha_{0°}$), respectively (Figure 4.9b). Due to raised c_m caused by small β, the C8-BTBT is more prone to saturate and nucleate at the contact line.

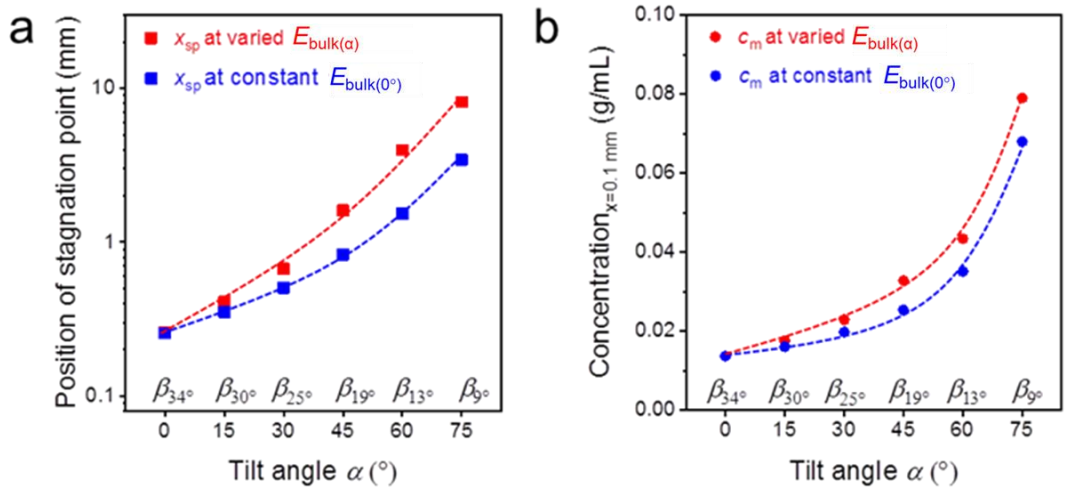

Figure 4.9. Two-dimensional fluid simulation for ADDC. (a) Position of stagnation point (x_{sp}) as function of α. (b) Solute concentration at the meniscus (c_m) at x = 0.1 mm as function of α.

The fluid simulation for different α (and β) was also performed for varied $E_{bulk(\alpha)}$ condition to compare with the experimental data obtained for ADDC of C8-BTBT. Besides the contribution of small β, the gradually larger E_{bulk} additionally increases E_m and intensifies the upward flow (Figure 4.9). In comparison to constant E_{bulk}, at varied (higher) E_{bulk} the

stagnation point is shifted further away from the contact line (Figure 4.9a) and leads to a higher c_m (Figure 4.9b for x = 0.1 mm as example). In addition to varied (higher) E_{bulk}, a small β can significantly enhance the upward fluid flow during meniscus-guided coating resulting in a higher concentration at the narrow meniscus and finally in greater film thickness (Figure 4.3).

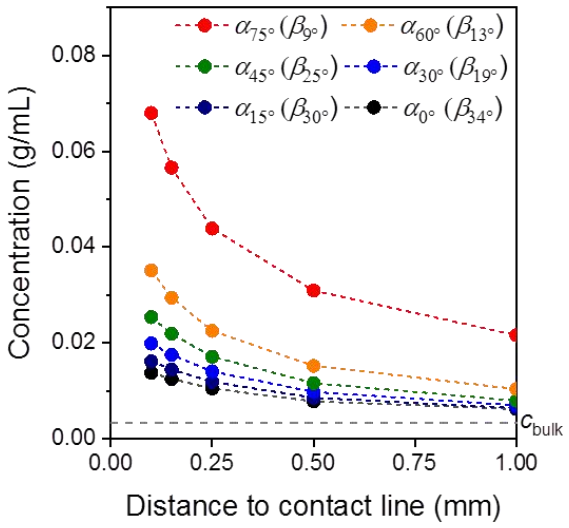

Figure 4.10. Solute concentration at the meniscus (cm) calculated at constant Ebulk.

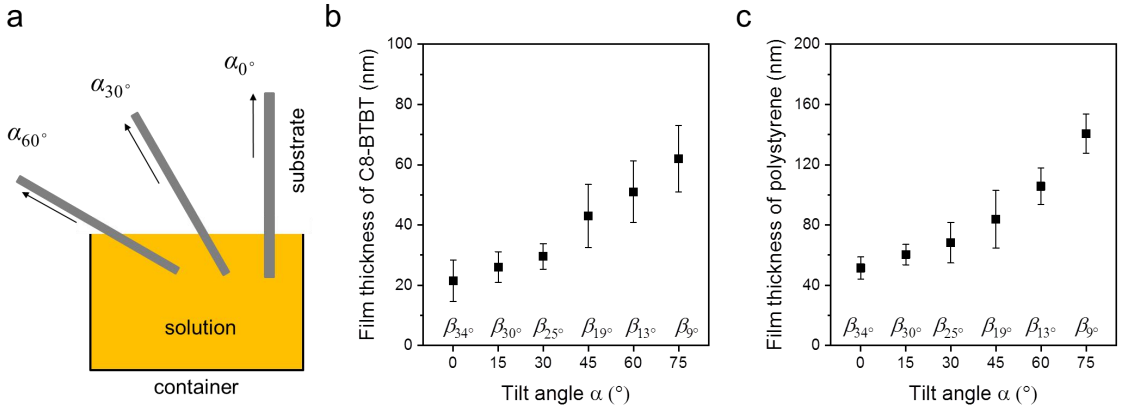

Figure 4.11. (a) Schematic illustration of ADDC from large container completely filled by the solution achieving a constant E_{bulk} at experimental conditions. (b) Film thickness of C8-BTBT obtained by ADDC at 200 µm/s from large container completely filled by $CHCl_3$ (3 mg/mL). (c) Film thickness of polystyrene (400 kDa) obtained by ADDC at 80 µm/s from large container completely filled by $CHCl_3$ (1 mg/mL).

ADDC was also performed from a larger container (50 mL) completely filled by the solution to achieve a constant E_{bulk} and exclude the influence of varied E_{bulk} at experimental

conditions (Figure 4.11a). Due to extensive material consumption, these experiments were performed for two representative cases. C8-BTBT and polystyrene (400 kDa) were dip-coated at 200 μm/s and 80 μm/s, respectively. As shown in Figure 4.11b,c, higher film thicknesses of C8-BTBT and polystyrene were obtained at greater α, where the increased mass deposition results solely from small β. These results directly confirm the role of the meniscus shape on the mass deposition during meniscus-guided coating.

4.4 Surface energy of substrate

The OSC crystallization during meniscus-guided coating is more complex, including not only the fluid flow, but also the supersaturated concentration as driving force and barrier for crystal nucleation and growth. The crystallization behavior of OSCs greatly depends on the substrate roughness, surface energy of substrate, concentration and solubility.[13] For instance, the nucleation barrier for a 2D spherulite heterogeneous nucleation in solution deposited films, ΔG^*_{het}, is determined by concentration (c), solubility (δ), temperature (T), the surface energy between solution and crystals (γ_{CL}),[14]

$$\Delta G^*_{het} = \frac{-16\pi^3\gamma_{CL}^3}{3(k_BT)^3\left(\ln\left(\frac{c}{\delta}\right)\right)^2} f(\vartheta) \quad (2)$$

where k_B is Boltzmann's constant, and the shape factor $f(\vartheta)$ is influenced by substrate surface energy.

Table 4.1. Contact angles (θ) of probe liquids on various substrates.

	γ_{LV} (mN/m)	S_{OTS}	S_{HMDS}	S_{bare}	S_{plasma}
Ethylene glycol	47.7	104.2±3.4	87.2±2.9	46.0±4.3	11.2±1.9
Formamide	59.1	96.6±1.3	81.1±1.5	40.2±2.5	11.0±1.3
Glycerol	65.0	92.0±1.3	67.0±2.7	29.3±2.2	
Water	72.7	68.4±2.6	30.3±2.0		

To deeper understand the role of the meniscus on OSC crystallization, the influence of surface energy of substrate on film coating of C8-BTBT was studied. The modulation of surface energy of substrate was achieved by plasma treatment and self-assembled monolayer modification of the substrate using HMDS and OTS. The substrate surface energy can be estimated by combining the equation of state with the Young's equation.[13] Details on the contact angle measurements and fittings are shown in Table 4.1 and Figure 4.12.

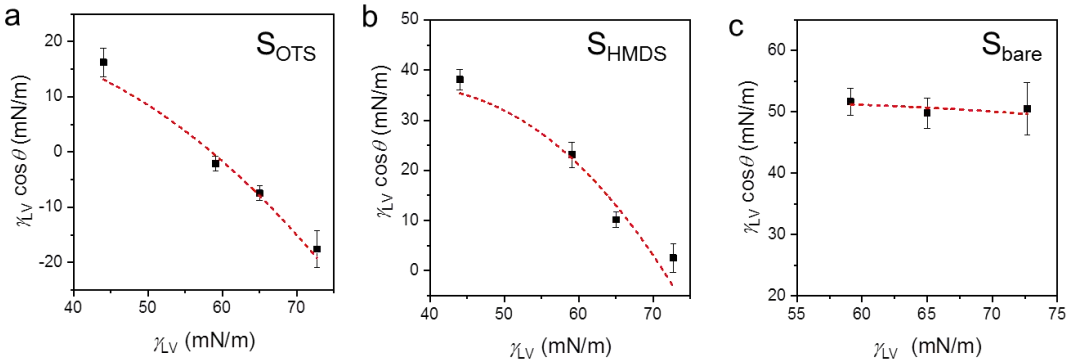

Figure 4.12. Determination of substrate surface energy via the equation of state approach. The plot shown is the comparison between experimental data and fitted curve obtained from the equation of state.

Determination of substrate surface energy via the equation of state approach[13]:

$$cos\theta = -1 + 2\sqrt{\frac{\gamma_{SV}}{\gamma_{LV}}}(1 - \xi(\gamma_{LV} - \gamma_{SV})^2) \qquad \text{(Equation 4.1)}$$

wherein γ_{LV} is the surface tension of solvent and γ_{SV} is the substrate surface energy, and ξ is an empirical constant unique for each substrate, introduced to reduce the fitting error.

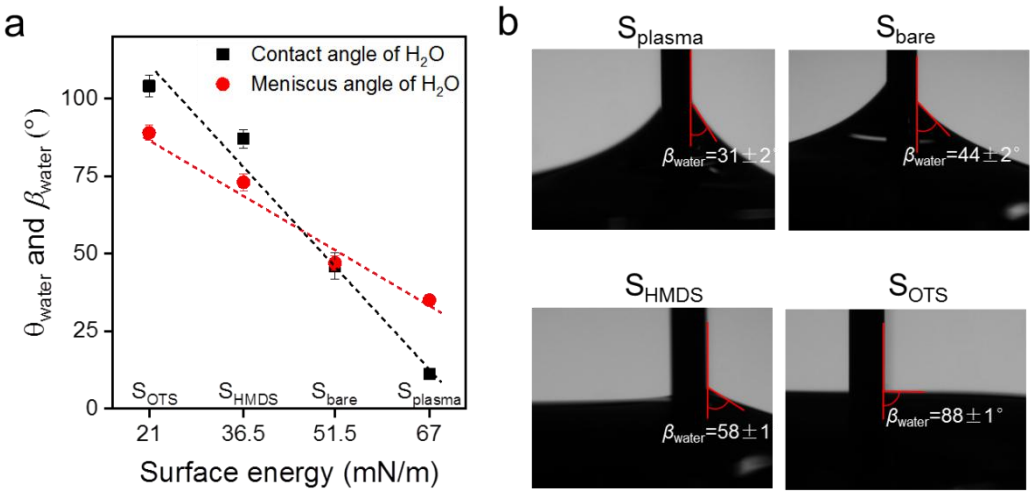

Figure 4.13. (a) θ_{water} and β_{water} on substrates with different surface energy. (b) Optical images of meniscus shape of β_{water} at substrates with different substrate surface energy for $\alpha_{0°}$.

As presented in Figure 4.13, substrate surface energy is modulated over a wide range from 21 to 67 mN/m. The surface energy for bare SiO_2 surface (S_{bare}) is around 51.5 mN/m and for S_{plasma} it is 67 mN/m. However, HMDS and OTS modifications (S_{HMDS} and S_{OTS}) decrease surface energy to 36.5 and 21 mN/m, respectively (Figure 4.13).[13, 15] The meniscus angle of water (β_{water}) at $\alpha_{0°}$ increases from 31° to 88° when surface energy declines from 67 to 21 mN/m (Figure 4.13). This trend corresponds to the surface energy dependent contact angle of water (θ_{water}).

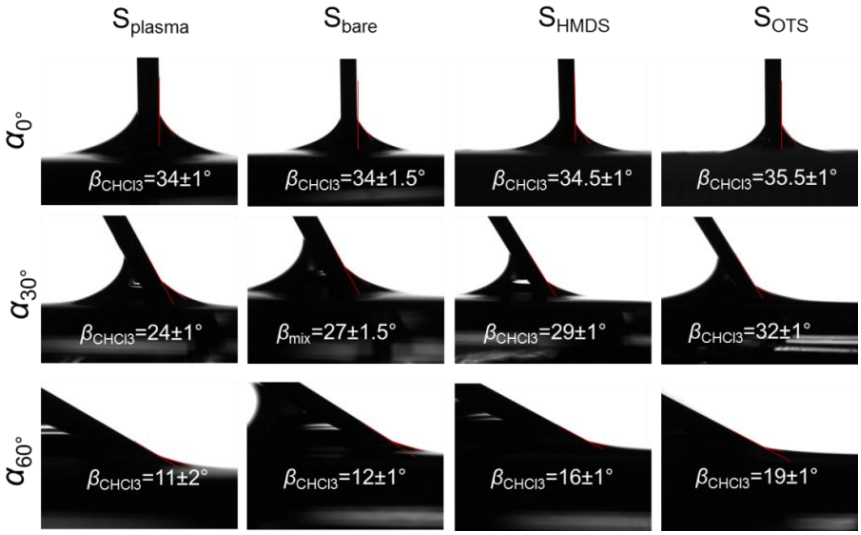

Figure 4.14. Meniscus angles of $CHCl_3$ (β_{CHCl3}) at substrates with different surface energy for $\alpha_{0°}$, $\alpha_{30°}$ and $\alpha_{60°}$.

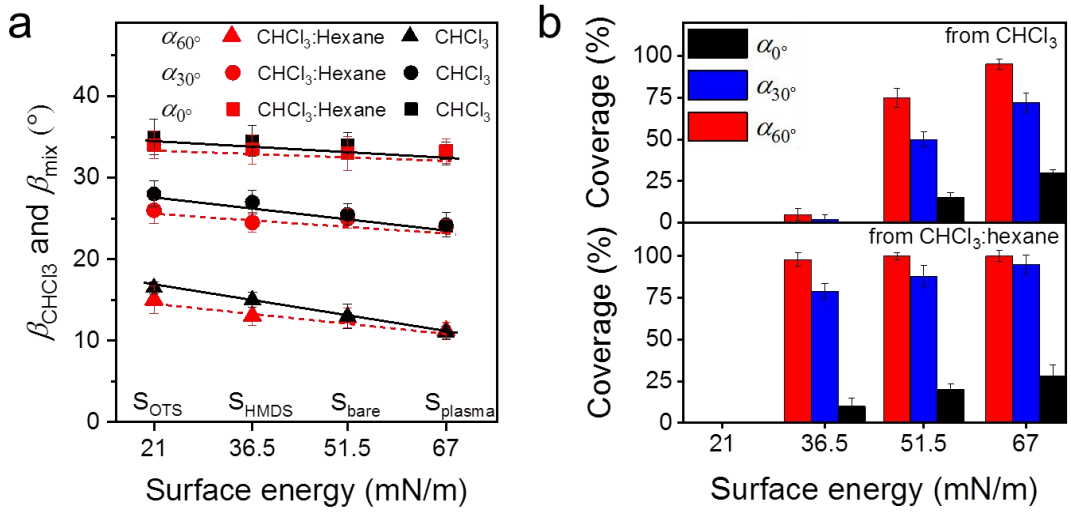

Figure 4.15. (a) β_{CHCl3} and β_{mix} at different α as a function of surface energy. (b) The coverage of C8-BTBT obtained from (top) $CHCl_3$ and (bottom) mixed-solvent $CHCl_3$:hexane (4:1) on substrates with different surface energy.

In contrast to β_{water}, β_{CHCl3} remains around 33°-35.5° for the same surface energy range (Figures 4.14 and 4.15a). The surface energy independent behavior of β_{CHCl3} is owing to the much lower surface tension of $CHCl_3$ (26.7 mN/m) compared to water (72.7 mN/m). However, the coverage ratio and crystallization of C8-BTBT during coating at $\alpha_{0°}$ and 20 µm/s significantly rely on substrate surface energy. The coverage is reduced for small surface energy which is also related to morphology changes in the film (Figure 4.16). For instance, at $\alpha_{0°}$ the dendritic C8-BTBT crystals on S_{plasma} are much wider than those on S_{bare}, but almost no nucleation occurs on S_{HMDS} and S_{OTS} (Figure 4.16). For different surface energy, β_{CHCl3} gradually decreases when α changes from 0° to 30° and 60° (Figure 4.15). The declined β_{CHCl3} leads to a higher coverage of C8-BTBT on S_{plasma} and S_{bare}, but does not efficiently improve the crystallization on S_{HMDS} and S_{OTS} (Figure 4.16).

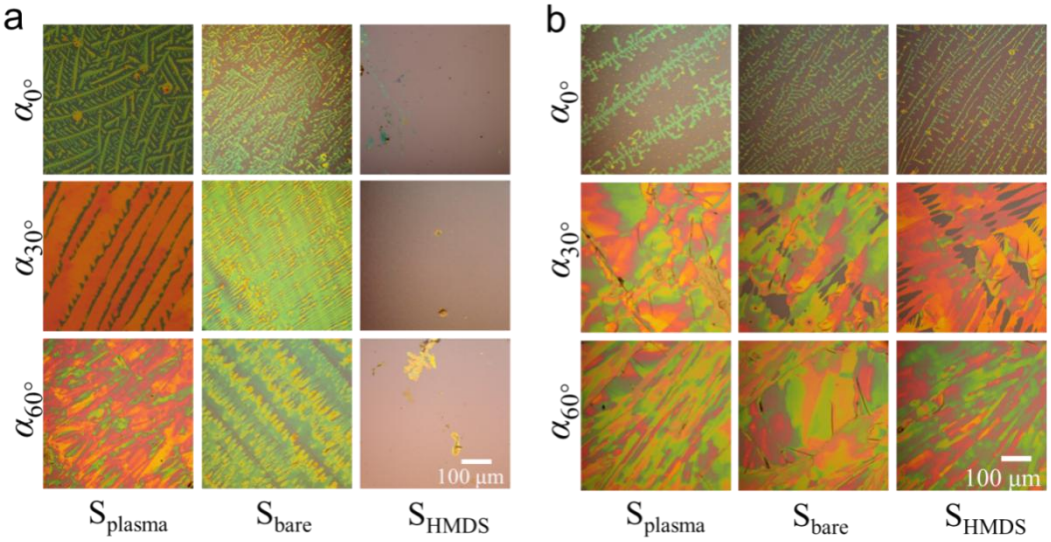

Figure 4.16. Optical microscopy images for film morphologies of dip-coated C8-BTBT at 20 µm/s and at $\alpha_{0°}$, $\alpha_{30°}$ and $\alpha_{60°}$ on substrates with different surface energy from (a) $CHCl_3$ and (b) mixed-solvent (4:1 $CHCl_3$:hexane). Scale bar is valid for all images.

Therefore, in the case of a similar β during meniscus-guided coating, the crystallization of OSC still significantly depends on substrate surface energy. Differences in the crystallization behavior are attributed to the surface energy dependent nucleation barrier which decreases in the order $\Delta G^*_{OTS} > \Delta G^*_{HDMS} > \Delta G^*_{bare} > \Delta G^*_{plasma}$ (Figure 4.17).[16, 17] These results indicate that the fluid flow assisted crystallization on low surface energy substrates is weakened by the high nucleation barrier.

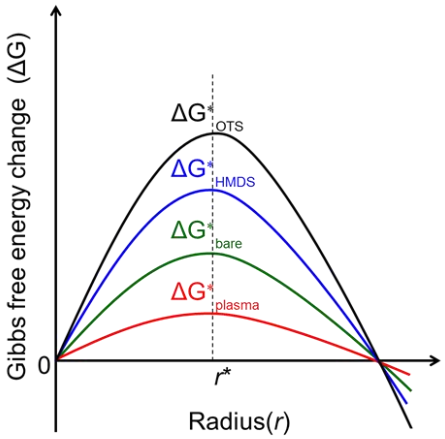

Figure 4.17. The influence of substrate surface energy on the nucleation barrier, ΔG^*, on different substrates. r^* indicates the crucial size for nucleation, where ΔG decreases with the increase of r when $r > r^*$.

To facilitate the fluid flow assisted crystallization on low surface energy substrate, a mixed-solvent ($CHCl_3$:hexane 4:1) was introduced to reduce solubility of C8-BTBT and thus to improve the supersaturation. The meniscus angle of the mixed-solvent (β_{mix}) is also surface energy independent. At the same α, β_{mix} is slightly lower than β_{CHCl3} resulting from smaller surface tension of hexane (18.4 mN/m), as shown in Figures 4.15a and 4.18. When dip-coated at $\alpha_{0°}$ and 20 µm/s from mixed-solvent, C8-BTBT exhibits dendritic morphologies with low coverage on S_{plasma}, S_{bare}, and S_{HMDS}. The coverage of C8-BTBT greatly enhances at larger α and reaches above 95% at $\alpha_{60°}$ (Figure 4.16b).

This coverage improvement at large α (small β) is directly attributed to the increased upward flow and the reduced solubility, leading to higher supersaturation necessary to overcome the nucleation barrier on S_{HMDS}. This means that to some extent the fluid flow assisted crystallization is facilitated by the raised supersaturation. However, even under the same deposition conditions no nucleation occurs on S_{OTS}, which may require a much higher supersaturation of C8-BTBT for nucleation on this type of surface during dip-coating. Because of this reason, the substrate surface modification by self-assembled monolayer of moderate surface energy provides the appropriate requirements for excellent mobility OFETs through the improvement of the crystallization during meniscus-guided coating at small β and reduction of the trap density at the interface.

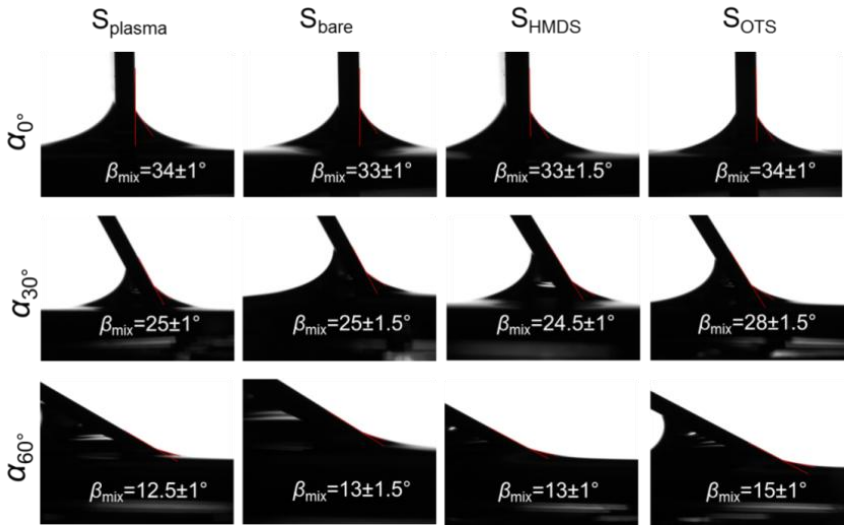

Figure 4.18. Meniscus angles of mixed-solvent (β_{mix}) at substrates with different surface energy for $\alpha_{0°}$, $\alpha_{30°}$ and $\alpha_{60°}$.

4.5 Molecular organization and OFETs

4.5.1 Molecule organization

To study the packing of C8-BTBT in the dip-coated films, GIWAXS was performed. The GIWAXS patterns of dip-coated C8-BTBT films indicate identical molecular packing in films cast at 20 µm/s from $CHCl_3$ at $\alpha_{0°}$, $\alpha_{30°}$, and $\alpha_{60°}$ on S_{plasma} (Figure 4.19). The distinct out-of-plane scattering intensity at q_z = 0.22 Å^{-1} for q_{xy} = 0 Å^{-1} is assigned to an interlayer distance of 2.85 nm.[18] The in-plane reflection at q_z = 0 Å^{-1} and q_{xy} = 1.90 Å^{-1} is associated to a π-stacking distance of 0.33 nm that is characteristic for a preferential edge-on organization of the molecules towards the surface, where the long molecular axis is parallel to the out-of-plane direction. The higher reflection intensity at $\alpha_{60°}$ is related to the greater film thickness, whereas the low intensity at $\alpha_{0°}$ is attributed to the low surface coverage.

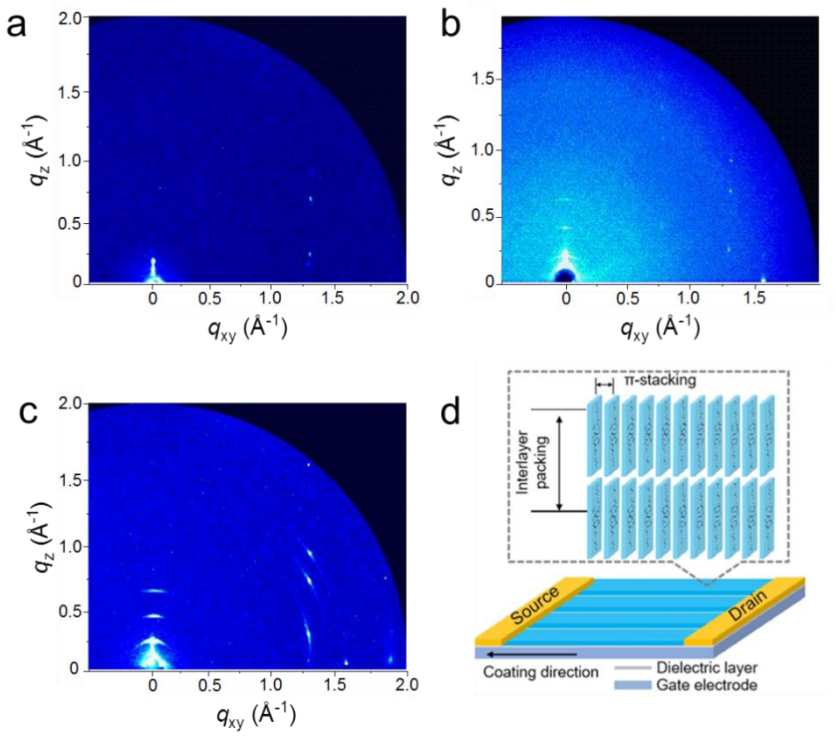

Figure 4.19. GIWAXS patterns of dip-coated C8-BTBT at 20 µm/s from $CHCl_3$ on S_{plasma} for (a) $\alpha_{0°}$, (b) $\alpha_{30°}$ and (c) $\alpha_{60°}$. (d) Schematic of C8-BTBT packing in the dip-coated OFETs.

4.5.2 OFETs

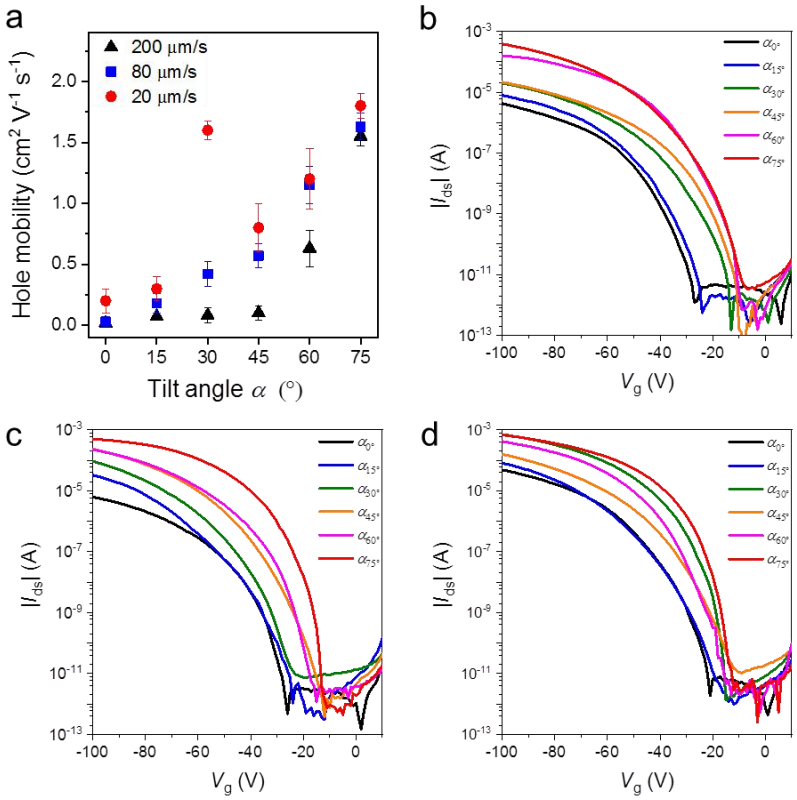

Figure 4.20. (a) Average mobilities of C8-BTBT on S_{plasma} dip-coated from $CHCl_3$ at different speeds as a function of α. Transfer curves at V_{ds}= -100 V for C8-BTBT dip-coated on S_{plasma} from 3 mg/mL $CHCl_3$ at (b) 200 µm/s, (c) 80 µm/s, and (d) 20 µm/s.

To probe the charge carrier transport of C8-BTBT obtained by ADDC, bottom-gate and top-contact transistors were fabricated, where the channel length (25 µm) was parallel to the coating direction (Figure 4.19). The average charge carrier mobilities of crystalline C8-BTBT films dip-coated on S_{plasma} increase with larger α for different dip-coating speeds (Figure 4.20a). As derived from the transfer curves, the transistors show a pronounced I_{on}/I_{off} ratio of around 10^7-10^8. When dip-coated at 200 µm/s, dendritic crystals and low coverage ratio of C8-BTBT lead to a mobility of less than 0.2 $cm^2\ V^{-1}\ s^{-1}$ at $\alpha < 45°$ which improves for $\alpha > 60°$ (Figure 4.20a,b). At the deposition speed of 80 µm/s, the mobilities gradually rise from 0.03 $cm^2\ V^{-1}\ s^{-1}$ to 1.5 $cm^2\ V^{-1}\ s^{-1}$ with larger tilt angle α (Figure 4.20a,c). The enhanced mobility is attributed to the improvement in both coverage ratio and crystalline morphology of C8-BTBT films (Figure 4.21a,b). At the same time, the turn-on voltage is reduced from -25

V to around -15 V. The generally high turn-on voltage results from the surface trapping on S_{plasma} and injection barrier induced by the mismatch between the work function of gold (-5.0 eV) and the HOMO level of C8-BTBT (-5.6 eV). [40, 41]

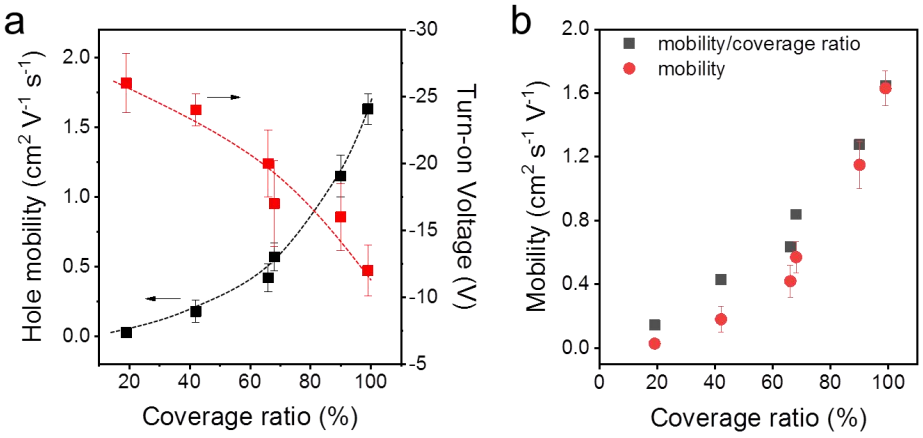

Figure 4.21. (a) Relation between hole mobility, turn-on voltage, and coverage ratio for C8-BTBT on S_{plasma} from $CHCl_3$ at 80 µm/s. (b) Charge carrier mobility of C8-BTBT (related to Figure 4.21a, deposited on S_{plasma} from $CHCl_3$ at 80 µm/s) without (red dots) and with (black dots) taking the true contact width into account. The corrected mobility (black dots) is extracted from the measured mobility divided by coverage ratio. The corrected mobility also increases with higher coverage ratio indicating that the enhanced charge transport results from the improved crystalline morphology of the deposited film.

At 20 µm/s, the mobility also increases from 0.2 $cm^2\ V^{-1}\ s^{-1}$ to 1.8 $cm^2\ V^{-1}\ s^{-1}$ for α from 0° to 75°, except the extraordinary high upwards outlier of 1.6 $cm^2\ V^{-1}\ s^{-1}$ at $\alpha_{30°}$ (Figure 4.20 a,d). This value found only for $\alpha_{30°}$ and 20 µm/s results from the well aligned crystalline structures (Figure 4.4). This confirms the common knowledge that both high coverage ratio and pronounced alignment of crystalline films are important for the charge transport in OFETs.[1]

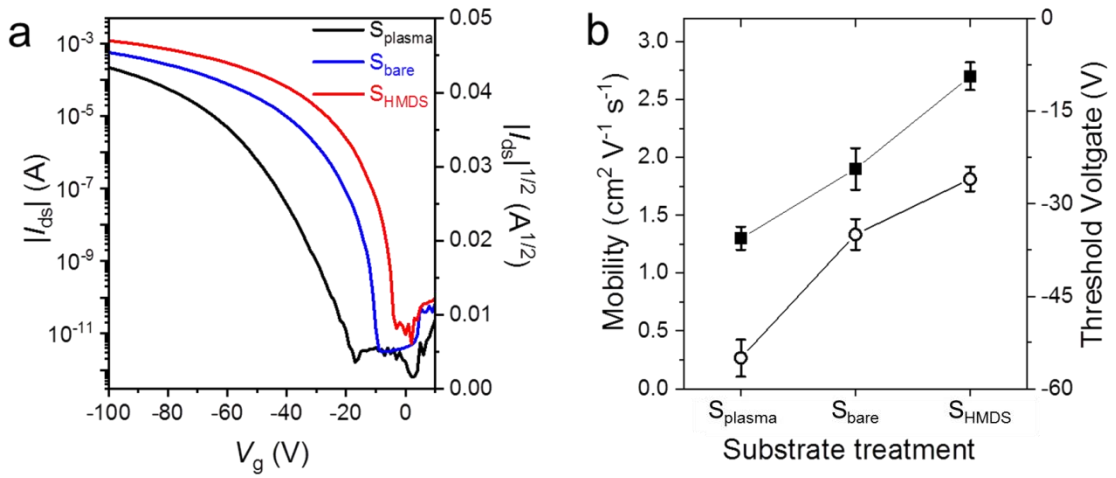

Figure 4.22. (a) Transfer curves at V_{ds} = -100 V for C8-BTBT on different substrates from mixed-solvent at 20 μm/s and $\alpha_{60°}$.

Surface modification can also favor the charge carrier transport in OFETs. The transfer curves in Figure 4.22 reveal that the average mobility rises from 1.5 cm^2 V^{-1} s^{-1} for S_{plasma} to 2.0 cm^2 V^{-1} s^{-1} for S_{bare} and to 2.7 cm^2 V^{-1} s^{-1} for S_{HMDS} when C8-BTBT is dip-coated from a mixed-solvent at 20 μm/s and $\alpha_{60°}$. This improvement in device performance is attributed to the reduction of the surface trap density due to the self-assembled monolayer applied at the interface.[19] The highest mobility of around 3.6 cm^2 V^{-1} s^{-1} is obtained for S_{HMDS} at 20 μm/s and $\alpha_{60°}$. Notably, the small β_{mix} and low solubility mixed-solvent during ADDC significantly assists the crystallization of C8-BTBT and thus improves device performance. It gives inspiration to develop innovative solution deposition techniques and adaptable OSC (electrode) inks towards industrial-scale printing processes.

4.6 Conclusion

In this chapter, I have discussed the crucial role of the meniscus shape on the fluid flow and crystallization of small molecule OSCs by ADDC of C8-BTBT. The meniscus angle is determined the surface tension of solution, surface energy of substrate and substrate tilt angle. During ADDC, the film thickness and coverage ratio of C8-BTBT increases with

substrate tilting. With the increase of tilt angle, the crystalline morphology of C8-BTBT transits from dendritic morphology, to aligned ribbon and to slip-stick morphology. Fluid flow simulation shows that the increased upward flow at small β enlarges the concentration gradient at the meniscus. Therefore, the increased mass deposition of C8-BTBT results from the evaluated concentration gradient yielding raised supersaturation. On the other hand, the coverage ratio and morphology of C8-BTBT are impacted by the surface of energy of substrate. At low surface energy of the substrate the fluid flow assisted crystallization at small meniscus angle is suppressed by an elevated nucleation barrier. At the same time, the fluid flow assisted crystallization also favored by higher supersaturation caused by a lower solubility of C8-BTBT. The resulting aligned film morphologies and higher surface coverage significantly enhance the charge carrier transport in the dip-coated C8-BTBT films.

Reference

1. Y. Diao, L. Shaw, Z. Bao and S.C.B. Mannsfeld, *Energy Environ. Sci.*, 2014, **7**(7): 2145-2159.
2. X. Gu, L. Shaw, K. Gu, M.F. Toney and Z. Bao, *Nat. Commun.*, 2018, **9**(1): 534.
3. G. Qu, J.J. Kwok and Y. Diao, *Acc. Chem. Res.*, 2016, **49**(12): 2756-2764.
4. D. Grosso, *J. Mater. Chem.*, 2011, **21**(43): 17033-17038.

5. R. Janneck, F. Vercesi, P. Heremans, J. Genoe and C. Rolin, *Adv. Mater.*, 2016, **28**(36): 8007-8013.
6. N. J. Arfsten, A. Eberle, J. Otto and A. Reich, *J. Sol-Gel Sci. Technol.*, 1997, **8**(1-3): 1099-1104.
7. A. Filali, L. Khezzar and E. Mitsoulis, *Comput. Fluids*, 2013, **82**: 110-121.
8. K. Zhang, P. Wucher, T. Marszalek, M. Babics, A. Ringk, P.W.M. Blom, P.M. Beaujuge and W. Pisula, *Chem. Mater.*, 2018, **30**(15): 5032-5040.
9. A.M. Tartakovsky, P. Meakin, T.D. Scheibe and R.M. Eichler West, *J. Comput. Phys.*, 2007, **222**(2): 654-672.
10. J. Jang, S. Nam, K. Im, J. Hur, S.N. Cha, J. Kim, H.B. Son, H. Suh, M.A. Loth, J.E. Anthony, J.-J. Park, C.E. Park, J.M. Kim and K. Kim, *Adv. Funct. Mater.*, 2012, **22**(5): 1005-1014.
11. H. Bodiguel, F. Doumenc and B. Guerrier, *Langmuir*, 2010, **26**(13): 10758-63.
12. B.B. Patel and Y. Diao, *Nanotechnology*, 2018, **29**(4): 044004.
13. F. Zhang, E. Mohammadi, X. Luo, J. Strzalka, J. Mei and Y. Diao, *Langmuir*, 2018, **34**(3): 1109-1122.
14. N.T. Thanh, N. Maclean and S. Mahiddine, *Chem. Rev.*, 2014, **114**(15): 7610-7630.
15. S.C. Lim, S.H. Kim, J.H. Lee, M.K. Kim, D.J. Kim and T. Zyung, *Synth. Met.*, 2005, **148**(1): 75-79.
16. J.R. Ray, B. Lee, J. Baltrusaitis and Y.S. Jun, *Environ. Sci. Technol.*, 2012, **46**(24): 13167-13175.
17. Y.S. Jun, D. Kim and C.W. Neil, *Acc. Chem. Res.*, 2016, **49**(9): 1681-1690.
18. S. Kwon, J. Kim, G. Kim, K. Yu, Y.R. Jo, B.J. Kim, J. Kim, H. Kang, B. Park and K. Lee, *Adv. Mater.*, 2015, **27**(43): 6870-6877.
19. L. L. Chua, J. Zaumseil, J. F. Chang, E. C. W. Ou, P. K. H. Ho, H. Sirringhaus and R. H Friend, *Nature*, 2005, **434**(7030): 194.

Chapter 5 Microstructural evolution of small molecule organic semiconductor crystals during meniscus-guided coating

5.1 Introduction

In Chapter 3, the dip-coated DH4T:PMMA and DPP6T:PMMA blends show continuous crystalline thin film morphologies and exhibit comparable charge transport performance. In Chapter 4, the role of meniscus shape on the fluid flow on the crystallization of OSC is discussed. These insights on the viscosity gradient and meniscus shape are important for the scaling-up of printed organic electronics. However, a comprehensive unified understanding of the OSC crystallization mechanism during meniscus-guided coating remains elusive.[1, 2] Especially, various meniscus-guided coating techniques have been developed to obtain aligned crystalline morphologies,[3-5] but only little insight on the origin of alignment and the microstructural evolution has been so far provided.

Combination of experiment and simulation is an efficient route to reveal the origin of alignment and microstructural evolution. During meniscus-guided coating of OSCs, the confinement of OSCs crystallization is imposed in the out-of-plane direction.[6] As for two-dimensional mode, spherulitic crystal growth is a simple and ideal model to understand the crystallization mechanism.[6, 7] However, it is challenging to precisely control the spherulitic morphology. Meanwhile, in order to match the two-dimensional in-plane simulation, the experimental fluid flow and mass transport that in the out-of-plane should be suppressed.

In this chapter, zone-casting of small molecule DPP(Th_2Bn)$_2$ is performed. Spherulitic crystals of DPP(Th_2Bn)$_2$ were obtained by optimizing solution concentration and deposition temperature, whose domain size was governed by zone-casting speed. In the evaporation regime, the crystal sizes increase with the decrease of coating speed. A relatively slow coating

speed lead to aligned morphology. The numerical simulation of the two-dimensional in-plane crystallization demonstrates that the concentration gradient during meniscus-guided coating is governed by the depletion induced by crystal growth and the increase due to solvent evaporation. The aligned morphology at slow coating speed results from the low concentration gradient near the crystalline growth front. This work proves that during meniscus-guided coating the morphological evolution of small molecule OSC crystal is governed by coating speed and concentration gradient. This behavior indicates the formation of crystal morphology and origin of the alignment.

5.2 Zone-casting of DPP($Th_2Bn)_2$

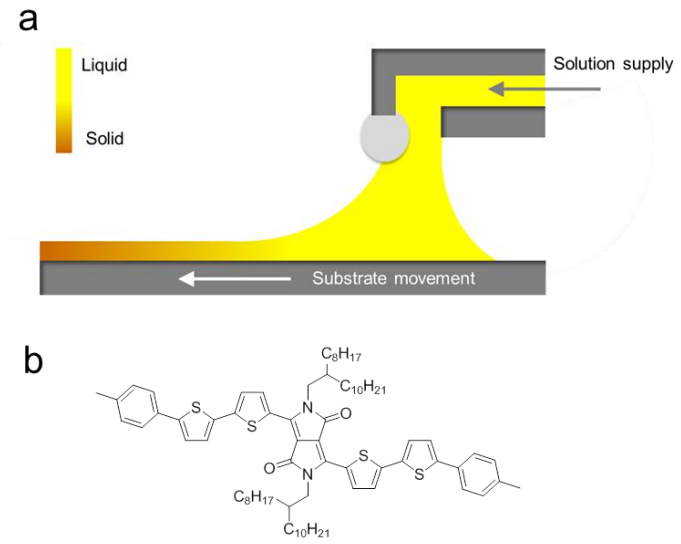

Figure 5.1. (a) Schematic illustration of zone-casting. (b) Molecular structure of DPP($Th_2Bn)_2$.

In order to understand the relation between small molecule OSC crystal growth and coating speed, zone-casting of DPP($Th_2Bn)_2$ was performed as shown in Figure 5.1a. The low-rigid conjugated backbone and long symmetry side chains of DPP($Th_2Bn)_2$ lead to a mediate crystallization ability and wetting property of the DPP($Th_2Bn)_2$/$CHCl_3$ solution. Zone-casting was performed from 3 mg/mL DPP($Th_2Bn)_2$/$CHCl_3$ solution on S_{plasma}. Firstly, zone-casting speeds vary from 50 µm/s to 1000 µm/s and the deposition temperatures are

fixed at 50 °C. The deposition temperature (50 °C) is close to the boiling point of $CHCl_3$ (61.2 °C). In this condition, the equilibrium front evaporation rate (E_{efe}) is expected to above 100 μm/s (this value is from the reported edge-casting evaporation rate).[4] Therefore, the time scale for fluid flow and mass transport in the out-of-plane is expected to be highly suppressed.

As introduced in Chapter 1.4.3, the deposition regime of zone-casting is characterized by the relation between film thickness and coating speed.[8] During zone-casting of DPP(Th$_2$Bn)$_2$, the film thickness obtained at a coating speed of ν (h_v) was measured to reveal the deposition regime. Figure 5.2 shows that the average film thickness $<h_v>$ exhibits an exponential growth with the decrease of coating speed, indicating a typical evaporation regime for these processing parameters.[9] For instance, $<h_{75}>$ is around 600 nm, which is 6 times of $<h_{1000}>$.

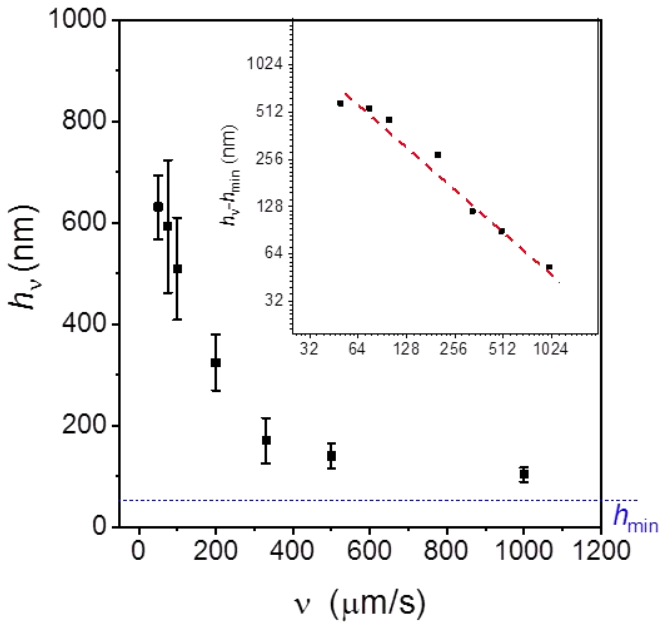

Figure 5.2. Relation between film thickness and coating speed during zone-casting of DPP(Th$_2$B)$_2$. h_{min} indicates the minimum film thickness can be obtained by zone-casting, which simply estimated as $<h_{1000}>/2$.

5.3 Spherulitic crystals of DPP(Th$_2$Bn)$_2$

Morphologies of DPP(Th$_2$Bn)$_2$ films obtained by zone-casting at different coating speeds were inspected by polarized optical microscopy images and atomic force microscopy

images. As shown in Figures 5.3 and 5.4, a continuous crystalline film is composed of densely packed DPP(Th_2Bn)$_2$ spherulites for coating speeds from 75 μm/s to 1000 μm/s. At a fast coating speed at 500 (and 1000) μm/s, polarized optical microscopy and atomic force microscopy images display random spherulitic domains of DPP(Th_2Bn)$_2$ crystal. With the decrease of coating speed, the domain size of DPP(Th_2Bn)$_2$ obviously increases and the random domain gradually turns into anisotropy. When coating speed slows to 75 (and 100) μm/s, DPP(Th_2Bn)$_2$ crystals exhibit a preferred directionality along the zone-casting direction. It is found that the nucleation point of DPP(Th_2Bn)$_2$ appears at the front of crystal domains along coating direction, different with centralized nucleation at 500 (and 1000) μm/s.

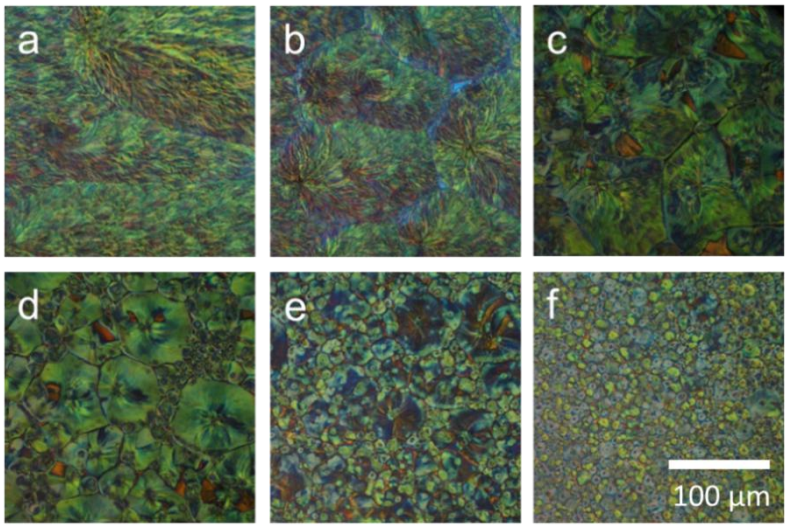

Figure 5.3. Polarized optical microscopy images of zone-cast DPP(Th_2Bn)$_2$ crystals obtained at different coating speed. Scale bare: 100 μm.

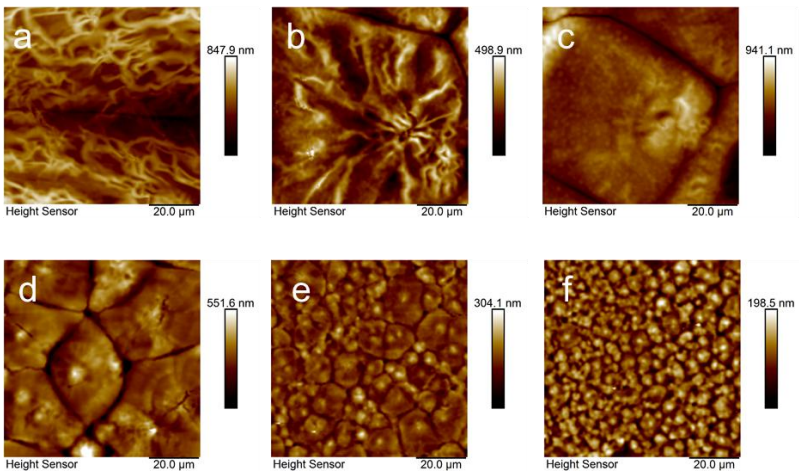

Figure 5.4. Atomic force microscopy images of zone-cast DPP(Th_2Bn)$_2$ crystals obtained at different coating speed.

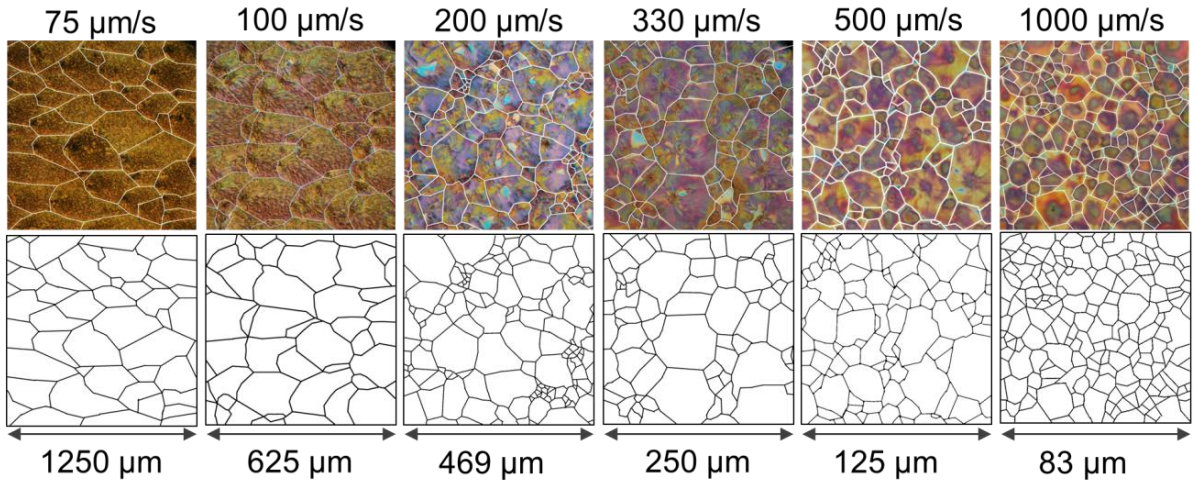

Figure 5.5. Optical microscopy images highlighted domain boundary of DPP(Th_2B)$_2$ crystals obtain by zone-casting and the corresponding extracted domain diagram of DPP(Th_2B)$_2$ crystals for analysis of average domain size.

To determine the relation between domain size (A_v) and coating speed of v, domain boundaries of DPP(Th_2B)$_2$ crystals was identified and highlighted in the optical microscopy images in Figure 5.5. For the calculation of the domain size by Image J, the boundaries were further emphasized and extracted into a domain diagram by Adobe photoshop CS6 (Figure 5.5). As shown in Figure 5.6, relatively small DPP(Th_2Bn)$_2$ crystal sizes ($A_{1000} \approx 30$ µm^2) were obtained at 1000 µm/s. With coating speed decreasing from 1000 µm/s to 75 µm/s, the DPP(Th_2Bn)$_2$ domain size grows exponentially. At a slow coating speed at 75 µm/s, the average film thickness $<A_{75}>$ reaches up to 30,000 µm^2, which is around 1000 times of A_{1000}. The relation between domain size and coating speed indicates that during zone-casting DPP(Th_2Bn)$_2$, the crystal morphology formation is governed by coating speed.

For zone-cast DPP(Th_2Bn)$_2$ films, the dimensions of the film thickness h_v are much lower than the diameter (d_v) of DPP(Th_2Bn)$_2$ crystal domains. This implies that the growth of DPP(Th_2Bn)$_2$ is mainly dominated by a two-dimensional in-plane growth. Though the growth of DPP(Th_2Bn)$_2$ crystals is expected that to be three-dimensional at the initial stage of film formation, the crystal growth transfers into two-dimensional mode when crystal domain sizes

exceeds a crystal film thickness. Since the out-of-plane growth is suppressed owing to the specimen thickness effect.[6, 7]

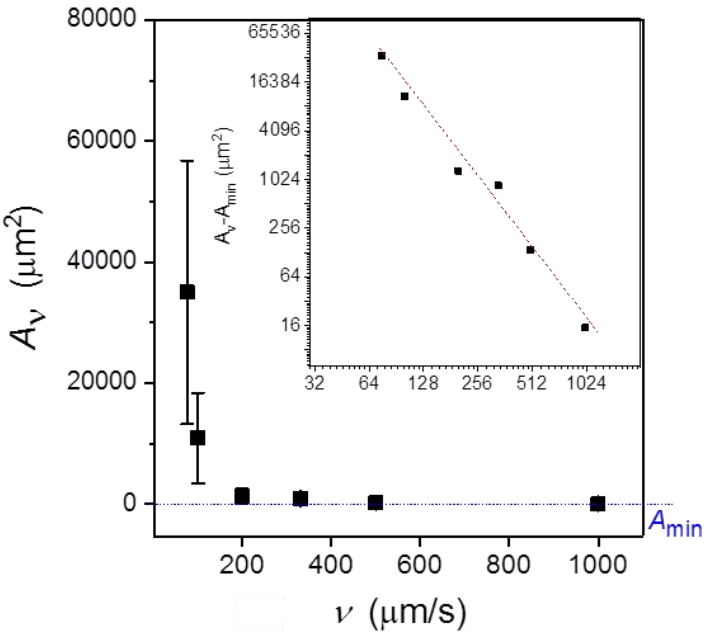

Figure 5.6. Relation between domain size (A_v) and coating speed of v for zone-cast DPP(Th$_2$B)$_2$. A_{min} indicates the minimum film thickness can be obtained by zone-casting, which simply estimated as $<A_{1000}>/2$.

To gain information about the molecular organization of zone-cast DPP(Th$_2$Bn)$_2$ film, GIWAXS was employed. All deposited films have shown an edge-on orientation as indicted by the meridional position of the 100 reflection corresponding to the interlayer distance of 2.10 nm (Figure 5.7). Off meridional position of the reflection assigned to the π-π distance of 0.36 nm suggest tilting of the DPP(Th$_2$Bn)$_2$ molecules under angle of 32° to the substrate. At 1000 μm/s, the DPP(Th$_2$Bn)$_2$ crystals exhibit identical reflection patterns for two measurement directions, perpendicular and parallel to the zone-casting, corresponding to random spherulitic morphology obtained at high deposition speed (Figure 5.7). In contrast, the difference in the diffraction patterns for the two measurement directions DPP(Th$_2$Bn)$_2$ films cast at 75 μm/s proves the structural orientation of the crystal domains induced by the slow coating speed (Figure 5.7).

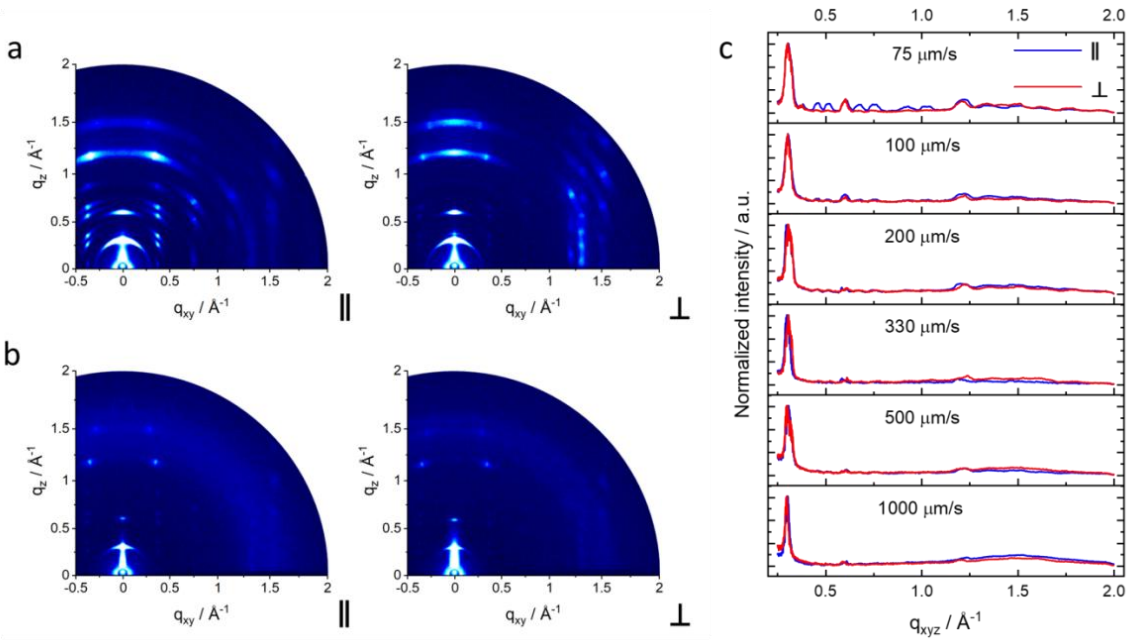

Figure 5.7. GIWAXS patterns of DPP(Th_2B)$_2$ crystals obtain parallel and perpendicular to zone-casting direction (a) at 75 µm/s and (b) at 1000 µm/s. Comparison of full range integration profiles (c) for samples measured parallel and perpendicular to the zone-casting direction. ("∥" and "⊥" represents measurement parallel and perpendicular to coating direction, respectively.)

Though the decrease of zone-casting speed leads to the increase of in-plane domain size of the spherulitic DPP(Th_2Bn)$_2$ crystal, the out-of-plane coherence length decreases with lower coating speed. As shown in Figure 5.8, the coherence length declines almost linearly with decreasing coating speed from 20.6 nm at 1000 µm/s to 11.8 nm at 75 µm/s. The decrease of coherence length is caused by random fluctuations and imperfections in the crystalline lattice which can be quantified by paracrystallinity disorder parameter. As shown in Figure 5.8, the paracrystallinity disorder increases linearly with decreasing casting speed and reaches 15.8% at 75 µm/s while at 1000 µm/s is 12%.[11-13] It is assumed that the formation of paracrystallinity is located between the crystalline domain planes. This may be related to molecules organisation disturbance in the out-of-plane direction. At low coating speed, the crystalline growth is affected by shearing forces and thus high molecule order in the coating direction and in-plane but low order in the out-of-plane. While at high coating

speed the spherulite growth is not forced in any direction and the out-of-plane order is not so strongly hindered.

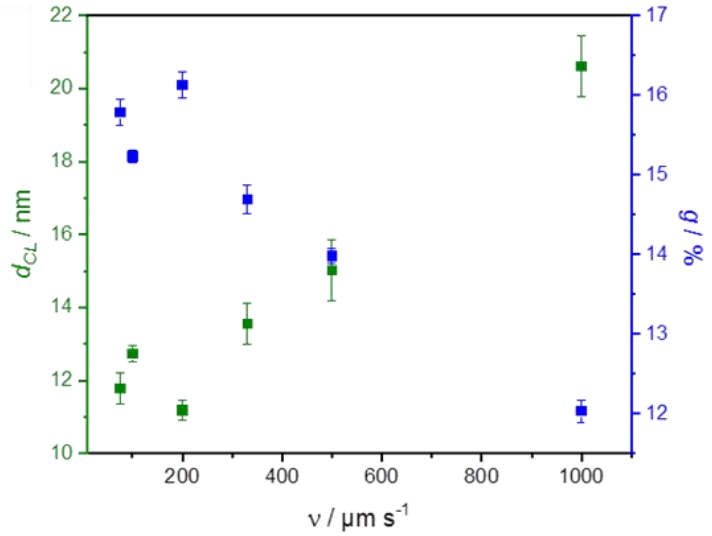

Figure 5.8. Coherence length d_{CL} and paracrystalinity disorder g derived from (100) reflection for different coating speed.

5.4 Aligned crystal of DPP(Th$_2$Bn)$_2$

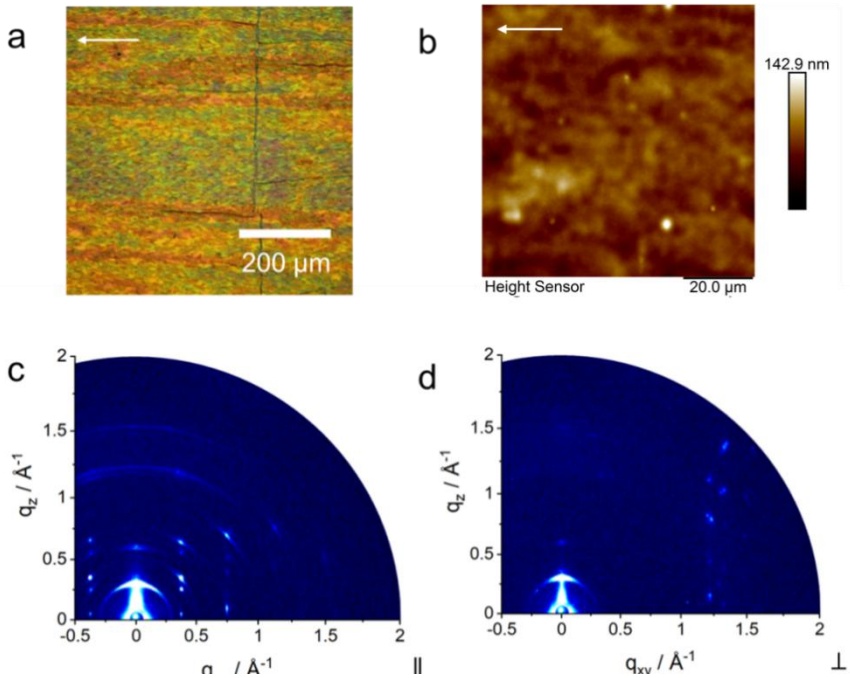

Figure 5.9. (a) Optical microscopy and (b) atomic force microscopy images of DPP(Th$_2$Bn)$_2$ obtained by zone-casting at 50 µm/s. GIWAXS patterns of DPP(Th$_2$B)$_2$ crystals obtain at 50 µm/s (c) parallel and (d) perpendicular to zone-casting direction. White arrow indicates the coating direction. ("∥" and "⊥" represents measurement parallel and perpendicular to coating direction, respectively.)

For a lower zone-casting speed at 50 μm/s, morphologies of DPP(Th$_2$Bn)$_2$ transits from spherulite into aligned morphology (Figure 5.9a). Atomic force microscopy image indicates no obvious large domain boundaries (Figure 5.9b). It indicates that the formation of aligned crystal is determined by zone-casting speed. The GIWAXS patterns show the distinct difference for the two measurement directions, strong reflection at parallel direction but relatively low reflection at perpendicular direction (Figure 5.9d). It indicates the crystal growth of DPP(Th$_2$Bn)$_2$ is aligned, corresponding with the optical microscopy images in Figure 5.9a. Due to the aligned morphology at 50 μm/s, the domain size is not discussed here. The optical microscopy and atomic force microscopy images and GIWAXS patterns proves the coating speed governed crystal morphology and the transition from spherulites to alignment. These behaviors indicate that the nucleation density and position of meniscus-guided OSC crystallization is impacted by coating speed as well as the concentration gradient at the evaporation front.

5.5 Numerical model of crystal growth

As discussed above, the growth of DPP(Th$_2$Bn)$_2$ during zone-casting can be described by two-dimensional in-plane growth. In order to understand the role of zone-casting speed and solvent evaporation on the microstructural evolution, the phase field method [14] in combination with a description for spatially anisotropic solvent evaporation was employed to numerically model the spherulitic crystal growth (Numerical simulation carried by Dr. Jasper J. Michels). This numerical model [15-18] is based on two types of order parameter fields, a conserved one, denoted ϕ, representing local volume fraction and a non-conserved one, denoted η, representing the local crystallinity. Both parameters smoothly vary between 0 (zero concentration/amorphous) and 1 (pure solute/crystalline). In this model, the N-phase formalism ($\eta_1,\eta_2,...,\eta_N$) was used to account for grain impingement due to mismatch in

crystalline orientation. The set of coupled dynamic equations governing mass transport (Cahn-Hilliard) and phase transition (Allen-Cahn) reads as follows:

$$\frac{\partial \phi(\mathbf{r},t)}{\partial t} = \nabla \cdot \Lambda_{\phi\phi} \frac{\delta F}{\delta \phi} + \theta_{\phi}(\mathbf{r},t) + \sigma(\mathbf{r},t) \qquad \text{(Equation 5.1)}$$

$$\frac{\partial \eta_i(\mathbf{r},t)}{\partial t} = \Gamma_{\eta} \frac{\delta F}{\delta \eta_i} + \theta_{\eta_i}(\mathbf{r},t) \qquad \text{(Equation 5.2)}$$

where $\mathcal{F}$ is the total free energy of the system composed of local and non-local contributions. $\Lambda_{\phi\phi}$ and Γ_{η} respectively represent a mobility coefficient based on mutual diffusivity[19] and a kinetic coefficient assuming crystal growth to be limited by diffusion of solute from the solution towards the liquid-solid interface. The terms θ_{ϕ} and θ_{η_i} represent thermal fluctuations in the conserved and non-conserved order parameter fields, and σ the local (concentration-dependent) evaporative flux.

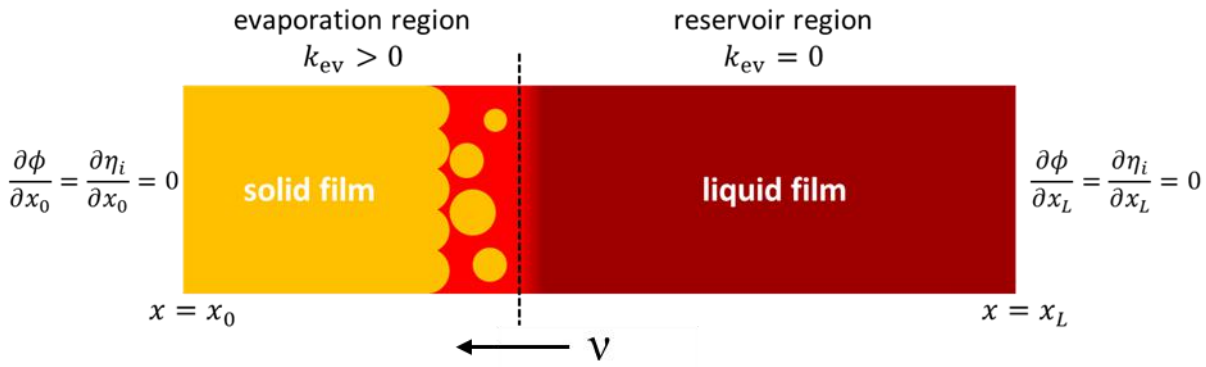

Figure 5.10. Schematic illustration of the computational domain. The solid film, crystallization front and bulk solution are respectively indicated in orange, red and dark red. The dotted black line represents the "evaporation border", left (right) of which a positive constant (zero) solvent mass transfer coefficient (k_{ev}) applies. During the simulation run, the evaporation border is translated at a constant speed v. No-flux boundary conditions for order parameters ϕ and η_i apply at $x = x_0$ and $x = x_L$. Periodic boundary conditions apply at the y-extremes.

The simulated solute-solvent system was assumed to be incompressible ($\phi_{solute} + \phi_{solvent} = 1$) and impose $\sum_{i=1}^{N} \eta_i = 1$ for the phase fields. In order to identify the regimes and regions in the liquid where we deem our model to be valid, there are three main assumptions and simplifications including: (1) material transport is treated in a purely diffusive manner; (2)

two dimensional in-plane space dimensions, which neglects composition and order parameter gradients in the z-direction; (3) heat dissipation (*e.g.* heat of crystallization) is fast in comparison to material transport and crystal growth.

The computational domain of the zone-coating process is shown in Figure 5.10. An "evaporation" and a "reservoir" region, respectively indicated by the orange/red and dark red regions. The former grows linearly in time at the expense of the latter by translating an "evaporation border" (dashed black line) across the domain at a constant speed ν. The red area represents solution with increased solute concentration, whereas the orange areas represent crystallized (solidified) solute. In the evaporation region the evaporative mass transfer coefficient k_{ev} is assigned a positive constant value, whereas in the reservoir region it is set to zero ($k_{\mathrm{ev}} \sim v^n$ and $n > 1$). This way, the evaporation region is subject to irreversible evaporative mass-loss, whereas in the reservoir region the effect of evaporation is negligible owing to replenishment. The solute concentration in the reservoir region is not necessarily the same as the experimental initial concentration in the solution. In contrast, in the evaporation regime the reservoir concentration may in fact be a steady state value achieved at some small distance upstream from the solidification front.

Exemplary numerical simulations of spherulitic crystal growth during zone-casting at different coating speeds are shown in Figure 5.11. One of the most striking results is that for a given solvent evaporation rate, a critical coating speed exists, below which the crystalline morphology changes from an impinged shperulitic morphology (as exemplified by Figures 5.11a and b) to an aligned morphology (Figure 5.11c). Near this transition, the size of the spherulites increases as they become stretched parallel to the coating direction, their nucleation points becoming off-centered (Figure 5.11 b). These computational results agree very well with the morphological evolution of DPP(Th_2Bn)$_2$ crystal growth during zone-casting (Figures 5.3 and 5.9a).

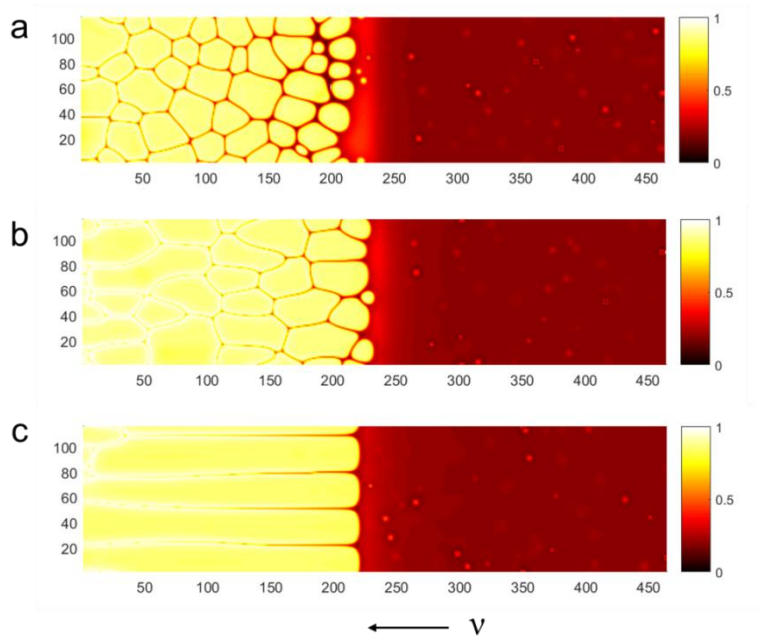

Figure 5.11. Numerical simulation of spherulitic crystal growth during zone-casting at (a) fast, (b) mediate and (c) slow speeds and comparable rate of evaporation. Length and time scales in these simulations are non-dimensionalized.

An explanation of the observed phenomena is given in the solute concentration profiles (ϕ_{solute}) as shown in Figure 5.12a,b. The images (exemplified in Figure 5.12c,d) clearly reveal the concentration gradient (ϕ_{solute}) that precedes the crystalline region. $\phi_{\text{nucleation}}$ is the critical concentration that allows the occurrence of nucleation. A maximum concentration develops owing to the combined effect of an increase in concentration due to solvent evaporation and a decrease in concentration due to depletion near the crystalline growth front. In the impingement regime, the coating speed is fast in comparison to the depletion. The ongoing solvent evaporation drives the maximum concentration into the super-saturated regime exceed the critical concentration ($\phi_{\text{solute}} > \phi_{\text{nucleation}}$) .This allows the successful nucleation to occur in front of the initial growing crystal domains, giving rise to a spherulitic crystalline morphology (Figure 5.12a,c). In contrast, in the alignment regime, the maximum concentration remains below the critical concentration ($\phi_{\text{solute}} < \phi_{\text{nucleation}}$). As a result, the insufficient maximum concentration only contribute the growth of the initial crystal domains and thus leads to aligned morphology (Figure 5.12b,d).

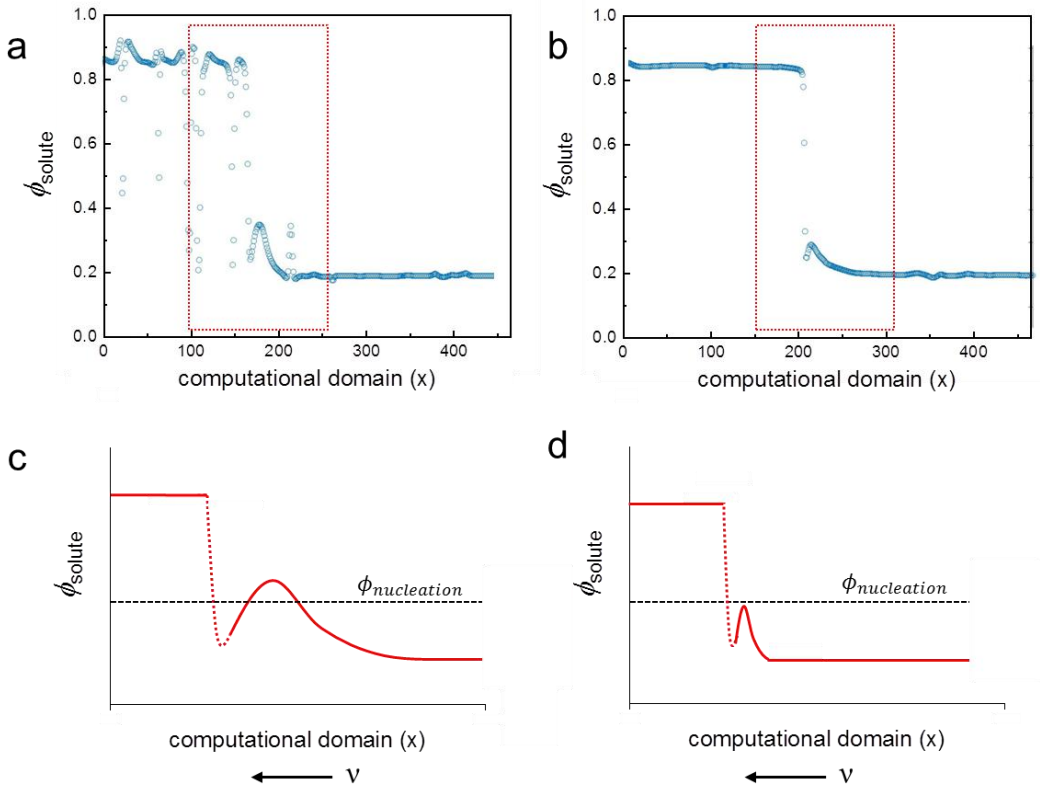

Figure 5.12. Computational ϕ_{solute} and corresponding schematic illustration along coating direction at (a,c) fast speed and (b,d) slow speed.

As discussed above, the fluid flow and meniscus shape are not considered in this simulation. This numerical model focuses on understanding the impact of coating speed and solvent evaporation on the crystal growth. It indicates that during zone-casting of DPP(Th_2Bn)$_2$ at 50 °C (from $CHCl_3$), the crystal growth at is governed by the interplay between solvent evaporation and coating speed.

In this work, the crystallization simulation reveals that crystal growth induces a depletion of solute at the crystalline growth front. It is a strong supplement for the fluid flow simulation in Chapter 4. Since the small vial was used during ADDC of C8-BTBT to suppress solvent evaporation and focus on fluid flow without considering the solidification into the fluid flow simulation. As for zone-casting of DPP(Th_2Bn)$_2$, the high evaporation rate is employed to reduce the out-of-plane flow. It gives an in-plane concentration gradient influenced by crystal growth and solvent evaporation.

Therefore, during meniscus-guided coating, the formation of concentration gradient in the meniscus is a collective effect of the concentration accumulation owing to solvent evaporation and fluid flow and depletion induced by crystal growth.

5.6 OFETs

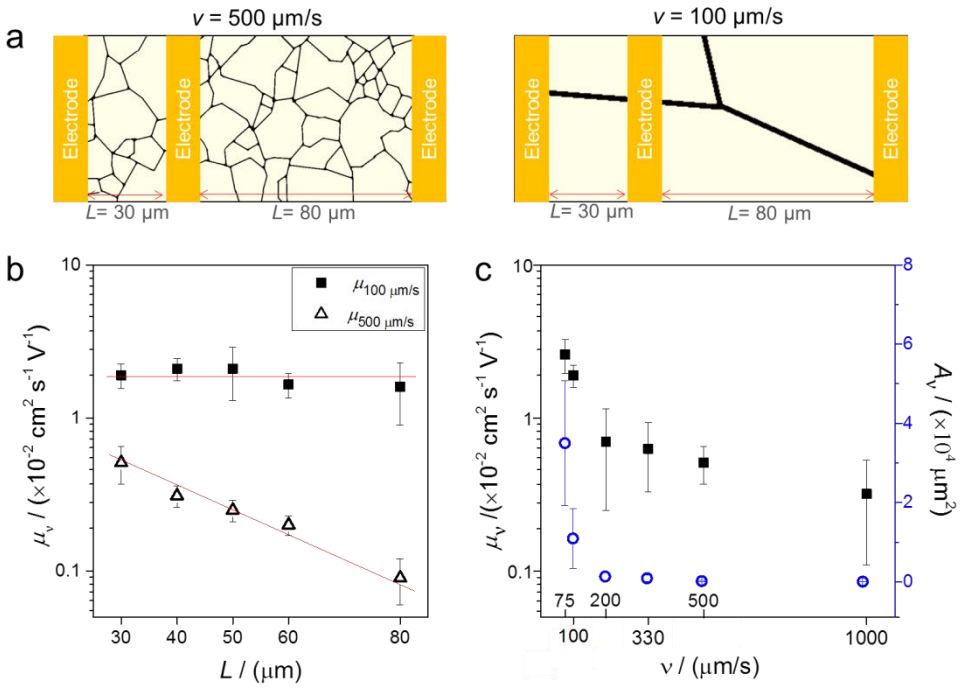

Figure 5.13. (a) Illustration of domain boundaries between source and drain electrodes for DPP(Th$_2$Bn)$_2$ films zone-cast at two different speeds. (b) Mobility μ_v of DPP(Th$_2$Bn)$_2$ films zone-cast at 100 μm/s and 500 μm/s as a function of Channel length *L*. (c) Mobility μ_v of DPP(Th$_2$Bn)$_2$ films zone-cast at 100 μm/s as a function of coating speed.

As discussed in Chaper 1.4.3, the charge carrier transport performance of thin film transistors is influenced by the film morphology. Therefore, in order to reveal the influence of domain size and structural directionality of zone-cast DPP(Th$_2$Bn)$_2$ on the charge carrier mobility (μ_v), BGTC configuration transistors based on DPP(Th$_2$Bn)$_2$ were fabricated. The BGTC configuration can avoid the influence of the bottom electrodes on the crystal growth of OSCs, whereby it leads to an underestimated μ_v induced by bulk traps for thick films,[20, 21] since the effective pathway for carriers in transistor is the first few layers.[22, 23]

In the case of the zone-cast speed of 500 µm/s, DPP(Th$_2$Bn)$_2$ crystals exhibit small domains whose diameter d_{500} is smaller than channel length (L) (Figure 5.13a). The relation between μ_v and L is shown in Figure 5.13b and 5.14. For transistors with $L_{30\mu m}$, $\mu_{500\mu m/s}$ is around 5.1 × 10^{-3} cm^2 s^{-1} V^{-1}, with an on/off ration of 5x10^3 (Figure 5.14a). With the increase of L, $\mu_{500\mu m/s}$ gradually decreases. Thereby, $L_{80\mu m}$ leads to the lowest mobility around 0.9 × 10^{-3} cm^2 s^{-1} V^{-1}. The L-dependent behavior of $\mu_{500\mu m/s}$ is induced by the small domain size. As shown in Figure 5.13a, the number of domain boundaries between source and drain electrodes will greatly increases when L is increased from 30 µm to 80 µm. In contrast, $\mu_{100\mu m/s}$ remains unchanged at 1.6 - 2.1 × 10^{-2} cm^2 s^{-1} V^{-1} for L varying from 30 µm to 80 µm, exhibiting L-independent behavior (Figures 5.13a and 5.14c). The constant $\mu_{100\mu m/s}$ arises from the large domains that are comparable to or longer than L (Figure 5.13a).

Figure 5.13c presents the relation of μ_v and coating speed of ν for zone-cast DPP(Th$_2$Bn)$_2$ crystals based on transistor with $L_{30\mu m}$. When coating speed decreases from 1000 µm/s to 200 µm/s, μ_v slightly increase from 0.3 × 10^{-2} cm^2 s^{-1} V^{-1} to 0.7 × 10^{-2} cm^2 s^{-1} V^{-1}. Lowering the speed further to 100 and 75 µm/s, $\mu_{100\mu m/s}$ and $\mu_{75\mu m/s}$ increase to 1.9 × 10^{-2} cm^2 s^{-1} V^{-1} and 2.7 × 10^{-2} cm^2 s^{-1} V^{-1}, respectively (Figures 5.13c and 5.14e). The output curve indicates serious contact resistance for DPP(Th$_2$Bn)$_2$ cast at 100 and 75 µm/s (Figure 5.14d,f).[24] This can be related to the bulk traps and bulk resistance of BGTC devices for thicker film and the rough semiconductor/electrode interface for large DPP(Th$_2$Bn)$_2$ domains.[21] The overall upward trend of μ_v mainly follows the increase of A_v (Figure 5.13c). The larger domain size and preferred directionality dominate the charge carrier transport of DPP(Th$_2$Bn)$_2$ crystals as evident for $\mu_{75\mu m/s}$ around 9 times higher than $\mu_{1000\mu m/s}$.[13]

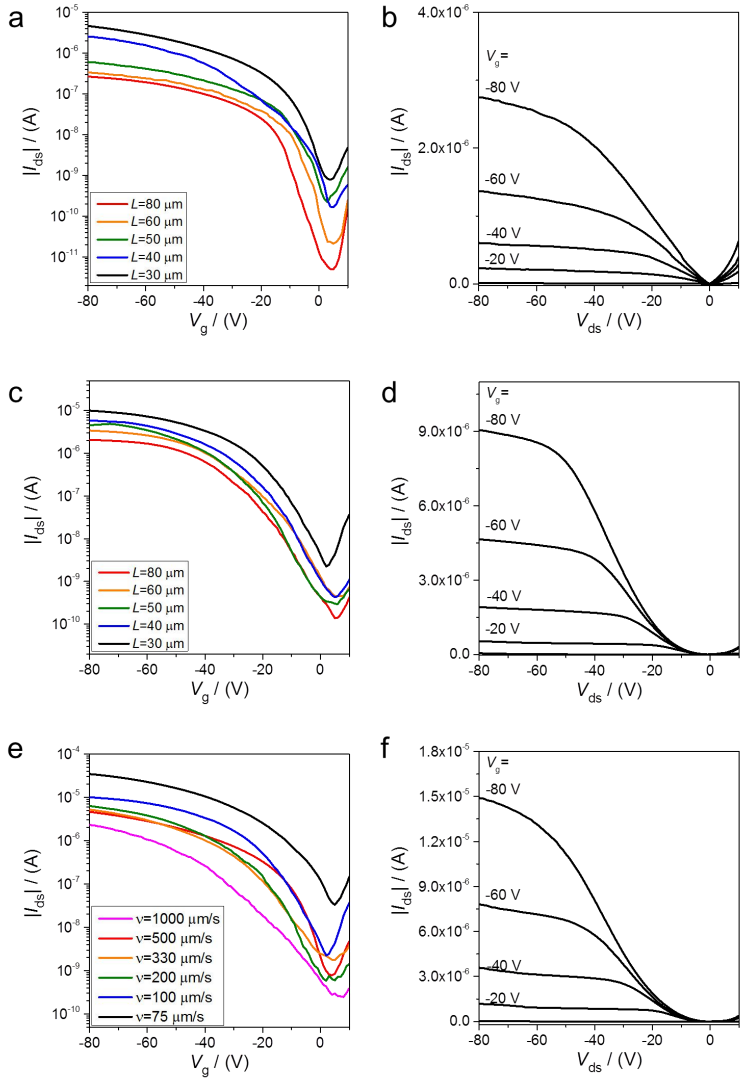

Figure 5.14. Transfer curves of DPP(Th$_2$B)$_2$ obtained at (a) 500 µm/s and (c) 100 µm/s with different *L*. (e) Transfer curves of DPP(Th$_2$B)$_2$ obtained at different coating speed for $L_{30µm}$. Output curves of DPP(Th$_2$B)$_2$ crystals obtained at (b) 500 µm/s (d) 100 µm/s and (f) 75 µm/s for $L_{30µm}$.

At low zone-casting speed of 50 µm/s, the aligned films yield a mobility $\mu_{50µm/s}$ of about 0.1 cm^2 s^{-1} V^{-1}, which is higher than the mobility of spheruliteic DPP(Th$_2$Bn)$_2$. The corresponding transfer and output curves are shown in Figure 5.15. Since I focused on the correlation between coating speed and crystal growth during meniscus guided coating, the optimization of the thickness of the aligned morphology is out of this topic. The electronic performance of zone-cast DPP(Th$_2$Bn)$_2$ films from 50 µm/s to 1000 µm/s demonstrates that

domain boundaries impede the hole transport in OFETs and directional or aligned morphology leads to high mobility.

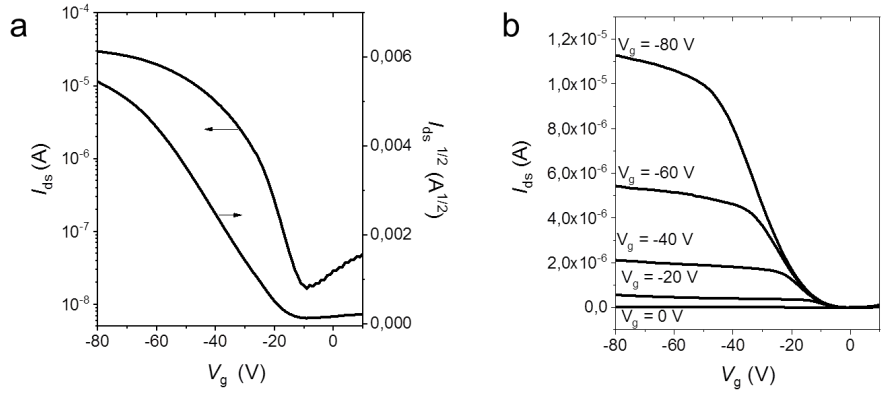

Figure 5.15. (a) Transfer and (b) output curves of FETs based on aligned DPP(Th_2Bn)$_2$ obtained by zone-casting at 50 μm/s.

5.7 Conclusion

In this chapter, a comprehensive understanding of OSCs crystallization during meniscus-guided coating was established by revealing the morphological evolution of zone-cast DPP(Th_2Bn)$_2$. During Zone-casting of DPP(Th_2Bn)$_2$, the domain size and morphology of spherulitic crystal are governed by coating speed. In the evaporation regime, both domain size and film thickness of the spherulitic DPP(Th_2Bn)$_2$ elevate with the decrease of coating speed. Random spherulites of DPP(Th_2Bn)$_2$ form at a fast coating speed. With the decrease of coating speed, a distinct growth front uniaxially orients the spherulites in the coating direction. At a relatively slow coating speed of 50 μm/s, the aligned morphology of DPP(Th_2Bn)$_2$ is formed. The numerical simulation reveals that the morphological during zone-casting is governed by the concentration gradient influenced by coating speed. The formation of concentration gradient is attributed to the depletion induced by crystal growth and the increase due to solvent evaporation. During zone-casting of DPP(Th_2Bn)$_2$, fast coating speed leads to the nucleation in the front of the crystalline growth front and thus leads to spherulites. In

contrast, crystal growth depletes more solute at slow coating speed and leads to a concentration gradient lower than the critical concentration for nucleation. In this way, the insufficient saturation only contributes to crystal growth and thus forms aligned morphology. GIWAXS results confirm the directionality of DPP($Th_2Bn)_2$ structures obtained at slow coating speed. In transistors, the large domain size and preferred directionality ensure a high charge transport.

Reference

1. X. Gu, L. Shaw, K. Gu, M.F. Toney and Z. Bao, *Nat. Commun.*, 2018, **9**(1): 534.
2. Y. Diao, L. Shaw, Z. Bao and S.C.B. Mannsfeld, *Energy Environ. Sci.*, 2014, **7**(7): 2145-2159.
3. W. Deng, X. Zhang, H. Dong, J. Jie, X. Xu, J. Liu, L. He, L. Xu, W. Hu and X. Zhang, *Mater. Today*, 2018.
4. R. Janneck, F. Vercesi, P. Heremans, J. Genoe and C. Rolin, *Adv. Mater.*, 2016, **28**(36): 8007-8013.
5. D.R. Ceratti, B. Louis, X. Paquez, M. Faustini and D. Grosso, *Adv. Mater.*, 2015, **27**(34): 4958-4962.
6. B.B. Patel and Y. Diao, *Nanotechnology*, 2018, **29**(4): 044004.
7. M. He, B. Li, X. Cui, B. Jiang, Y. He, Y. Chen, D. O'Neil, P. Szymanski, M.A. Ei-Sayed, J. Huang and Z. Lin, *Nat. Commun.*, 2017, **8**: 16045.
8. D. Grosso, *J. Mater. Chem.*, 2011, **21**(43): 17033-17038.
9. G. Qu, J.J. Kwok and Y. Diao, *Acc. Chem. Res.*, 2016, **49**(12): 2756-2764.
10. M. L, Berre, Y. Chen and D. Baigl, *Langmuir*, 2009, **25**(5): 2554-2557.
11. J. Rivnay, S.C. Mannsfeld, C.E. Miller, A. Salleo and M.F. Toney, *Chem. Rev.*, 2012, **112**(10): 5488-5519.
12. R. Noriega, J. Rivnay, K. Vandewal, F.P. Koch, N. Stingelin, P. Smith, M.F. Toney and A. Salleo, *Nat. Mater.*, 2013, **12**(11): 1038-1044.
13. J. Rivnay, L.H. Jimison, J.E. Northrup, M.F. Toney, R. Noriega, S. Lu, T.J. Marks, A. Facchetti and A. Salleo, *Nat. Mater.*, 2009, **8**(12): 952-958.
14. N. Provatas and E. Ken, *Phase-field methods in materials science and engineering*, John Wiley & Sons, 2011.
15. J. J. Michels and E. Moons, *Macromolecules*, 2013, **46**(21): 8693-8701.
16. C. Schaefer, P. van der Schoot and J. J. Michels, *Phys. Rev. E,* 2015, **91**(2): 022602.
17. C. Schaefer, J. J. Michels and P. van der Schoot, *Macromolecules* 2016, **49**(18): 6858-6870.
18. H. S. Dehsari, J. J. Michels and K.Asadi, *J. Mater. Chem. C*, 2017, **5**(40): 10490-10497.
19. W. W. Mullins, *Acta Metall.*, 1958, **6**(6): 414-427.
20. D. Gupta and Y. Hong, *Org. Electron.*, 2010, **11**(1): 127-136.
21. J. Dong, P. Yu, S.A. Arabi, J. Wang, J. He and C. Jiang, *Nanotechnology*, 2016, **27**(27): 275202.

22. F. Dinelli, M. Murgia, P. Levy, M. Cavallini, F. Biscarini and D.M. de Leeuw, *Phys Rev Lett*, 2004, **92**(11): 116802.
23. M. Li, D.K. Mangalore, J. Zhao, J.H. Carpenter, H. Yan, H. Ade, H. Yan, K. Mullen, P.W.M. Blom, W. Pisula, D.M. de Leeuw and K. Asadi, *Nat. Commun.*, 2018, **9**(1): 451.
24. C. Liu, Y. Xu and Y.-Y. Noh, *Mater. Today*, 2015, **18**(2): 79-96.

Chapter 6 Conclusions

In this thesis, solvent vapor enhanced drop-casting (SVED) and meniscus-guided coating have been employed to deposit organic semiconductor (OSC) thin films for electronic applications. In order to precisely control the microstructural evolution of OSCs, molecular structure and deposition parameters including solvent selection, polymer binder, meniscus shape and coating speed, were modulated. The study of their correlations allowed to exploit the crystallization mechanism of OSCs during solution processing. The role of these factors on fluid flow, concentration gradient and film growth are summarized as follows:

1. To reveal the influence of conjugation length of donor-acceptor small molecule OSCs on the self-assembly and charge carrier transport, SVED has been employed to control the self-assembly as presented in Chapter 2. On one hand, the extension of the π-conjugation length of donor-acceptor molecules (pyrene-functionalized diketopyrrolopyrrole, pyrene-DPP analogues) has a significant impact on their HOMO/LUMO levels and resulting bandgaps. Especially, the incremental extension of the π-conjugation length in pyrene-DPP analogues leads to the transition from unipolar to ambipolar OFET characteristics, paving the way to a general rational design approach towards achieving solution-processable small-molecule ambipolar OFETs, with high balanced hole and electron mobilities. On the other hand, more extended pyrene-DPP analogues tend to form smaller crystal sizes. The decreased self-assembly ability results from the extension of conjugation length and the increased number of alkyl side-chains involved in the DPP core.

Additionally, the self-assembly also depends on the nature of the solvent used in the SVED protocols. One-dimensional fibers of pyrene-DPP analogues are prone to form in THF, attributed to the reduced solubility and strong π-π stacking interactions. However, the one dimensional fibers of pyrene-DPP analogues show random orientation and large grain boundary, impeding the charge carrier transport.

2. In order to achieve large area, aligned crystalline OSC film growth to enhance the charge carrier transport in transistors, a minor amount of an insulating amorphous polymer binder has been blended with small molecule OSCs during dip-coating. Chapter 3 describes the impact of polymer binder on the OSC crystallization during meniscus-guided coating. In contrast to spin-coating and drop-casting of an OSC:polymer blend, the dip-coated OSC:polymer blend shows a continuous alignment of the crystalline films with stratified OSCs/polymer layers.

The improved crystallization is attributed to the increased mass transport owing to the formation of viscosity gradient at the meniscus. This study provides an understanding on the crystallization mechanism of small molecule OSCs in the presence of a polymer binder during meniscus-guided coating. This efficient and convenient methodology is broadly applicable to various soluble crystalline organic semiconductors, since misaligned crystalline grains and morphological defects are commonly encountered problems during the coating processes of small molecules.

3. In Chapter 3, a new method, termed as angle dependent dip-coating, is proposed to deposit large area, aligned crystalline OSC films. This method is based on the modulation of the meniscus shape (described by the meniscus angle) by substrate tilting, wherein a large tilt angle leads to a narrow meniscus shape. Through combined simulation and experiment, it is found that the increased mass deposition of OSCs during angle dependent dip-coating is attributed to the narrow meniscus shape and increased evaporation rate. In particular, the narrow meniscus shape results in an elevated upward fluid flow enlarging the concentration-gradient at the meniscus and hence yielding raised supersaturation. Therefore, control of the meniscus shape is a convenient and efficient way to modulate the crystallization of OSCs for improving their film deposition.

More importantly, the fluid flow assisted crystallization effect during angle dependent dip-coating is greatly influenced by the surface energy of the substrate. Despite of a narrow

meniscus shape, OSC crystallization is difficult to achieve on substrates with low surface energy due to the high nucleation barrier. However, a mixed solvent with low solubility supports the OSC growth on the substrate with mediate surface energy, owing to the elevated supersaturation. This is another important aspect since the development of inks and substrate treatments is also crucial for scaling-up solution processing of OSCs towards practical applications.

4. In order to understand the microstructural evolution and the origin of aligned morphologies of small molecule OSCs during meniscus-guided coating, zone-casting of DPP(Th_2Bn)$_2$ was performed and described in Chapter 5. The spherulitic domain size of DPP(Th_2Bn)$_2$ was controlled by the zone-casting speed, whereby a low coating speed leads to large domains and directional growth of the OSC. At a relatively slow coating speed, the spherulitic crystal transits into an aligned morphology.

Numerical simulations of the two-dimensional in-plane crystallization demonstrate that a slow coating speed leads to a low concentration gradient that impedes the additional nucleation and thus results in an aligned morphology. The concentration gradient in the meniscus is a combined effect of crystal growth and solvent evaporation as well as the fluid flow, as described in Chapter 4. At slow coating speed, a low concentration gradient forms in the meniscus, owing to the strong solute depletion induced by crystal growth but insufficient increase caused by solvent evaporation. In this way, no additional nucleation occurs in the front of initial growing crystal domains and an aligned morphology forms at slow coating speed. Therefore, the morphological evolution of small molecule OSCs during meniscus-guided coating is governed by zone-casting speed and concentration gradient. Transistors based on small molecule OSCs crystalline film prove that the large domain size and preferred directionality contribute to efficient charge transport.

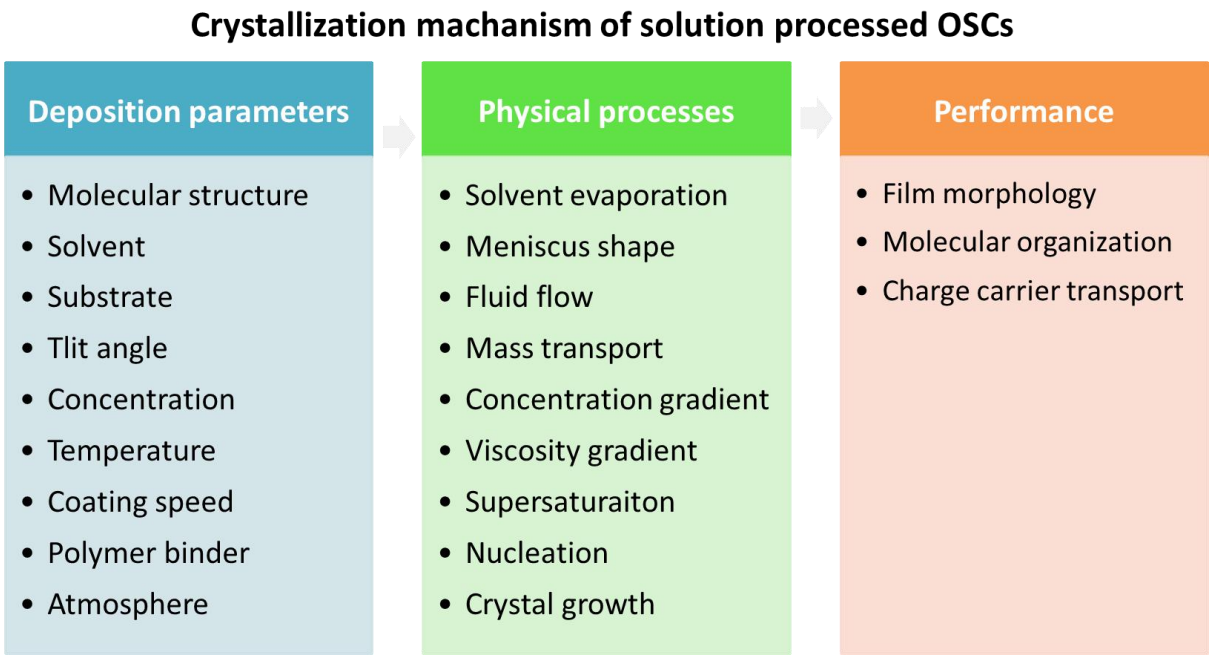

Figure 6.1. Crystallization mechanism of solution processed OSCs

This thesis has revealed the morphological formation of pyrene-DPP analogues by SVED and the crystallization mechanism of small molecule OSCs during meniscus-guided coating. These findings provide a novel insight on the correlation between the deposition parameters, physical processes, and the microstructure of OSCs as well as their electronic performance, as shown in Figure 6.1. It can be expected that understanding the physical processes during solution processing will favor the development of energy-efficient production of low-cost, high-performance electronic devices.

Nevertheless, a full understanding of the solution processed OSC growth still remains elusive. For instance, conjugated polymer OSCs show advantages on the fabrication of flexible device, both the need to clarify their microstructural evolution and crystallization mechanism is significant. Molecular dopants improve the conductivity and mobility of OSCs, but it is challenging to modulate the doping efficiency by solution processing. Revealing the phase separation processes between molecular dopants and active OSCs is expected to provide new insight on controlling the distribution of molecular dopant in these blend systems. Up to now, the deposition of highly aligned conjugated polymer OSCs and solution processed

multilayer architecture are still challenging but important for the development of flexible printed electronics.

Chapter 7 Experimental appendix

7.1 Substrate preparation

The heavily doped n-type Si wafers with a 300 nm thick SiO_2 layer were adopted as substrate. These substrates were cleaned by 20 min ultrasonication in acetone and subsequent 20 min ultrasonication in isopropyl alcohol. In this thesis, the substrate treatment method includes oxygen plasma, HMDS and OTS modification. For S_{plasma}, silicon wafer substrates were treated by an oxygen plasma for 3 min. For S_{HMDS} and S_{OTS}, silicon wafer substrates with a 300 nm thick SiO_2 layer were treated with HMDS or OTS at 150 °C for 6 h to form a self-assembled monolayer.

7.2 Solution processing

7.2.1 Solvent vapor enhanced drop-casting

SVED is an efficient method to tune solvent evaporation rate for controlling the self-assembly behavior and reduction of the dewetting effect for improved film formation ability.[1] During SVED in the laboratory, 0.15 mL of OSC solution is drop-cast on a S_{HMDS} (1.5 × 2 cm^2), which is exposed to saturated solvent vapor in a container with a covered lid (nearly airtight). The container volume of 40 mL contained 3 mL of solvent. The boiling point of the selected solvent will influence the evaporation rate. In Chapter 2, $CHCl_3$ and THF are selected as solvent and the **SM1-3** concentration is 2 mg/mL.

7.2.2 Dip-coating of OSC:polymer blend

Dip-coating is a low-cost and waste-free process to prepare OSC films for electronic applications.[2] During dip-coating, the substrate is immersed into the OSC solution and then withdrawn at a constant speed. Dip-coating of OSC:polymer blends was developed to

improve the film formation of OSC to gain large area, continuous, and aligned crystalline morphology.

In Chapter 3, dip-coating of the pure compounds and blends was performed on S_{plasma}. The dip-coating was performed at coating speeds of 5 µm/s, 10 µm/s and 20 µm/s from $CHCl_3$ solution at concentrations of 3 mg/mL for DH4T and DPP6T. The vial volume was 9 mL and the solution volume was 3 mL.

7.2.3 Angle dependent dip-coating

Angle dependent dip-coating is a further development of the traditional dip-coating method. Angle dependent dip-coating was achieved by tilting the substrate with respect to the solvent bath, allowing a precise control of the meniscus shape. In Chapter 4, angle-dependent dip-coating of C8-BTBT was performed from a $CHCl_3$ or $CHCl_3$:hexane solution at a concentration of 3 mg/mL. The dip-coating speeds ranged from 10 µm/s to 1000 µm/s, and the substrate tilt angles were tuned from 0° to 75° in ambient atmosphere. The vial volume is 15ml and the solvent volume is 4 mg/mL. Bare Si/SiO_2 substrates were treated by oxygen plasma, HMDS or OTS self-assembled monolayer modification to modulate substrate surface energy.

7.2.4 Zone-casting

Zone-casting is a meniscus-guided coating technique to deposit OSC films from OSC solution on a moving substrate.[3] This technique allows controlling the coating speed, solution and substrate temperature. In Chapter 5, zone-casting was performed from 3 mg/mL $DPP(Th_2Bn)_2/CHCl_3$ solution on S_{plasma} with varying coating speeds from 50 µm/s to 1000 µm/s. During zone-casting, the solution and substrate temperatures were 50 °C.

7.3 Characterizations

7.3.1 Contact angle and meniscus angle

The contact angle (θ) is the angle between a drop of liquid and the substrate formed at the gas–liquid–solid interface (Figure 7.1a). The contact angle is determined by the Young's equation as follows:

$$\gamma_{LV}\cos\theta + \gamma_{SL} = \gamma_{SV} \qquad \text{(Equation 7.1)}$$

wherein γ_{SV} represents the solid–vapor interfacial tension, γ_{SL} is the solid–liquid interfacial tension, and γ_{LV} is the liquid–vapor interfacial tension.[4] The meniscus angle is not only influenced by the surface tension of the solvent and the surface energy of the substrate, but also depends on the substrate tilt angle (α) during dip-coating. Contact angle and meniscus angle measurements were performed with a contact angle meter, Data Physics, OCA35 (Figure 7.1b).

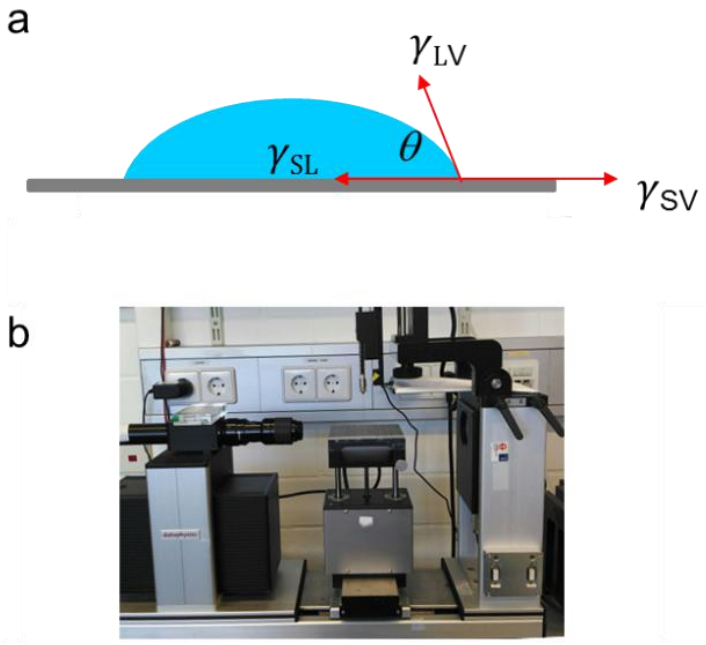

Figure 7.1. (a) Schematic illustration of contact angle. (b) Contact angle meter, Data Physics, OCA35.

7.3.2 Solution viscosity

In Chapter 3, the solution viscosities were obtained by a standard Ostwald capillary viscometer. The capillary or Ostwald viscometer is a common viscometer. The principle is simple: measurement of the time for a volume of liquid (solution or solvent) to flow through the capillary in the vertically aligned viscometer.

7.3.3 UV-vis-NIR spectrum

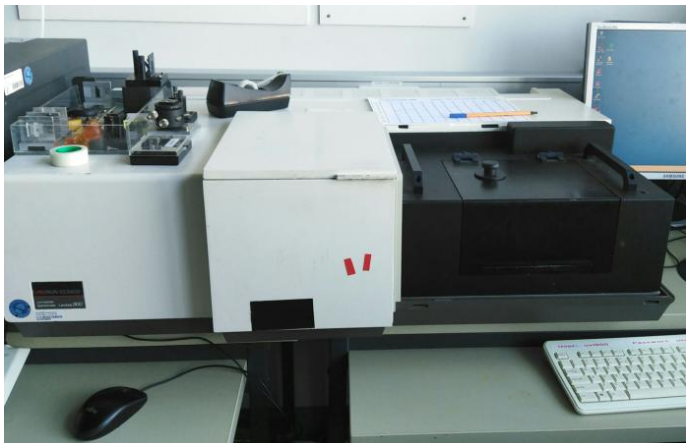

Figure 7.2. PerkinElmer Lambda 900 spectrometer.

Solution optical absorption measurements were performed using a PerkinElmer Lambda 900 spectrometer (Figure 7.2). Optical absorption spectra were calculated from the transmission spectra using the following equation

$$A = 2 - \log(T), \qquad \text{(Equation 7.2)}$$

wherein A is the absorbance at a certain wavelength (λ) and T is the transmitted radiation.

7.3.4 Film morphology

Figure 7.3. Leica polarized optical microscope.

The optical microscopy and polarized optical microscopy images were recorded using a Leica polarized optical microscope equipped with a digital CCD camera (Figure 7.3).

Atomic force microscope is a common scanning probe microscopy method widely used to get structural and morphological information if the surface. The atomic force microscope consists of a cantilever with a sharp probe tip. When the probe tip is brought close to the sample surface, forces between the tip and the sample lead to a deflection of the tip. The combining analysis of height and phase images gives surface information such as thickness, surface roughness, grain size and phase distribution, respectively. In this thesis, atomic force microscopy measurements for OSC films were performed by a Dimension Icon FS setup in tapping mode (Figure 7.4).

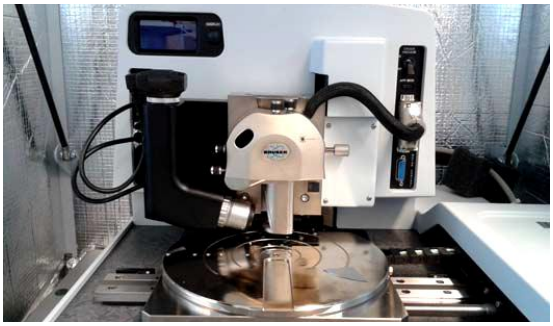

Figure 7.4. Dimension Icon FS atomic force microscope..

7.3.5 Film thickness

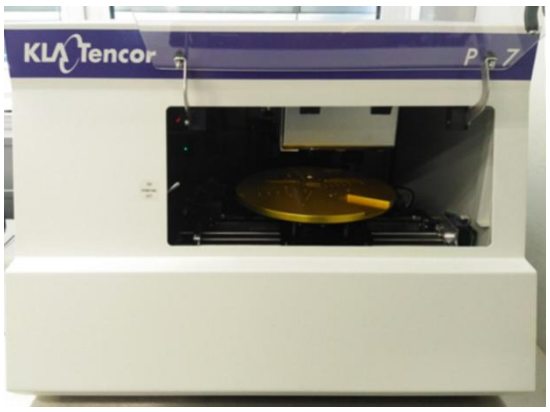

Figure 7.5. KLA Tencor Profiler.

The thickness of C8-BTBT and DPP(Th_2Bn)$_2$ crystalline films were measured by P-7 stylus profiler, KLA Tencor (Figure 7.5).

7.3.6 Molecule organization

GIWAXS is a röntgen based scattering technique for the investigation of molecular organization of OSC thin films.[5] The GIWAXS measurement geometry is schematically shown in Figure 7.6. A grazing incident angle, α, is applied and the diffuse scattering from the sample surface is collected with a 2D detector. In this thesis, GIWAXS was carried out by means of a solid anode X-ray tube (Siemens Kristalloflex X-ray source, copper anode X-ray tube operated at 35 kV and 40 mA), Osmic confocal MaxFlux optics, X-ray beam with pinhole collimation and a MAR345 image plate detector. The GIWAXS measurements were performed by Dr. Tomasz Marszalek and Michał Borkowski.

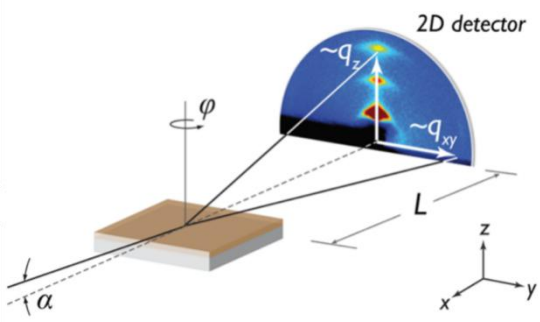

Figure 7.6. GIWAXS measurement geometry.[5]

Transmission electron microscopy (TEM) is a microscopy technique in which a beam of electrons is transmitted through a sample to form an image. The thickness for the TEM sample is ultrathin (less than 100 nm). During measurement, the sample is suspended on a grid and an image is formed from the interaction of the electrons with the sample as the beam is transmitted through the specimen.

In TEM measurement, the molecular organization can be obtained by selected area electron diffraction (SAED). The relation between wavelength and diffraction is governed by Bragg's Law. The TEM measurements presented in Chapter 3 were performed by a FEI Tecnai F20 TEM at 200 kV under liquid nitrogen cryoconditions, and SAED was recorded by using a Philips CM 12 electron microscope (Figure 7.7).

Figure 7.7. TEM of FEI Tecnai F20.

7.3.7 Charge carrier transport

Device fabrication

The heavily doped n-type silicon wafers were used as common gate electrode and the 300 nm thick SiO_2 layer (capacitance of 11 nF cm^{-2}) was adopted as the gate dielectric layer. Source and drain electrodes were deposited at a thickness of 50 nm by gold (Al) evaporation. The active OSC layer was fabrication by solution processing as discussed in Chapter 7.2.

OFETs characterization

A Keithley 4200-SCS was used for all standard electrical measurements in a glove-box under nitrogen atmosphere (Figure 7.8a). The source, drain and gate electrodes were

connected to three probes for all electrical measurements (Figure 7.8b). The mobility, on/off ratio and threshold voltage were obtained from the typical transfer and output curves as discussed in Chapter 1.1.3. In Chapter 3, the capacitance is influenced by the bottom PMMA layer, which is around 10–11 nF cm^{-2} owing to the thin thickness (less than 40 nm) of the bottom PMMA layer for dip-coated OSC:PMMA films. To simplify the comparison of the charge carrier transport, the mobilities of all devices were calculated based on the capacitance of 11 nF cm^{-2}. Though the simplification of mobility calculation leads to a slightly underestimation, there is no influence on the key conclusions.

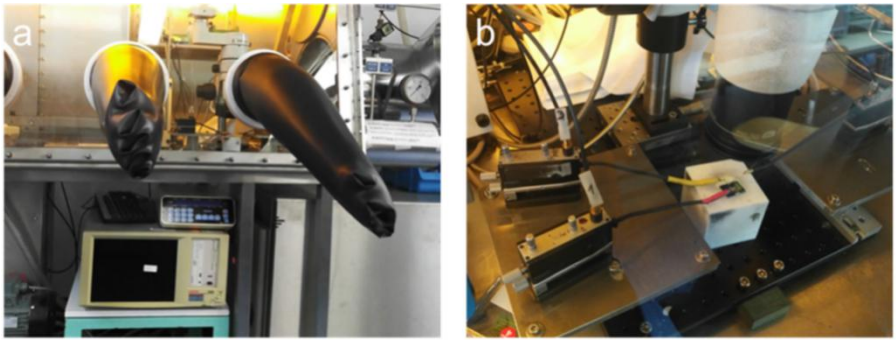

Figure 7.8. (a) Keithley 4200 system for OFETs measurement. (b) Probe station for contacting the devices inside the glove box.

7.4 Simulations

7.4.1 Fluid flow simulation of dip-coating of OSC:polymer blend

Steady-state simulations were conducted by using the COMSOL Multiphysics package. The flow and concentration distributions were captured by using the Creeping Flow and Transport of Dilute Species models. The model dimensions were determined based on the experimentally obtained shape of the meniscus during dip-coating (Figure 7.9).

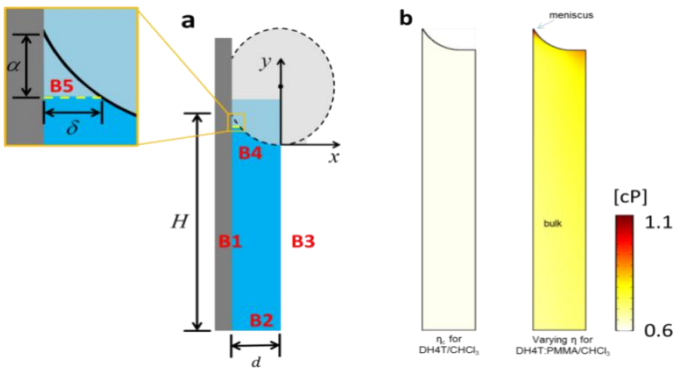

Figure 7.9. (a) Schematic of the simulation setup (note only the blue region is simulated), (b) viscosity simulation for defined DH4T/$CHCl_3$ and defined DH4T:$PMMA_{(2480\ kDa)}$/$CHCl_3$ solution.

The meniscus model was determined based on the experimentally obtained shape of the meniscus in dip-coating. The solvent evaporation rate was set as 1 μm/s. The dip-coating speed (i.e., the substrate moving speed) is 20 μm/s. The concentration of defined DH4T/$CHCl_3$ solution is c = 3 mg/mL, η_0=0.61 cP. The concentration of defined DH4T:$PMMA_{(2480\ kDa)}$/$CHCl_3$ solution is also 3 mg/mL, in which the concentration of $PMMA_{(2480\ kDa)}$ (c_{PMMA}) is 0.3 mg/mL that contributes to the viscosity, η_{bulk}=0.68 cP. The meniscus shape is fitting by an ellipse profile, $(\frac{x}{a})^2 + (\frac{y-r}{b})^2 = 1$, in which a=2.44 mm, b=2.75 mm, r=2.75 mm, d=2.15 mm, H = 20 mm, α = 50 μm.

The boundary conditions are as follows: B1 — moving wall, B2 — fully developed flow with constant solute concentration, B3 — symmetric boundary, B4 — evaporation boundary (ellipse gemeotry), and B5 — truncated boundary (to avoid the singularity problem in generating meshes). The concentration dependence of the solution's dynamic viscosity was explicitly accounted by using the experimentally measured and fitted viscosity data.[6]

The dynamic viscosity of a dilute PMMA/$CHCl_3$ solution was measured by an Ostwald capillary viscometer, fitted according to the Huggins equation, and estimated on the basis of COMSOL Multiphysics calculations.

7.4.2 Fluid flow simulation of angle dependent dip-coating

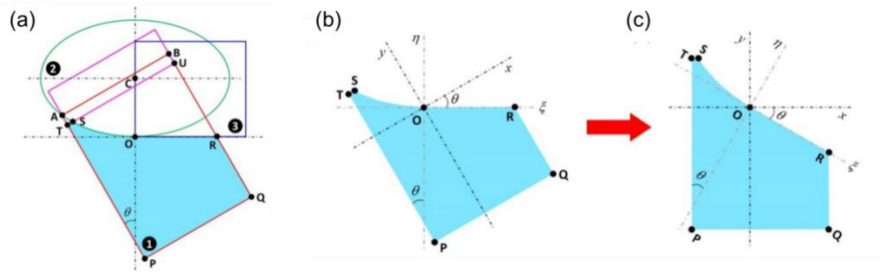

Figure 7.10. (a) Schematic illustration of a simulation domain. The domains are constructed as explained in the text. To simply the expressions of the boundary conditions, (b) the simulation domain was rotated clockwise by the tilt angle (α) to obtain (c) the simplified simulation domain. The rotation axis is normal to the page and passes through point O.

The governing equations are the steady state, two-dimensional continuity equation, momentum transport equation, and mass transport equation. Because of the small Reynolds numbers (Re < 1), the flow involved during dip-coating can be considered as Stokes flow (or creeping flow). For Stokes flow (or creeping flow), gravity has a negligible effect on the momentum and mass transport. As a result, the simulation domains can be rotated around point O clockwise by the tilt angle (α) so that the domain becomes vertically oriented (see Figure 7.10). This rotation significantly simplifies the expressions of the boundary conditions.

After determining the governing equations, we derived the boundary conditions that are appropriate for the dip-coating simulations. There are five boundaries: (1) B1: segment TP; (2) B2: segment PQ; (3) B3: segment QR; (4) B4: segment RO + elliptic arc OS; (5) B5: segment TS (truncated boundary to avoid the singularity problem in generating meshes). The corresponding physics models in COMSOL are the transport of dilute species model and the creeping flow model. For all the six simulations (i.e., α = 0°, 15°, 30°, 45°, 60°, 75°), we adopt the following parameters: dip-coating speed at 20 μm/s, solute concentration of bulk solution, c_{bulk} = 0.003 g/mL. The calculated concentration distribution and streamline are shown in Figures 7.11 and 7.12.

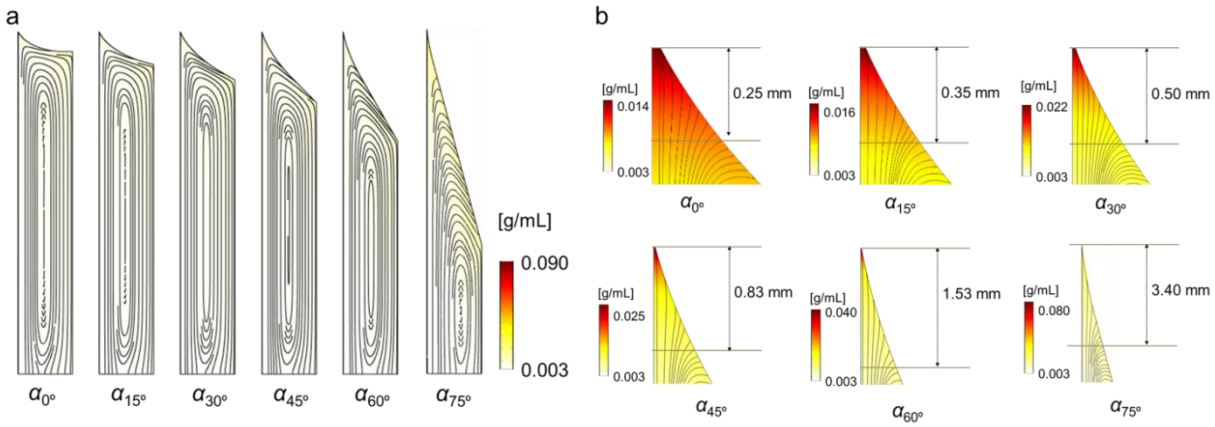

Figure 7.11. Concentration distributions and calculated streamline based on constant E_{bulk} for different α in (a) the entire simulated regime and (b) meniscus regime. The positions of stagnation point (x_{sp}) for different α are shown in the meniscus regime.

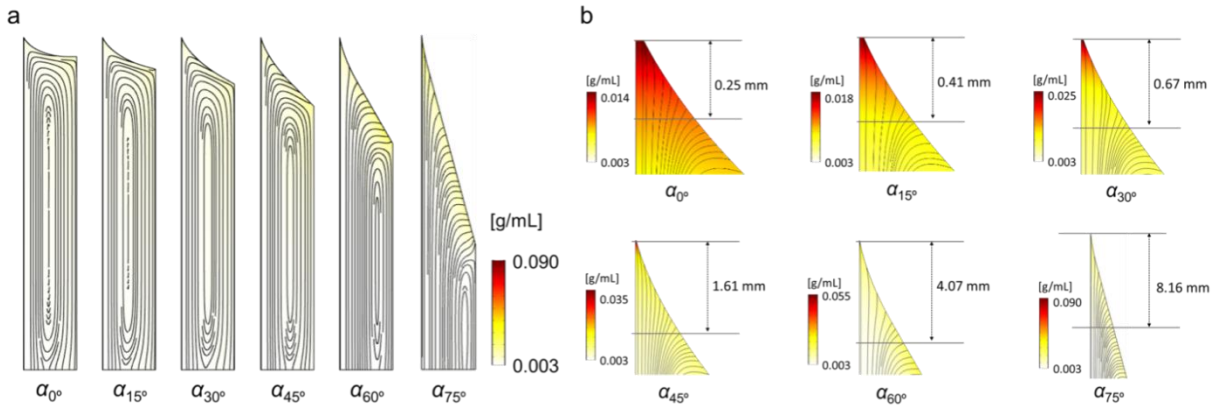

Figure 7.12. Concentration distribution and calculated streamline based on varied E_{bulk} for different α in (a) the entire simulated regime and (b) meniscus regime. The positions of stagnation point (x_{sp}) for different α are shown in the meniscus regime.

7.4.3 Numerical model of crystal growth

A phase field method in combination with a description for spatially anisotropic solvent evaporation was employed to numerically model the spherulitic crystal growth. The numerical model is an extension of models that used to describe liquid-liquid de-mixing in evaporating thin films in previous work of Dr. J. J. Michels[7-9].

7.5 Materials

In Chapter 2, pyrene-DPP analogues (**SM1-3**) are provided by Prof. Pierre M. Beaujuge and his group at the Physical Sciences and Engineering Division of King Abdullah University of Science and Technology in Saudi Arabia.

In Chapter 3, DH4T was purchased from Syncom and used without further purification. PMMA (2 kDa, 100 kDa and 2480 kDa) was purchased from Sigma-Aldrich.

In Chapter 4, C8-BTBT were purchased from Sigma-Aldrich and used without further purification.

In Chapter 5, DPP(Th_2Bn)$_2$ is provided by Prof. Pierre M. Beaujuge and his group at the Physical Sciences and Engineering Division of King Abdullah University of Science and Technology in Saudi Arabia.

Reference

1. S. Wang, P. Gao, I. Liebewirth, K. Kirchhoff, S. Pang, X. Feng, W. Pisula and K. Müllen, *Chem. Mater.*, 2011, **23**(22): 4960-4964.
2. D. Grosso, *J. Mater. Chem.*, 2011, **21**(43): 17033-17038.
3. W. Pisula, A. Menon, M. Stepputat, I. Lieberwirth, U. Kolb, A. Tracz, H. Sirringhaus, T. Pakula and K. Müllen, *Adv. Mater.*, 2005, **17**(6): 684-689.
4. F. Zhang, E. Mohammadi, X. Luo, J. Strzalka, J. Mei and Y. Diao, *Langmuir*, 2018, **34**(3): 1109-1122.
5. J. Rivnay, S.C. Mannsfeld, C.E. Miller, A. Salleo and M.F. Toney, *Chem. Rev.*, 2012, **112**(10): 5488-5519.
6. C. Hsueh, F. Doumenc and B. Guerrier, *Europ. Phys. J. Special Topics*, 2013, **219**(1): 51-57.
7. J. J. Michels and E. Moons, *Macromolecules*, 2013, **46**(21): 8693-8701.
8. C. Schaefer, P. van der Schoot and J. J. Michels, *Phys. Rev. E,* 2015, **91**(2): 022602.
9. C. Schaefer, J. J. Michels and P. van der Schoot, *Macromolecules* 2016, **49**(18): 6858-6870.

List of publications

1. Junzhi Liu, Ji Ma, **Ke Zhang**, Prince Ravat, Peter Machata, Stanislav Avdoshenko, Felix Hennersdorf, Hartmut Komber, Wojciech Pisula, Jan J Weigand, Alexey A Popov, Reinhard Berger, Klaus Müllen, Xinliang Feng, *π-Extended and Curved Antiaromatic Polycyclic Hydrocarbons*, *J. Am. Chem. Soc.*, **2017**, *139* (22): 7513-7521.

2. Ben-Lin Hu, **Ke Zhang**, Cunbin An, Wojciech Pisula, Martin Baumgarten, *Thiadiazoloquinoxaline-Fused Naphthalenediimides for n-Type Organic Field-Effect Transistors (OFETs)*, Org. Lett., 2017, 19 (23): 6300-6303.

3. Sheng Yang, **Ke Zhang**, Antonio Gaetano Ricciardulli, Panpan Zhang, Zhongquan Liao, Martin R Lohe, Ehrenfried Zschech, Paul WM Blom, Wojciech Pisula, Klaus Müllen, Xinliang Feng, *A Delamination Strategy for Thinly Layered Defect-Free High-Mobility Black Phosphorus Flakes*, Angewandte Chemie, 2018, 130(17): 4767-4771.

4. **Ke Zhang**, Philipp Wucher, Tomasz Marszalek, Maxime Babics, Andreas Ringk, Paul WM Blom, Pierre M Beaujuge, Wojciech Pisula, *Long-Range Molecular Self-Assembly from π-Extended Pyrene-Functionalized Diketopyrrolopyrroles*, Chem. Mater., 2018, 30 (15): 5032-5040.

5. **Ke Zhang**, Tomasz Marszalek, Philipp Wucher, Zuyuan Wang, Lothar Veith, Hao Lu, Hans-Joachim Räder, Pierre M Beaujuge, Paul WM Blom, Wojciech Pisula, *Crystallization Control of Organic Semiconductors during Meniscus-Guided Coating by Blending with Polymer Binder*, Adv. Funct. Mater. , 2018, 28(50): 1805594.

6. Ben-Lin Hu, **Ke Zhang**, Cunbin An, Dieter Schollmeyer, Wojciech Pisula, Martin Baumgarten, *Layered Thiadiazoloquinoxaline-Containing Long Pyrene-Fused*

N-Heteroacenes, Angewandte Chemie International Edition, 2018, 57(38): 12375-12379.

7. Xuelin Yao, **Ke Zhang**, Klaus Müllen, Xiao-Ye Wang, *Direct C− H Borylation at the 2-and 2, 7-Positions of Pyrene Leading to Brightly Blue-and Green-Emitting Chromophores*, Asian Journal of Organic Chemistry, 2018, 7(11): 2233-2238.

8. Keitaro Yamamoto, Yutaka Ie, Masashi Nitani, Norimitsu Tohnai, Fumitoshi Kakiuchi, **Ke Zhang**, Wojciech Pisula, Kamal Asadi, Paul WM Blom, Yoshio Aso, *Oligothiophene quinoids containing a benzo[c]thiophene unit for the stabilization of the quinoidal electronic structure*, J. Mater. Chem. C, 2018, 6, 7493-7500.

9. Yubin Fu, **Ke Zhang**, Evgenia Dmitrieva, Fupin Liu, Ji Ma, Jan Weigand, Alexey A. Popov, Reinhard Berger, Wojciech Pisula, Junzhi Liu, Xinliang Feng, *NBN-embedded polycyclic aromatic hydrocarbons containing pentagonal and heptagonal rings*, Org. Lett., 2019, 21(5): 1354-1358.

10. Ji Ma, **Ke Zhang**, Karl Sebastian Schellhammer, Yubin Fu, Hartmut Komber, Chi Xu, Alexey A. Popov, Felix Hennersdorf, Jan J. Weigand, Shengqiang Zhou, Wojciech Pisula, Frank Ortmann, Reinhard Berger, Junzhi Liu, and Xinliang Feng, *Wavy-shaped Polycyclic Hydrocarbons with Controlled Aromaticity*, Chem. Sci., 2019,10: 4025-4031.

11. **Ke Zhang**, Zuyuan Wang, Tomasz Marszalek, Michał Borkowski, Georg Fytas, Paul W. M. Blom, Wojciech Pisula, *Role of Meniscus Shape on Crystallization of Organic Semiconductors during Meniscus-Guided Coating*. (*submitted*)

12. **Ke Zhang**, Michał Borkowski, Philipp Wucher, Pierre M. Beaujuge, Paul W. M. Blom, Tomasz Marszalek, Wojciech Pisula, Jasper J. Michels, *Crystallization Paradigm for Meniscus-Guided Coating of Organic Semiconductors*.(*prepared*)

Poster conference contribution

1. **Ke Zhang**, Philipp Wucher, Tomasz Marszalek, Maxime Babics, Andreas Ringk, Paul WM Blom, Pierre M Beaujuge, Wojciech Pisula, *Long-Range Molecular Self-Assembly from π-Extended Pyrene-Functionalized Diketopyrrolopyrroles*, 14th European Conference on Molecular Electronics (ECME 14), 29.Aug.2017-02.Sep.2017, Dresden, Germany.

2. **Ke Zhang**, Tomasz Marszalek, Philipp Wucher, Zuyuan Wang, Lothar Veith, Hao Lu, Hans-Joachim Räder, Pierre M Beaujuge, Paul WM Blom, Wojciech Pisula, *Crystallization Control of Large Area Organic Semiconductors during Meniscus-Guided Coating by Blending with Polymer Binder*, Innovations in Large Area Electronics Conference (InnoLAE 2019), 21-23. Jan, 2 b019, Cambridge, England.